MISSOURI S&T

CENTER FOR TRANSPORTATION INFRASTRUCTURE AND SAFETY

Unbonded Portland Cement Concrete Overlay/ Pavement Monitoring with Integrated Grating and Scattering Optical Fiber Sensors

by

Genda Chen, Ph.D., P.E., F.ASCE, F.SEI
Professor and Robert W. Abbett Chair in Civil Engineering
Department of Civil, Architectural, and Environmental Engineering
Missouri University of Science and Technology Rolla, MO 65409-0030

Ying Huang, Ph.D.
Assistant Professor
Department of Civil Engineering
North Dakota State University
Fargo, ND 58108-6050

Yi Bao, Ph.D. Candidate Graduate Research Assistant Department of Civil, Architectural, and Environmental Engineering Missouri University of Science and Technology
Rolla, MO 65409-0030

NUTC
R330

**A National University Transportation Center
at Missouri University of Science and Technology**

Disclaimer

The contents of this report reflect the views of the author(s), who are responsible for the facts and the accuracy of information presented herein. This document is disseminated under the sponsorship of the Department of Transportation, University Transportation Centers Program and the Center for Transportation Infrastructure and Safety NUTC program at the Missouri University of Science and Technology, in the interest of information exchange. The U.S. Government and Center for Transportation Infrastructure and Safety assumes no liability for the contents or use thereof.

Technical Report Documentation Page

1. Report No. NUTC R330	2. Government Accession No.	3. Recipient's Catalog No.
4. Title and Subtitle Unbonded Portland Cement Concrete Overlay/Pavement Monitoring with Integrated Grating and Scattering Optical Fiber Sensors		5. Report Date June 30, 2014
		6. Performing Organization Code
7. Author/s Genda Chen, Ying Huang, and Yi Bao		8. Performing Organization Report No. Project #: NUTC 00041896
9. Performing Organization Name and Address Center for Transportation Infrastructure and Safety/NUTC Program Missouri University of Science and Technology 220 Engineering Research Lab Rolla, MO 65409		10. Work Unit No. (TRAIS)
		11. Contract or Grant No. DTRT06-G-0014
12. Sponsoring Organization Name and Address U.S. Department of Transportation Research and Innovative Technology Administration 1200 New Jersey Avenue, SE Washington, DC 20590		13. Type of Report and Period Covered Final
		14. Sponsoring Agency Code
15. Supplementary Notes This study was completed in collaboration with the Minnesota Department of Transportation.		

16. Abstract

This report summarizes the findings and results from a laboratory and field study on the strain distribution and crack development in 3" thick concrete panels cast on top of existing concrete pavements as a rapid rehabilitation strategy for roadways. Both fiber Bragg gratings (FBG) and Brillouin Optical Time Domain Reflectometry/Analysis (BOTDR/A) were applied and tested for their feasibility and effectiveness in distributed strain measurement and crack detection. For laboratory tests, six 6'×6" panels were cast similar to their corresponding field construction. Each was tested under both truck loads and under three-point loads. The performance of distributed BOTDR/A strain measurements was compared with that of FBG sensors. In field study, the performance of FBG sensors was compared with that from strain gauges when the ambient temperature was measured with thermocouples. Overall, hairline to major cracks can be successfully detected with the distributed BOTDA measurements. The strain distributions measured from the FBG and BOTDR/A sensors are consistent. The FBG readings are in good agreement with those of strain gauges. Both FBG and BOTDR/A technologies are promising for pavement monitoring.

17. Key Words Unbonded concrete panel, optical fiber sensors, crack detection, strain distribution	18. Distribution Statement No restrictions. This document is available to the public through the National Technical Information Service, Springfield, Virginia 22161.		
19. Security Classification (of this report) Unclassified	20. Security Classification (of this page) Unclassified	21. No. Of Pages 96	22. Price

Form DOT F 1700.7 (8-72)

Executive Summary

This report summarizes the findings and results of Project No. NUTC41896 under the USDOT Contract No. DTRT06-G-0014 in collaboration with the Minnesota Department of Transportation (MnDOT). This study was focused on the applications of distributed and point optical fiber sensors for strain measurement and crack detection in unbonded concrete panels/overlays that were directly cast on top of existing concrete pavement. The main objectives of this study were: a) to characterize the strain sensing properties of three types of distributed optical fibers with the recently-developed pulse pre-pump Brillouin optical time domain analysis (PPP-BOTDA), b) to develop an installation method applicable for real world applications, (c) to apply the PPP-BOTDA and Fiber Bragg grating (FBG) sensing technologies into pavement monitoring and document their performances with laboratory and field tests, and (d) to develop a database of concrete pavement performance with a benchmark roadway at the MnDOT roadway test facility.

Unbonded Portland cement concrete (PCC) overlays have received increasing attention in new highway constructions and existing pavement rehabilitations. Thin concrete panels have been cast on top of an existing pavement layer with a fabric sheet in the middle to rapidly and cost-effectively improve the driving condition of existing roadways. The service life of PCC overlays can be appreciably extended by appropriate monitoring strategies at an early stage of deterioration based on the information provided by a sensing system.

Three types of single mode optical fibers (bare SMF-28e$^+$ fiber, SMF-28e$^+$ fiber with tight buffer, and FN-SIL-1 concrete cack cable) were considered as distributed optical fiber sensors. They were tested and characterized on a low capacity load frame by measuring their tensile strains at room temperature under axial loads. A Neubrescope Model 7020 was used to measure strains based on the PPP-BOTDA technology with 2 cm in spatial resolution. An installation method applicable for both laboratory and field conditions was proposed to address the logistics of handling delicate optical fibers in concrete construction environment. With the proposed installation method, optical fibers were installed into six full-scale, micro-fiber reinforced concrete panels in the laboratory and three panels in the field test site at MnDOT. The laboratory concrete panels were comparable with the field benchmark pavement overlays at the MnDOT test site. The specimens were first loaded with a dump truck to simulate real world applications, considering two cases of empty and fully-loaded trucks. Each panel was then tested to failure in flexure under a three-point loading setup. Strain distributions were obtained from the single mode optical fiber and validated by commercial FBG sensors. Cracks were identified and localized at significant peaks of the strain distributions. The onset and propagation of concrete cracks were successfully detected with high resolution.

Among the three types of distributed optical fiber sensors, the bare fiber was most fragile during construction and operation, but most sensitive to any strain change or micro-crack. The concrete crack cable was most rugged, but least sensitive to micro-cracks and robust in micro-crack detection. The ruggedness and sensitivity of the fiber with a tight buffer were in between the bare fiber and the concrete crack cable. The strain distribution resulted from the three optical fiber sensors are in good agreement. They can be applied to successfully locate cracks in the concrete panels. It was observed that the three types of fibers were functional until the concrete panels have experienced inelastic deformation, making the distributed strain sensing a promising technology for pavement monitoring in field applications.

Table of Contents

Table of Figures

Table of Tables

Acknowledgements

Chapter 1 Introduction

Unbonded Portland cement concrete (PCC) overlays have received increasing attention in new highway constructions and existing pavement rehabilitations [1, 2]. Thin concrete panels have been cast on top of an existing pavement with a fabric sheet in between to rapidly and cost-effectively improve the driving condition of existing roadways. The service life of PCC overlays can be appreciably extended by appropriate rehabilitation strategies at an early stage of deterioration, based on the information provided by a pavement condition monitoring system. However, the cost-effective monitoring technologies are currently under development. Fiber Bragg grating (FBG) sensors have been proposed and successfully used in various applications [3, 4]. However, FBG sensors are limited in that they are only point sensitive and their measurement represents an average effect over a given length, greatly reducing the measurement accuracy. Due to the unpredictable development of cracks within concrete structures, major challenges arise in using point sensors to accurately measure the condition of large volumes such as existing structures or roads. A quasi-distributed optical fiber sensor system was proposed by multiplexing multiple FBG sensors in series [5]. The strain distribution was mapped by combining the measurements from all FBG sensors. In this case, only the FBG locations were actually monitored and the measurement accuracy elsewhere changes depending on the density of FBG sensors. A novel coaxial cable was invented and used to measure strain and detect cracks in a full-scale reinforced concrete girder with distributed sensing ability [6]. However, the electromagnetic signals travelling in the cable were not immune to electromagnetic interference (EMI), and thus the measurements obtained from a coaxial cable were affected by external conditions. Fully distributed optical fiber sensor technologies have attracted intensive research interests worldwide and are being studied and successfully applied in various structures. They have many advantages such as large coverage area of continuous measurements, cost saving, immunity to EMI, and ruggedness in harsh environments [7].

Light scattering based sensing technologies provide excellent opportunities for distributed sensing of strain and temperature along the length of an optical fiber [7]. The technologies can be implemented in various applications such as strain distribution or crack detection in civil engineering structures, ground settlement or sliding damage monitoring, and detection of pipeline leaking or buckling [8-14]. They are further introduced and discussed below.

1.1 Light scatterings in an optical fiber

When it propagates in an optical fiber, a light wave interacts with the constituent atoms and molecules. If the light wavelength does not resonate with the oscillatory motion of the atoms and molecules, the electric field of the light induces a time dependent polarization dipole. The induced dipole generates a secondary electromagnetic (EM) wave, which is referred to as light scattering [7]. As illustrated in Fig. 1.1, the EM wave in optical fibers is typically present in the form of Rayleigh scattering, Brillouin scattering, and Raman scattering. Rayleigh scattering is a linear scattering process in which the scattered power is simply proportional to the incident power due to non-propagating density fluctuations. Since no energy is transferred to the optical fiber in Rayleigh scattering, there is no change in frequency of the scattered light compared with that of the incident light, thus named as elastic scattering. Located at both sides of the Rayleigh peak in Fig. 1.1 are two Brillouin peaks. They are contributed by the Brillouin scattering of sound waves moving in opposite directions. The left peak with a down-shifted frequency is called the Stokes peak while the right one with an up-shifted frequency is called the anti-Stokes peak. Raman peaks in Fig. 1.1 are contributed by the interaction of the light wave with molecular vibration in the optical fiber medium. Raman spectra usually contain many separated sharp bands corresponding to electronic vibration, each band resulting from molecular rotation or reorientation excitations [2]. Both Brillouin and Raman scattering are inelastic scattering because they are associated with frequency shifts.

Fig. 1.1 shows a representative spontaneous scattering spectrum from a typical solid state matter. Spontaneous scattering occurs when an incident light is scattered without significantly changing the

optical properties of a propagating medium. It includes Rayleigh, Brillouin, and Raman scattering. As the input light intensity increases to certain level, stimulated scattering occurs when the properties of the medium are modified significantly and the scattered light is proportional to the power of the input light. The evolution from spontaneous to stimulated scattering corresponds to a transition of the medium behavior from a linear to a non-linear regime.
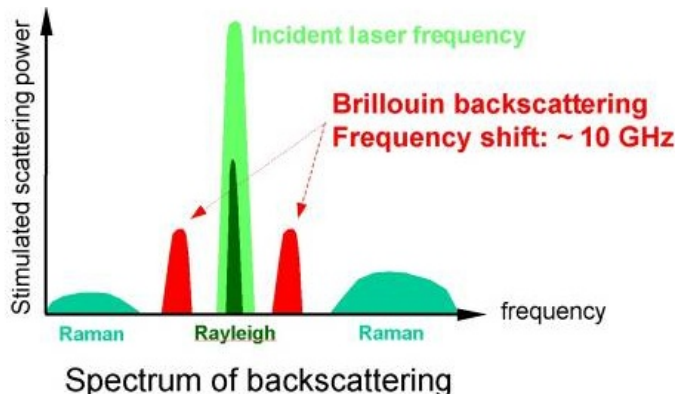
Fig. 1.1. Representative spontaneous scattering spectrum from a typical solid state matter.

1.1.1 Rayleigh scattering

At microscopic level, the molecules making up any ordinary matter are immersed in a violent internal EM environment in spite of the macroscopic charge neutrality for most macroscopic materials [7]. The violent EM environment constantly causes the molecules to readjust their electron clouds. By changing its own electron cloud configuration, each molecule contributes to the changing environment for other neighboring molecules in a perpetual cycle. Therefore, on a relatively small spatial scale (order of tens of molecular sizes), one would observe fluctuations in terms of local charge density, local temperature, or even strain values. Without incident light, however, such short range fluctuations would not produce measurable macroscopic effects at a far distance as they are mutually incoherent and thus cancelled out statistically. In this case, the macroscopic EM field inside any material is zero. However, under the excitation of external light, the EM field forces the originally incoherent, randomly fluctuating molecular clouds reoriented and responded collectively the same way on a small spatial scale. Such a collective tendency to respond to an EM field would result in macroscopic polarization that is proportional to the external electric field. The collective response is characterized by a material-dependent parameter associated with the randomly fluctuating portion. The fluctuating dielectric parameter gives a fluctuating polarization-induced light emission in all directions as illustrated in Fig. 1.2. Some of the scattered Rayleigh light is re-captured by the waveguide and sent in the backward direction. This backward propagating Rayleigh scattered light has a time delay that can be used for distributed sensing. The Rayleigh scattering can be treated as a single scattering process.

Similar to elastic Rayleigh scattering, Mie scattering arising from large scattering centers such as dust particles results in no frequency change. The strength of Mie scattering is related to the size of scattering particles and their refractive index with respect to the scattering medium. Mie scattering can be applied to detect dust particle size as widely used in biomedical sensing.
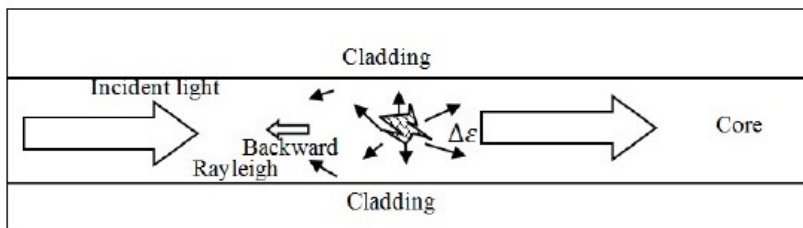
Fig. 1.2. Schematic diagram for the spontaneous Rayleigh scattering process.

1.1.2 Brillouin scattering

The Brillouin scattering in optical fiber represents light scattering from collective acoustic oscillations of the glass [8]. From the microscopic point of view, the intermolecular interaction in glass makes it favorable for molecules to stay at some stable distance, corresponding to equilibrium positions of the molecules. When spaced closer than the stable distance, two molecules will be pushed away from each other. Due to inertia, they will not stop at their equilibrium positions. When further separated apart, the two molecules will be pulled back in the opposite position but pass their equilibrium positions again. Such a repeating cycle forms a collective motion called acoustic phonons. When an optical beam (so-called pump wave) and another wave named Stokes wave are introduced around the down-shifted Brillouin frequency, their beating creates a modified density change due to electrostriction effect, resulting in the so-called stimulated Brillouin scattering (SBS). The density variation is associated with a mechanical acoustic wave and can be affected by local temperature, strain, and vibration through the changed effective refractive index of optical fiber and the changed sound velocity. Through the measurement of static or dynamic changes in Brillouin frequency along the length of an optical fiber, one can realize a distributed optical fiber sensor for temperature, strain and vibration over tens of kilometers.

For an intense light beam that travels in an optical fiber, acoustic vibration in the medium may be produced by the variation in electric field of the beam itself via electrostriction effect. The beam may undergo SBS from the acoustic vibration, usually in opposite direction to the incoming beam. Brillouin scattering can be optically stimulated to strengthen the scattering mechanism to its greatest potential, leading to an improved signal-to-noise ratio. The Brillouin frequency based technique is opposed to the intensity based techniques such as Raman and is inherently more accurate and more stable in long term since the intensity based techniques are sensitive to potential drifting. For liquids and gases, typical frequency shifts are of the order of 1~10 GHz (wavelength shifts of 1~10 pm for visible light).

1.2.3 Raman scattering

When light is scattered from an atom or molecule, most photons are elastically scattered. That is, the scattered photons have the same frequency with the incident photons. Only a small fraction of the scattered light, approximately 1 out of 10 million photons, is excited with photons' frequency different from that of the incident photons. The interaction of the small portion of light with matter in a linear regime, named as Raman scattering, allows a precise match between the absorption and emission of a photon and the difference in energy levels of the interacting electron or electrons. Since only a small portion of light is scattered by Raman scattering, the intensity is usually weak unless stimulated. Raman scattering technology has been widely used for temperature monitoring in oil wells and transport pipelines. The highest spatial resolution for Raman optical time domain reflectometry (OTDR) is 0.24 m over a sensing distance of 135 m and the temperature resolution is 2.5°C. The limited sensing distance is due to the weak anti-Stokes Raman signal, which is 20-30 dB weaker than that of the Rayleigh scattering light.

Raman optical frequency domain reflectometry (OFDR) was developed in 1998, including Stoke scattering and anti-Stokes scattering. During the Raman scattering, the photon jumps from the beginning steady-state to another steady-state. According to the Bose-Einstein probability distribution of photons, Stokes Raman scattering power is related to the distribution of temperature. Raman OTDR is one-dimensional optical radar that provides an echo scan of the entire length of an optical fiber at Raman stokes and anti-stokes frequencies. It is capable of simultaneously measuring temperature at many points along an optical fiber. In this technique, a short laser pulse is beamed along the fiber and the backscattered Raman light is detected with high resolution.

1.2 Rayleigh scattering based optical sensing technologies

1.2.1 Conventional optical time domain reflectometry

OTDR was first introduced to monitor signal attenuation along an optical fiber and thus detect fault in telecommunication cables [13]. It was then applied in various novel optical fiber sensors to monitor strain,

temperature, and displacement with the spatial resolution up to 0.5 m [9, 10, 15-18]. OTDR profiles the intensity of Rayleigh backscattering that varies over an optical fiber.

1.2.2 Polarization optical time domain reflectometry

Polarization OTDR uses a broadband frequency laser of ~0.1 nm to create a polarized pulse of light. The signal attenuation modulated with the local polarization state change is detected by Rayleigh backscattering. Polarization properties of an optical fiber can be modulated with various parameters such as pressure, strain, temperature, and electrical and magnetic fields. However, the contributions of various parameters are hard to distinguish [19, 20].

1.2.3 Coherent and phase OTDRs

Coherent OTDR (COTDR) measures the low coherence between a scattered light and a reference light over the length of an optical fiber with coherent detection [21]. Since the distances among adjacent scattering centers (particles) are significantly smaller than the wavelength of light travelled in an optical fiber, the secondary light waves due to Rayleigh scattering are coherent. In this case, the resulting intensity is a summation of the scattered fields. Coherent detection is realized by optical mixing of the backscattered light and a reference light. With the balanced detection technique such as photon counting [22, 23], the DC noise is reduced significantly. In this case, the coherent detection gives a shot noise limited sensitivity of -140 dB at a 3 Hz bandwidth for millimeter spatial resolution when the sensing distance is in the order of meters.

Phase OTDR utilizes a laser source with narrow spectral line width and low frequency shift to form the interference of the Rayleigh backscattered signals whose amplitude changes with vibration [24-26]. Phase OTDR measures the coherent light source with direct detection. In this case, a kHz line width laser is used with short pulses for coherent detection or with large pulses for direct detection; the spatial resolution of a few hundred meters can be achieved with 12 km of fiber for intrusion sensing. Because of coherent Rayleigh scattering, exact locations of intrusion can be identified unlike the polarization OTDR where only a starting point of the location can be used in an alarm system due to continuous state of polarization (SOP) change in the optical fiber by the disturbance.

1.2.4 Optical frequency domain reflectometry

The spatial resolution of OTDR technologies is generally related to the pulse width in optical domain and the bandwidth of detector, electrical amplifier and digitizer in electronic and digital domains. Millimeter spatial resolution measurement will require a bandwidth of tens of GHz and thus the use of a very expensive and complicated system [2]. OFDR is an alternative technique. It converts the frequency response into time domain by Fourier transformation so that the spatial resolution with OFDR does not depend on the bandwidths of detector and digitizer. Therefore, OFDR is a cost-effective distributed sensing technique with high resolution [27, 28].

1.3 Brillouin scattering based distributed sensing technologies

Brillouin scattering in an optical fiber describes the interaction of a light wave (photon) with an acoustic wave (phonon) that is equivalent to a characteristic density variation along the fiber. It can be spontaneous or stimulated, depending upon whether scattering strongly changes the property of the optical fiber medium [7, 8]. The spontaneous Brillouin scattering preserves the medium property while the stimulated Brillouin scattering affects the light propagating medium.

The first demonstration of Brillouin scattering spectrum in a distributed fashion was based on the stimulated Brillouin scattering [29], referred to as Brillouin optical time domain analysis (BOTDA). It used pump and probe waves counter-propagating from the two ends of an optical fiber. When the frequency difference between a pump pulse and probe continuous wave (CW) matches with the local Brillouin frequency, Brillouin gain or Brillouin loss will be observed at this location. The Brillouin frequency shift can be modulated with strain and temperature changes [30, 31]. A 3°C temperature

accuracy and 100 m spatial resolution over a sensing distance of 1.2 km was demonstrated [32, 33]. Later, a Brillouin optical time domain reflectometry (BOTDR) was proposed with the advantage of monitoring a system from one end of the sensing fiber [34]. The BOTDR performance was improved by coherent detection with a sensing distance up to 11 km at similar spatial resolution and temperature accuracy. However, the spatial resolution is still in the order of meter, which is mainly limited by the pulse width. The key to achieving long distance sensing is to limit the pump power so that low gain can be maintained over the entire sensing length, preventing gain saturation of the Stokes wave and reducing pump wave depletion. In addition to the power requirement, SOP matching is critical as the choice of SOP for pump and probe waves should maintain a modest gain over the entire sensing length, rather than high gain at the front of the fiber section. This is very different from the condition of short sensing length, in which SOP matching is required to have as much gain as possible. For long sensing distances, high stimulated Brillouin threshold fiber is preferred to ensure low Brillouin gain over the entire fiber [35, 36].

A pulse with narrow bandwidth can lead to high resolution but may not stimulate sufficient acoustic waves. To utilize the stimulated Brillouin scattering, the pulse bandwidth must be longer than the phonon relaxation time. It has been demonstrated that 28 ns is required to get the phonon fully stimulated, which corresponds to 3 m spatial resolution [29-31]. To solve this problem, pulse pre-pump BOTDA or PPP-BOTDA has been proposed to take advantage of a pre-pump pulse that stimulates the phonon before a narrow bandwidth pulse arrives and thus a centimeter spatial resolution has been achieved [47]. At the same time, frequency domain distributed sensing technologies have been developed, such as Brillouin optical frequency domain analysis (BOFDA) [38, 39] and Brillouin optical correlation domain analysis (BOCDA) [40]. With BOFDA, 3 cm spatial resolution has been realized with 9 m measurement distance [41]. With BOCDA, 1cm spatial resolution has been reported for short measurement distance [42] and 7 cm spatial resolution has been realized with 1 km measurement distance [43]. With differential Brillouin gains based on the differential pulse-width pair (DPP-BOTDA) technology, the time-domain waveform is subtracted at the same scanned Brillouin frequency obtained from light pulses with different pulse widths, and the spatial resolution is appreciably improved to 2 cm with 2 km sensing length [44-46].

1.3.2 BOTDA

BOTDA measures strain and temperature distributions by using pump and probe waves counter-propagating in a fiber. The pumping pulse light is launched at one end of the fiber and propagates in the fiber, while the CW light is launched at the opposite end of the fiber and propagates in the opposite direction. When the frequency difference between the pump pulse and the probe continuous wave (CW) matches with the Brillouin frequency of the optical fiber, Brillouin gain or Brillouin loss will happen and the density of the medium will be altered. A typical BOTDA system is schematically shown in Fig. 1.3 with its sensing principle as illustrated in Fig. 1.4. The Brillouin frequency shift Δv_b is on the order of 9-13 GHz for light waves of 1.3-1.6 μm wavelengths in a standard SMF. It can be determined by [16].

$$\Delta v_b = \frac{2nV_a}{\lambda} \tag{1.1}$$

where n is the effective refractive index, V_a is the acoustic velocity, and λ is the wavelength of the laser source.
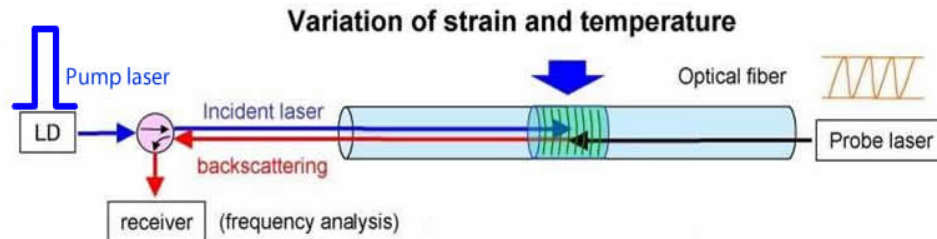
Fig. 1.3. Schematic diagram of a BOTDA system.

5
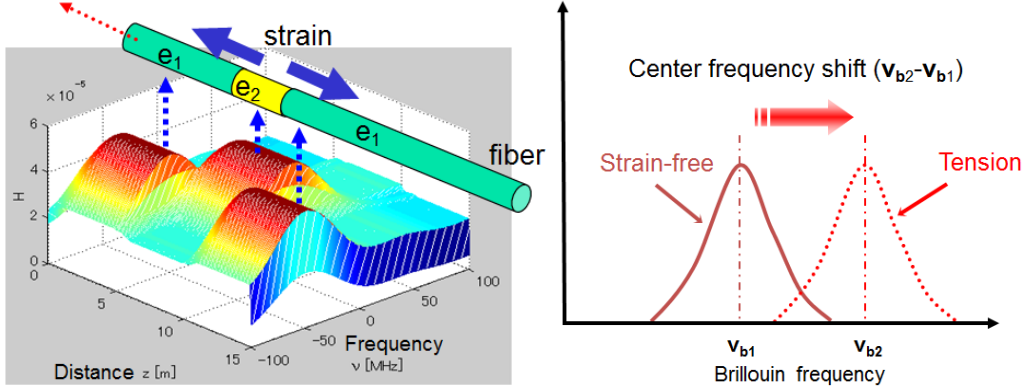
(a) Stimulated Brillouin scattering   (b) Brillouin frequency shift under tension

Fig. 1.4. BOTDA sensing principle.

The Brillouin frequency shift $\varDelta v_b$ in an optical fiber is linearly modulated with the strain and temperature change applied on the fiber. It can be expressed into:

$$\varDelta v_b = C_\varepsilon \varDelta\varepsilon + C_T \varDelta T \tag{1.2}$$

where C_ε and C_T denote the strain and the temperature coefficients, respectively; and $\varDelta\varepsilon$ and $\varDelta T$ denote the strain and the temperature changes, respectively. The location of Brillouin backscattering along the optical fiber can be measured by the time delay of the backscattering wave at the speed of light c. With a pulse width τ, the spatial resolution can be defined as the location accuracy that can be determined by:

$$\Delta z = \frac{\tau c}{2n} \tag{1.3}$$

According to Eq. (1.3), the spatial resolution can be improved by using a short pulse. However, a short pulse provides a broadened Brillouin gain spectrum (BGS) by which the signal-to-noise ratio (SNR) will be significantly reduced. Even though high pump power is used to compensate for the power loss and thus enhance spatial resolution, the measurement accuracy of the Brillouin frequency shift remains low [7]. These limitations indicate that high precision distributed sensing cannot be achieved by simply shortening the pulse-width [17]. Generally, the spatial resolution of conventional BOTDA is limited to 1 m.

1.3.2 BOTDR

Unlike BOTDA, BOTDR measures strain and temperature distributions along an optical fiber from one end of the fiber as shown in Fig. 1.5. The Brillouin frequency shift can also be related to the applied strain and temperature in a certain part of the fiber by Eq. (1.2). Given the change in one parameter (strain or temperature), the other parameter can be determined along the length of the optical fiber. BOTDR can also be applied to determine the location of optical fiber faults. The accuracy of the fault location depends on the spatial resolution, the quality of the optical fiber, and the signal intensity of the BOTDR. The shorter the measurement distance, the more accurate the identified fault location.
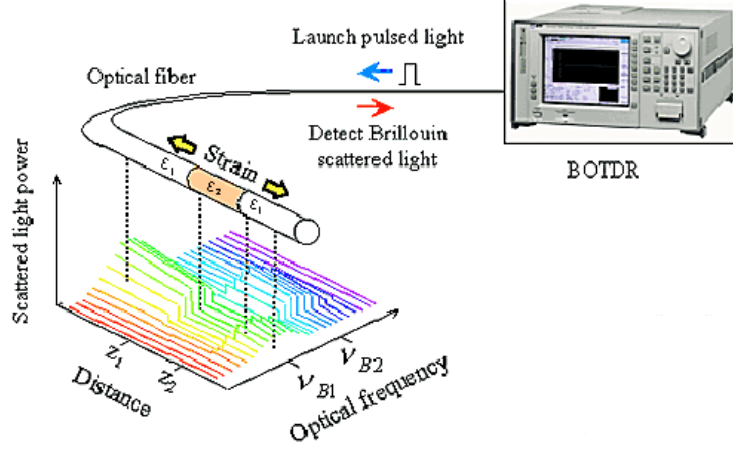
Fig. 1.5. Working principle of BOTDR technology.

1.3.3 PPP-BOTDR

To achieve high spatial resolution, PPP-BOTDA was developed by stimulating the phonons in an optical fiber with a pre-pump pulse before a narrow bandwidth pulse arrives [18]. In this way, the pump pulse length can be chosen to remain significantly shorter than the relaxation time of phonons, thus improving spatial resolution in distributed measurement, while the BGS becomes narrow due to stimulation of the pre-pump pulse and can be evaluated at high SNR. The combined effect of the pump and pre-pump pulses results in an immediate time response and a narrow BGS at the same time. In commercialized applications (Neubrescope) with a pulse of 0.2 ns width, 2 cm spatial resolution was achieved over 0.5 km measurement distance with 15 µε/ 0.75°C measurement accuracy for strain and temperature, respectively [19]. Compared with BOTDA in Fig. 1.3, PPP-BOTDA as schematically illustrated in Fig. 1.6 differs only in the shape of the pump pulse. The sensing principle of the PPP-BOTDA is the same as that of BOTDA as shown in Fig. 1.4. The probe light is CW.
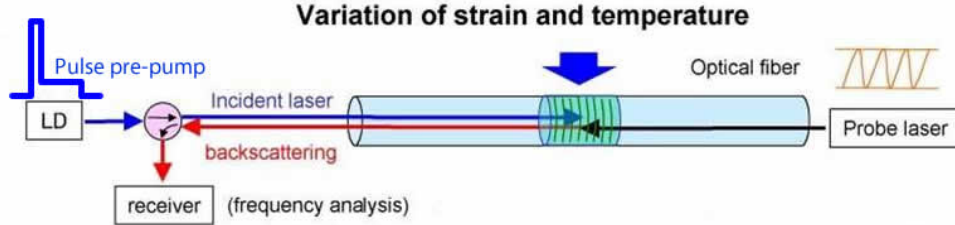
Fig. 1.6. A resentative PPP-BOTDA system.

Fig. 1.7 presents a general SBS model with detailed pump and probe light sources. The pump light with a leakage can be described as follows:

$$A_P(t) = \begin{cases} A_p + C_p, & D_{pre} - D \leq t \leq D_{pre} \\ C_p, & 0 \leq t \leq D_{pre} - D \\ 0, & \text{elsewhere} \end{cases}$$

(1.4)

where D and D_{pre} denote the pump pulse duration and the pre-pump duration, respectively. The extinct ratio, R_x, is defined as $(A_p + C_p)/C_p$.
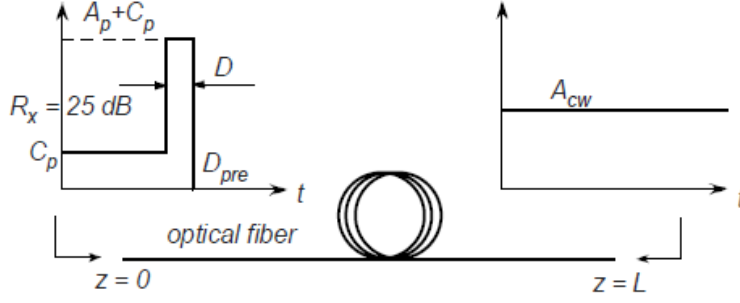
Fig. 1.7. A general SBS model.

The resulting Maxwell equation of the SBS model can be solved by means of the perturbation theory, leading to the following solution for amplitude of the probe light:

$$E_{CW}(0,t)=A_{CW}[1+\beta H(t,\ \Omega)] \tag{1.5}$$

The last term on the right-hand side of Eq. (1.5) represents the SBS effect. Here, β (= 2.2×10^{-4}) is the perturbation parameter, Ω is the frequency of phonons (the difference between frequencies of the pump and probe light), and t denotes time. In general, the $H(.,.)$ term can be expressed into a double integral of a pump profile $A(.)$ and a convolution of the pump profile with a phonon function $h(.,.)$:

$$H(t,\Omega)=\int_{0}^{L}A\left(t-\frac{2z}{\upsilon_g}\right)\int_{0}^{\infty}h(z,s)A\left(t-s-\frac{2z}{\upsilon_g}\right)dsdz \tag{1.6}$$

where v_g represents the light wave speed and $h(z, s)$ describes the phonon behavior as detailed by:

$$h(z,\ s)=\Gamma e^{-[\Gamma+i(\Omega_B(z)-\Omega)]s} \tag{1.7}$$

in which L is the length of the optical fiber, and $\Omega_B(z)$ is the Brillouin center frequency. Furthermore, $\Gamma = \Gamma_B/2$ and Γ_B is the full width at half of the maximum (FWHM) of a Brillouin spectrum. The power of Brillouin Gain Spectrum (BGS) can be expressed into:

$$V(t,\ \Omega)=0.5\beta A_{CW}^2 H(t,\ \Omega)+c.c. \tag{1.8}$$

If the pump profile shape is described by the step function in Eq. (1.4), $H(t,\ \Omega)$ can be expressed into:

$$H(t,\ \Omega) = H_1(t,\ \Omega) + H_2(t,\ \Omega) + H_3(t,\ \Omega) + H_4(t,\ \Omega) \tag{1.9}$$

where H_1 represents a narrow pump pulse leading to high spatial resolution and wide spectrum span, H_4 represents a pre-pump pulse leading to low spatial resolution and narrow spectrum span, H_2 represents their interaction that leads to high spatial resolution and narrow spectrum span, and H_3 indicates the effect of their interaction on vibration noise. The BGS power for various durations of the pre-pump pulse is presented in Fig. 1.8. The long duration of the pre-pump pulse results in a sharp BGS, giving a high accuracy in identification of the peak.
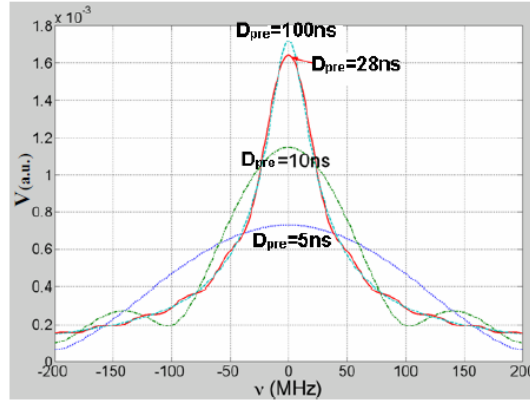
Fig. 1.8. Influence of pre-pump duration.

Fig. 1.9 shows a schematic design of a commercial PPP-BOTDA system (NBX-6000 model) by Neubrex Inc. To ensure that D_{pre} is of finite value, the pre-pumped composite pulse (represented by H_2) is considered to have the same area as the pump pulse (represented by H_1). As long as an optical fiber is longer than the corresponding pre-pump pulse, the BGS remains unchanged. The entire system is divided into four basic parts: user interface, data processing, signal processing/control, and light sources, receiver and recording. The interface part contains a notebook computer linked to the mainframe of PCI via a bridgeboard. This design allows one to increase the speed of data processing by upgrading the notebook computer over time. The digitizer has a bandwidth of 1 GHz, sampling rate of 2Gs, and memory of 4 Mb. With these specifications, the measurement time is within several minutes even over a long distance. Two wavelength lock LDs are adopted in NBX-6000 Model and the absolute wavelength control is performed individually. The precision is found to be within 1 MHz between two laser modules.
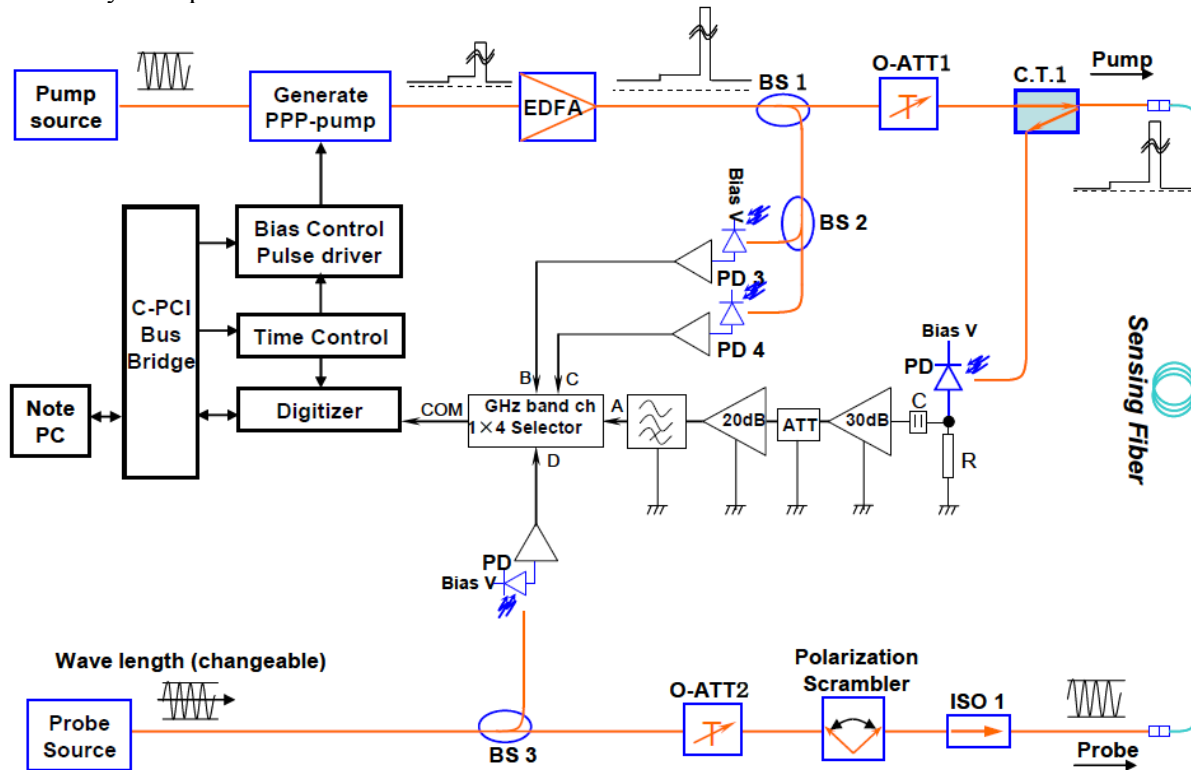
Fig. 1.9. Scheme of NBX-6000.

1.3.4 Comparison of Brillouin and Raman scatterings

The operation principles of Brillouin and Raman scattering based sensors differ significantly. In a distributed Brillouin scattering sensor, temperature change modifies the mean density of an optical fiber, which is associated with the velocity of sound, and thus influences the mechanical waves travelling in the optical fiber. Although influenced by the effective refractive index to some degree, the change in Brillouin frequency is dominated by the variation of density or sound velocity as a result of applied temperature and strain. In a Raman scattering sensor, temperature change induces the transition between rotation and vibration levels of molecules. The spectrum in Raman scattering is on the THz scale, while the spectrum in Brillouin scattering is on the MHz scale. Therefore, the Brillouin based distributed sensors are usually focused on the frequency measurement, *i.e.*, the Brillouin peak frequency shift due to strain or temperature effect, while the Raman scattering based sensors are on the power measurement over a wide frequency range (THz).

1.4 Tunable wavelength COTDR

In COTDR measurements, the Rayleigh backscattering signal and a reference signal are correlated and the frequency shift is determined by changing the laser frequency step by step [21-23]. The density (refractive index) fluctuations in an optical fiber are observed from the randomly distributed power spectrum with COTDR. A tunable wavelength COTDR (TW-COTDR) system utilizes the tunable wavelength of distributed feedback (DFB) laser and the frequency scanning for the improved regularity of the power spectrum. With distributed Rayleigh backscattering, the spectral shift distribution is modulated with strain and temperature changes along the optical fiber with 2 cm spatial resolution over 21 km measurement distance [25]. The intensity of Rayleigh scattering is three-order times stronger than that of Brillouin scattering in an optical fiber [56]. Hence, the accuracy of Rayleigh scattering based method is usually higher. Despite the accuracy and high spatial resolution over long distance, TW-COTDR has two disadvantages. First, scanning the frequency range takes significant time in each measurement. Second, the measurement may not be so reliable since the frequency shift is obtained by calculating the correlation between the Rayleigh backscattering and the reference signal. Since the strain or temperature distribution along the optical fiber is usually non-uniform, the correlation value is often low and the spectrum shift is difficult to determine precisely. In the extreme case when the deformation of an optical fiber is longer than the spatial resolution, different parts of the fiber are compared and their correlation can be zero [24]. As a result, TW-COTDR is typically not applied alone to solve practical problems.

1.5 FBG sensors

FBG sensors have been widely applied to measure the strain and the temperature of a test specimen at the location of attached and embedded sensors. Each FBG sensor measures a combined effect of strain and temperature averaged over the length of gratings. To separate the strain and temperature, two FBG sensors are often deployed side by side. One of the two sensors is attached to a test specimen such that is free of strain and measures the temperature change only for temperature compensation to the strain measurement of the other sensor. In a FBG sensor system, the grating portion is for sensing, and the remaining portion is for signal transmission by optic communication cables.

Bragg gratings are written over a segment of Ge-doped, photosensitive, single mode silica fiber so that a periodic modulation of core refractive index is formed by exposing the fiber to a spatial pattern of ultraviolet (UV) light in two ways: interference and masking. The amount of change in UV light is governed by the light intensity and exposure duration. In the interference method, a UV laser is split into two beams that interfere with each other, creating a periodic intensity distribution along the interference pattern. The refractive index of the photosensitive fiber changes according to the intensity of exposed light. This method allows for quick and easy changes to the Bragg wavelength, which is directly related to the interference period and a function of the incident angle of the laser light. In the phase mask method, a phase mask with intended grating features is placed between the UV light source and the photosensitive fiber. The shadow of the phase mask then determines the grating structure based on the intensity of

transmitted light that strikes the optical fiber.

According to Bragg's law, when a broadband source of light is injected into the fiber, a FBG sensor reflects a small part of light around certain wavelength, which is called the Bragg wavelength. The Bragg wavelength depends upon both the grating period and the refractive index of the fiber. A fiber Bragg grating can therefore be used as an inline optical filter to block certain wavelengths or as a wavelength-specific reflector.

Fig. 1.10 shows the operational principle of FBG sensors. At each periodic refraction change due to gratings, a small amount of light is reflected, collectively forming a coherent large reflection at the Bragg wavelength. Light signals at wavelengths other than the Bragg wavelength propagate through the gratings with negligible attenuation or signal variation. The ability to accurately preset and maintain the grating wavelength is a fundamental feature and advantage of FBG sensors. Fig. 1.11 shows the reflection spectrum of a typical FBG sensor. The Bragg wavelength of the reflected component satisfies the Bragg condition:

$$\lambda = 2n\Lambda \tag{1.10}$$

where n is the refractive index and Λ is the grating period of the FBG.
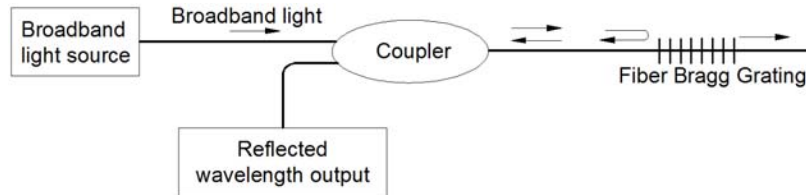
Fig. 1.10. Working principle of a typical FBG sensor.
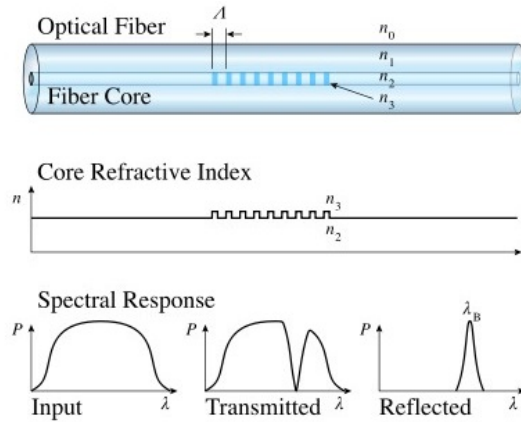
Fig. 1.11. A FBG structure with refractive index profile and spectral response.

Due to mechanical and/or thermal effects such as strain and/or temperature, the grating period Λ varies at the location of gratings. As a result, the wavelength of the reflected spectrum changes as a function of strain and/or temperature. The wavelength changes for an FBG strain sensor and a temperature compensation sensor can be respectively written as:

$$\frac{\Delta\lambda_1}{\lambda_1} = (1 - P_e)\varepsilon + (\alpha + \varsigma)\Delta T \tag{1.12}$$

$$\frac{\Delta\lambda_2}{\lambda_2} = (\alpha + \varsigma)\Delta T \tag{1.13}$$

where λ_i and $\Delta\lambda_i$ (i=1, 2) represent the Bragg wavelength and its change, respectively; ς, α, and P_e

denote the thermal-optics coefficient, the thermal expansion coefficient, and optical elasticity coefficient, respectively; and ε and ΔT are the changes in applied strain and temperature, respectively. Therefore, the strain after temperature compensation can be calculated by:

$$\varepsilon = \frac{1}{(1-P_e)}(\frac{\Delta\lambda_1}{\lambda_1} - \frac{\Delta\lambda_2}{\lambda_2}) \tag{1.14}$$

Chapter 2 Data acquisition systems and optical fiber sensors

A hybrid technology of PPP-BOTDA and TW-COTDR was made commercially available by Neubrex Inc., Japan, in 2011. It was applied to measure the strain distribution with a single mode optical fiber in concrete pavement. Its performance was compared with that of FBG sensors with an optical sensing interrogator sm125. In this chapter, both data acquisition systems and the utilized optical fiber sensors are discussed.

2.1 Data acquisition systems

2.1.1 Neubrescope NBX-7020

Neubrescope NBX-7020 combines four distributed optical fiber sensing technologies: PPP-BOTDA, BOTDR, TW-COTDR, and COTDR. When a hybrid mode of PPP-BOTDA and TW-COTDR is triggered, simultaneous strain and temperature measurements and discriminations can be realized based on the different strain and temperature coefficients between Brillouin and Rayleigh scatterings. NBX-7020 has the following technical specifications: up to 25 km measurement distance, up to 1 cm readout resolution, up to 2 cm spatial resolution, -3% to 4% strain range for PPP-BOTDA and -1.5% to +2% for TW-COTDR. With strain-free UV coated fibers, the measurement accuracy and repeatability for PPP-BOTDA are 7.5με /0.35ºC and 5με/0.25ºC; the measurement accuracy and repeatability for TW-COTDR are 0.5με/0.05ºC and 0.2με/0.01ºC; the measurement accuracy and repeatability for hybrid mode are 10με/0.5ºC and 5με/0.25ºC.

NBX-7020 as shown in Fig. 2.1 provides multiple measurement modes: standard mode, frequency sweep (FS) mode, and amplitude transfer (AT) mode. The FS mode can be used to measure an arbitrary strain distribution. The AT mode is a non-standard measurement mode. Instead of frequency scanning in FS mode, the AT mode measures the amplitude at a single frequency and determines the frequency shift using the pre-determined shape of Brillouin power spectrum. It is valid for specific strain distributions to expedite the measurement process.

Fig. 2.1. Neubrescope NBX-7020.

2.1.2 Optical sensing interrogator sm125

The sm125 interrogator as shown in Fig. 2.2 is a compact and industrial grade static optical sensor interrogation module designed for reliable, long term field operation. The Micron Optics "sm-sensing module" platform responds directly to the user commands of the optical interrogator core and outputs

sensor wavelength data via Ethernet port and custom protocol. All module settings, sensor calculations, data visualization, storage, and alarming tasks are run on an external PC or sensor processor module. The sm125 optical sensing interrogator is built upon the Micron Optics x25 optical interrogator core. The x25 interrogator core employs full spectral scanning and data acquisition, providing measurements with high absolute accuracy, flexible software post-processing, and high dynamic range performance. The "x25" based interrogators support continuous on-board NIST traceable wavelength reference components and are ideally suited to measure many different optical sensors, including FBGs, long period gratings, and extrinsic Fabry-Perot interferometers. The sm125 has four optical channels with a scan frequency of 1Hz and a wavelength range of 1510nm to 1590nm.

Fig. 2.2. Optical sensing interrogator sm125.

2.2 Distributed optical fiber sensors

The flexible optical fibers used in this study are made of high quality extruded silica glasses including a transparent core surrounded by a transparent cladding layer. Typically, the refraction index of the core is higher than that of the cladding so that total internal reflection (TIR) takes place and the light beam can be kept in the core as shown in Fig. 2.3. Therefore, optical fibers are often referred to as a waveguide. In terms of the propagation mode, optical fibers can be classified to be multi-mode fibers (MMFs) and single mode fibers (SMFs). The structure of a SMF is shown in Fig. 2.3. The diameters of the core and the cladding are 9 μm and 125 μm, respectively. Usually there is a protective coating layer outside the cladding.
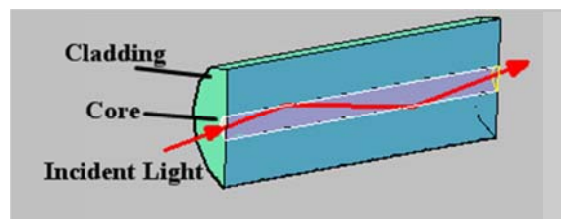
Fig. 2.3. Schematic of TIR in an bare optical fiber.

Optical fibers have many advantages, such as immune to EMI, compact, light, and robust in harsh environment. Thus, optical fiber sensing technologies have been widely studied worldwide and applied in real world structures. In this study, three types of optical fibers were investigated as distributed sensors: Corning bare SMF-28e^{+} fiber (BF), SMF-28e^{+} fiber with a tight buffer (TB), and FN-SIL-1 concrete crack cable (CC). Their specifications are listed in Table 2.1.

Table 2.1 Specifications of selected optical fibers

Optical fiber type	Bare SMF-28e$^+$ fiber (BF)	SMF-28e$^+$ fiber with tight buffer (TB)	FN-SIL-1 concrete crack cable (CC)	
			SM FG-SR15 with tight buffer	SM FG-SR15 with loose buffer
Cladding diameter	125 ± 0.7 μm	125 ± 0.7 μm	125 ± 0.7 μm	125 ± 0.7 μm
Coating material	Acrylics	Acrylics	Acrylics	Acrylics
Coating diameter	242 ± 5 μm	242 ± 5 μm	242 ± 5 μm	242 ± 5 μm
Secondary coating diameter	0.9 ± 0.1 nm	0.9 ± 0.1 nm	0.9 ± 0.1 nm	0.5 ± 0.1 nm
Coating process	Ultraviolet (UV)	Ultraviolet (UV)	Ultraviolet (UV)	Ultraviolet (UV)
Buffer material	---	Polyethylene	Polyethylene	Polyamide (nylon)
Buffer diameter	---	880 ± 10 μm	850 ± 10 μm	480 ± 10 μm
Cut off wavelength	< 1260 nm	< 1260 nm	< 1260 nm	< 1260 nm
Attenuation	< 0.2 dB/km (1550 nm)	< 0.2 dB/km (1550 nm)	< 0.5 dB/km (1550 nm)	< 0.5 dB/km (1550 nm)
Temperature range	-60 to + 85 $^\circ$C	-20 to + 60 $^\circ$C	-20 to + 60 $^\circ$C	-20 to + 60 $^\circ$C
Manufacturer	Corning Inc.	---	Fujikura Ltd.	

(1) Bare SMF-28e$^+$ fiber

Corning BF is produced with a polymeric coating in place to protect the glass surface. A dual-layer coating system is adopted. The glass is coated with an inner primary coating which is usually made of soft and rubbery material that cushions the glass from external mechanical loads. The inner primary coating is surrounded by an outer primary layer which is made of much stiffer material, which is used to protect the fiber from abrasion and environmental exposure. Both coatings are composed of complex mixtures of raw materials (monomers, oligomers, photoinitiators, and additives). The cross section of a BF is shown in Fig. 2.4. The primary and secondary coatings are sequentially applied in a liquid form as the glass fiber is drawn and individually cured by UV light sources.
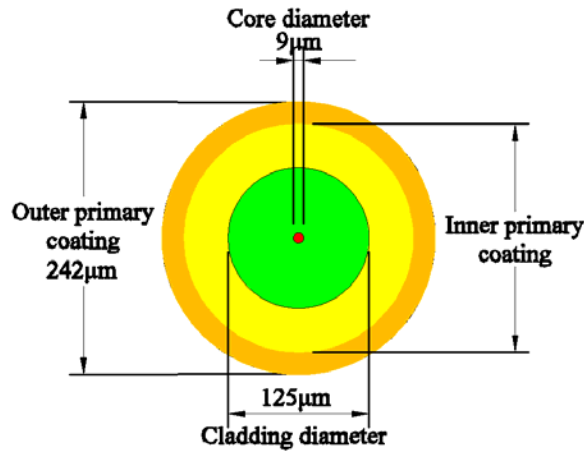
Fig. 2.4. Schematic of the cross section of a BF.

(2) SMF-28e$^+$ fiber with tight buffer

Due to the fragility of bare SMF-28e$^+$ fibers, the SMF-28e$^+$ fiber with tight buffer, as shown in Fig. 2.5, were invented by uniformly and tightly coating a layer of polyethylene on the bare SMF-28e$^+$ fiber. Due to its elasticity, the polyethylene buffer can uniquely transfer strain from the surface of the buffer to the fiber and thus doesn't compromise the sensing ability of the fiber. In addition, the buffer can significantly enhance the tensile strength and shear strength of the coated fiber, and thus reduce the risk of sensor damage during handling, transportation, and installation.
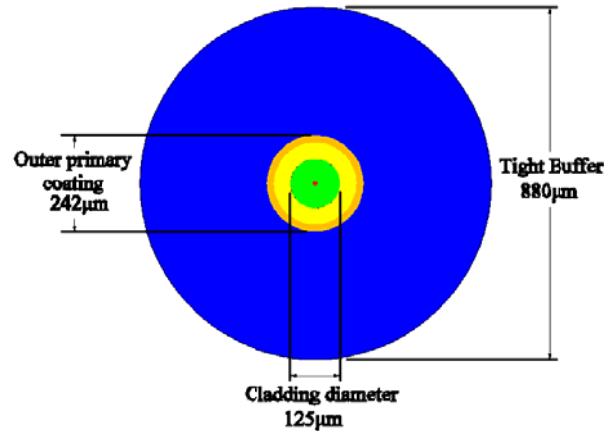
Fig. 2.5. The cross section of a TB.

(3) FN-SIL-1 concrete crack cable
As shown in Fig. 2.6, FN-SIL-1 concrete crack cable consists of one SMF FG-SR15 with a white tight buffer which can sense both strain and temperature, one SMF FG-SR15 with a green loose buffer for temperature compensation, and an outside protective tight sheath.
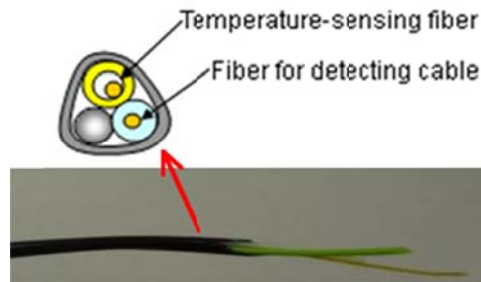
Fig. 2.6. Schematic of a CC.

2.3 Fiber Bragg grating sensors

One dimensional (1D) and three dimensional (3D) FBG sensors as shown in Fig. 2.7, each coated with a glass fiber reinforced polymer (GFRP) protective layer, were purchased from a company in Harbin, China, and used in this study to measure strains in concrete overlays. In each 3D-GFRP-FBG sensor, one short gauge is intended to monitor the vertical strain and two long gauges are used to monitor the horizontal strains of a host structure in two directions. Limited by the 7.5 cm thick concrete overlay in this application, the vertical sensor was designed and fabricated with a total length of 5 cm including the length of the GFRP holder. Reflective FBG signals from all of the three gauges will be taken from an optical signal analyzer (OSA) and recorded by a laptop computer for post data processing.
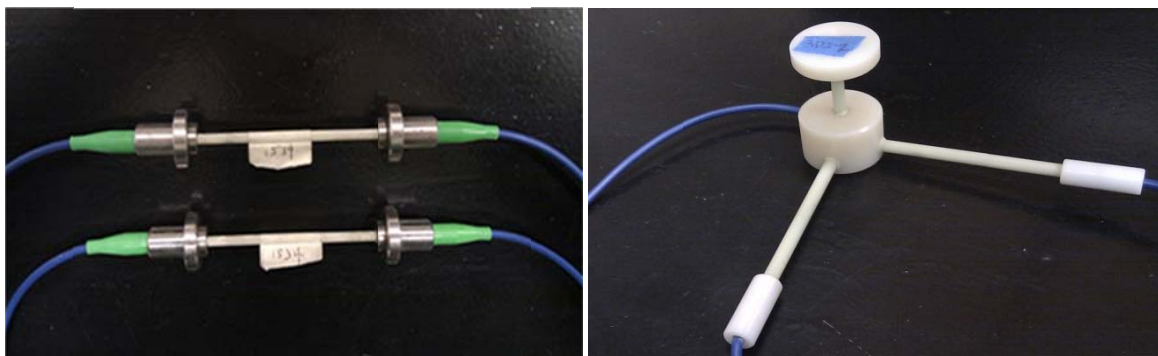
(a) 1D FBG sensor   (b) 3D FBG sensor
Fig. 2.7. Photograph of the FBG sensors.

16

The wavelength sensitivity coefficient of the FBG sensors is 7.937×10^{-4} nm/$\mu\varepsilon$ for strain measurement and 0.0104 nm/°C for temperature measurement. Although responsive to both strain and temperature, the FBG sensors are more sensitive to temperature change than to strain change. Therefore, when FBG sensors are used to monitor strain change, the temperature effect must be monitored simultaneously for temperature compensation. In general, two FBG sensors are deployed side by side with one isolated from straining for temperature compensation purpose and the other for strain measurement. They must be co-located in an area with the same temperature change.

When used as strain sensors, FBG sensors measure the strain change within their gauge length and thus provide their average values over the gauge length. Since the gauge length is usually short as indicated in Fig. 2.8, the FBG sensors can provide reasonable results for one location unless the strain suddenly changes in a short distance, for example, around a crack. As such, these sensors are referred to as point sensors at the location of their installation. The strain transfer mechanisms for embedded point sensors and surface attached sensors have been studied [61].

(a) Elevation view of 3D FBG   (b) Plan view of 3D FBG   (c) Elevation view of 1D FBG
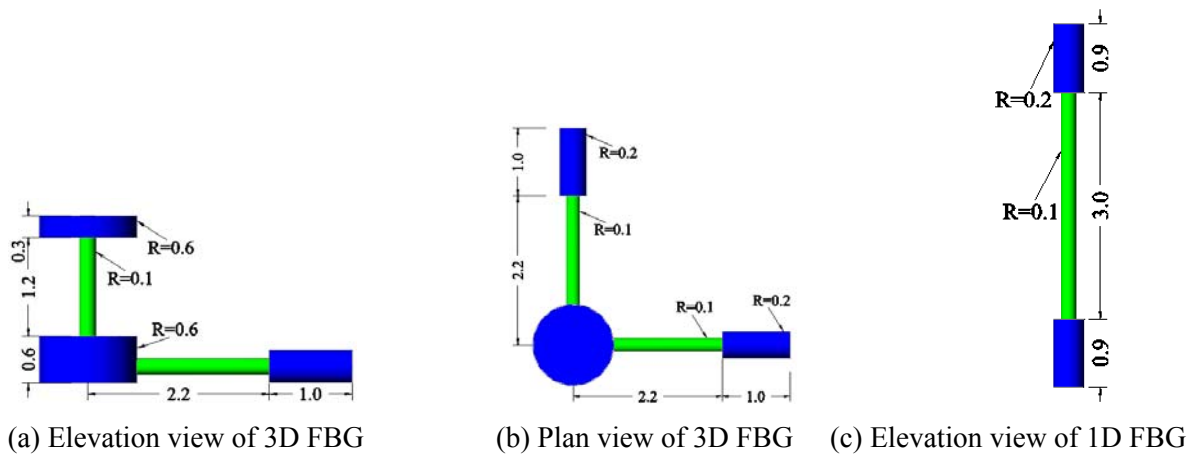
Fig. 2.8 Configuration and geometry of FBG sensors (in inch = 2.5 cm).

Chapter 3 Characterization of distributed optical fibers

The three types of optical fibers were characterized at room temperature (21 °C) using a low capacity load frame known as Instron 5965. They were axially loaded in tension and measurement data were obtained. A Neubrescope was used to take strain data based on the PPP-BOTDA technology with 2 cm spatial resolution.

Instron 5965 as shown in Fig. 3.1 is a low capacity load frame with 5 kN capacity. The load measurement accuracy of Instron 5965 is ±0.5% of reading down to 1/1000 of load cell capacity option (2580 Series load cells). It has up to 2.5 kHz data acquisition rate simultaneous on load, extension, and strain channels, a load rate of 0.001-3000 mm/min (0.00004-120 in/min), and an automatic transducer recognition for load cell and extensometer.

Two tests were run for each type of optical fibers: mechanical test and optical-mechanical test. For mechanical tests, each fiber was loaded in tension to failure in displacement-controlled mode. The loading rate was 2 mm/min. The load-extension relation was obtained directly and transferred to the load-strain relation when the initial length of each fiber was measured. Therefore, the tensile strength and the elastic limit of strain ε_e can be determined. Once ε_e was known from the mechanical test, a small portion of it was applied during the optical-mechanical test at strain increment $\Delta\varepsilon$. In this case, strains were simultaneously measured from the optical fiber with the Neubrescope and with load cell and extensometer of the Instron 5965. The measurements were conducted incrementally until enough data points were collected.
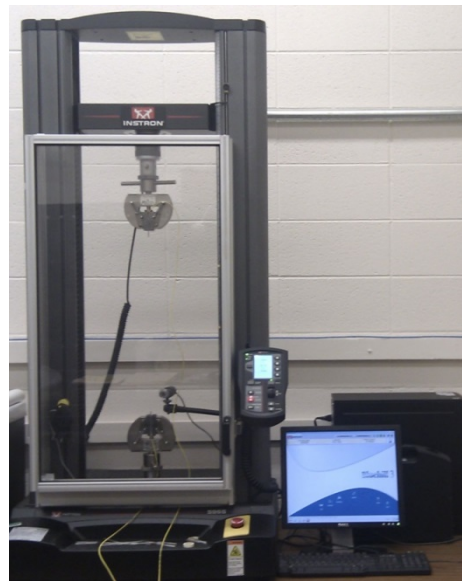
Fig. 3.1. Load frame (Instron 5965).

3.1 Bare SMF-28e$^+$ fiber

3.1.1 Tensile tests

Mechanical properties of Corning BF were characterized at room temperature (21°C) with tensile tests in the laboratory. Fig. 3.2 shows the test setup and the cross section of the tested fiber. Each end of the fiber was spliced with a communication cable that was instrumented with a FC/APC connector. Considering the fragility of the BF, the portions of the fiber in direct contact with the Instron grips were protected with sleeves that can be directly gripped by the fixture of the load frame. The loading force and the extension were simultaneously recorded by the load transducer and the extensometer.
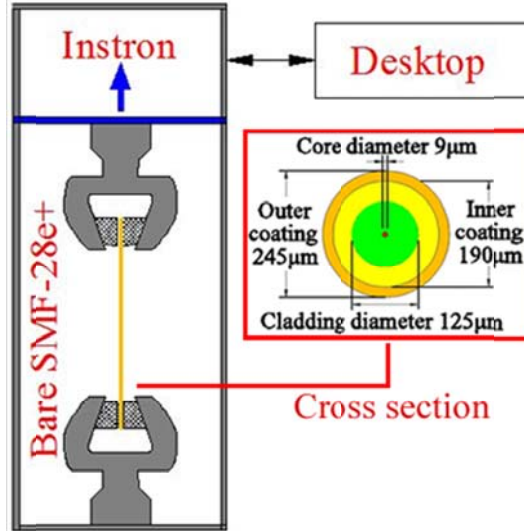
Fig. 3.2 Test setup and fiber cross section.

Ten fibers were tested to failure. Figs. 3.3(a, b) present the force-strain relation of a representative fiber and the linear regression for its linear portion, respectively. The optical fiber behaved linearly until ε_e and soon fractured with a suddenly reduced load that was resisted solely by the coating. The tensile strength of the fiber was approximately 15 N and the corresponding strain was $\varepsilon_e = 16,000$ µε (1.6%). An initial slope of 9.63×10^{-4} N/µε has been obtained from the force-strain curve by a linear regression technique as shown in Fig. 3.3(b). This value can be taken as the tensile stiffness of the optical fiber. The tensile strengths and their corresponding strains of the ten fibers are summarized in Figs. 3.3(a, b), respectively. The average tensile strength of the ten fibers is 12.68 N, and the average ε_e is 1.31×10^4 µε.

(a) Complete loading process

(b) Linear protion with regression analysis
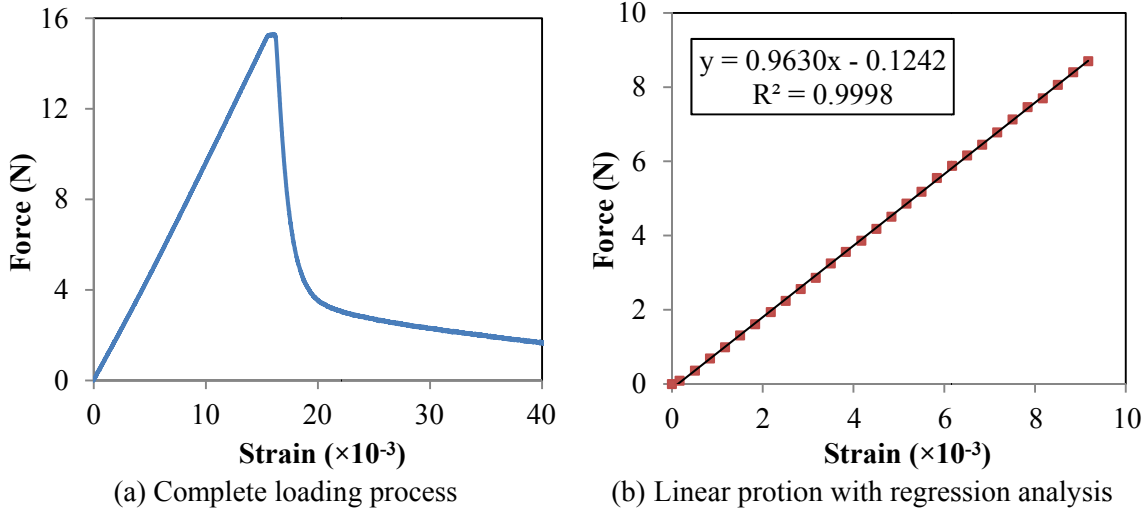
Fig. 3.3. Force-strain relation of a BF sensor.

19

(a) Tensile strength   (b) Strain at the elastic limit
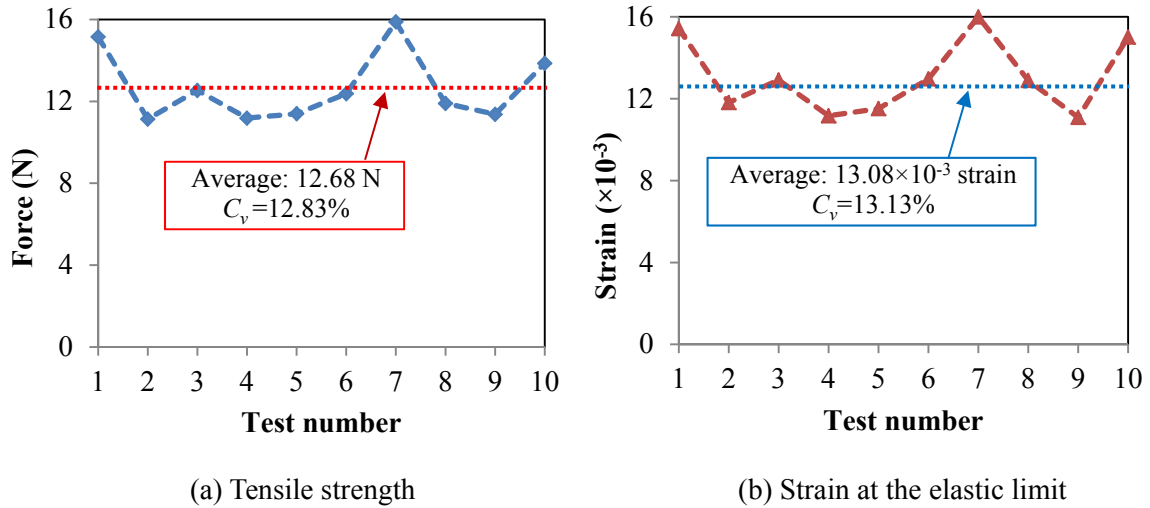
Fig. 3.4. Test results from ten fibers.

The coefficient of variation (C_V) is a normalized measure of the relative dispersion of various measurement data for one variable. Fig. 3.5 shows the glass fibers before and after load testing and indicates that the fiber has been pulled out of the coating during the test. Due to the stress concentration, the coating was broken at the end of a protective sleeve where the geometry suddenly changes. When not perfectly straight in the test setup, the optical fiber in tension will be subjected to bending. As a result, the measured strength could be lower than its actual value due to additional bending stress. In this sense, the test may underestimate the capacity of optical fibers, and thus the estimated load capacity is conservative. Therefore, another test was conducted to address this.
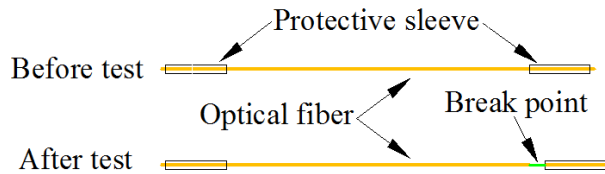
Fig. 3.5. Schematic of the failure mode of a BF.

Fig. 3.6 shows the second test setup. In this case, the two ends of an optical fiber were wrapped on PVC pipes that were fixed by grips of the load frame. The force-strain relation of a representative BF is presented in Fig. 3.7(a). With this test setup, ten additional optical fibers were loaded to failure again. Local slippages were observed during the test and reflected on the force-strain relation as shown in Fig. 3.7(a). Because of slipping, the force-strain relation in Fig. 3.7(a) may not be as reliable as that in Fig. 3.3(a). Therefore, only the load capacity was used in analysis as summarized in Fig. 3.7(b) for ten tested optical fibers. It can be observed from Fig. 3.7(b) that a higher load capacity was obtained in comparison with that of the first test setup in Fig. 3.4(a). The actual load capacity is expected in between the two tests. For conservativeness, the results from the first test setup were considered in this study.
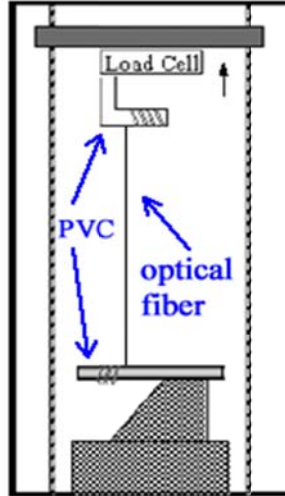
Fig. 3.6. Tensile test setup with a bare SMF-28e$^+$ fiber wrapped on a circular pipe.

(a) Force-strain relation   (b) Peak load in elastic range
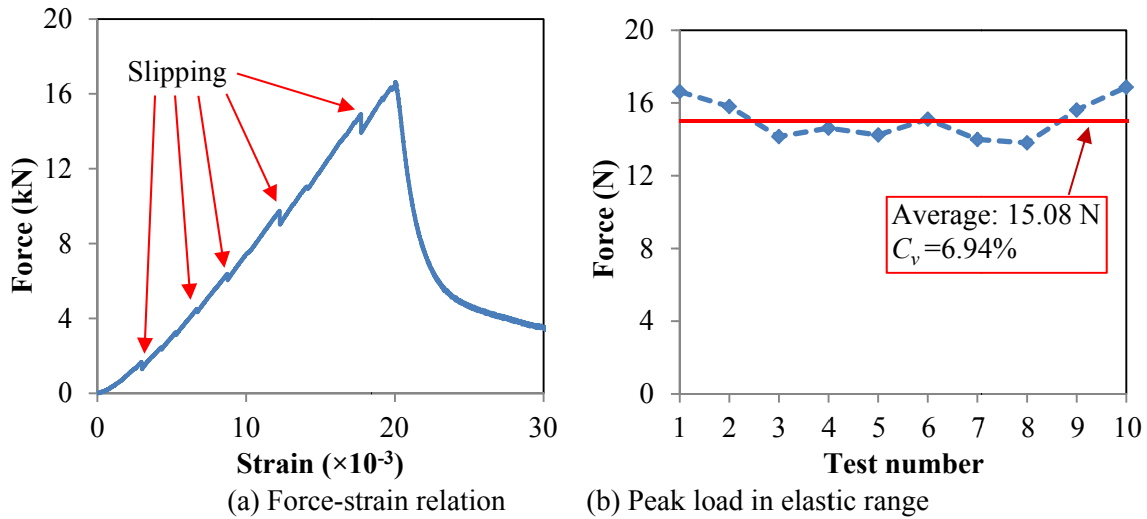
Fig. 3.7. Tensile test results with a bare SMF-28e$^+$ fiber wrapped on a round pipe.

3.1.2 Strain measurement with PPP-BOTDA

The elastic limit strain ε_e that was obtained from the mechanical tests was incrementally applied on optical fibers at constant increment so that enough data points can be collected before the optical fiber was broken. The fiber was loaded in tension with strain increment $\Delta\varepsilon$ step by step. The test setup in this case is illustrated in Fig. 3.8. In each test, the strain in the optical fiber was simultaneously taken with the Neubrescope and the Instron. The Neubrescope measures the Brillouin frequency shift that can be modulated with the strain change when the ambient temperature is kept constant. The Instron measures the applied strain on the optical fiber. Together, the Neubrescope and the Instron can give a calibration strain-frequency sensitivity coefficient. Fig. 3.9 shows the Brillouin frequency shift as a function of the applied strain obtained from the Instron. The data used to generate Fig. 3.9 were taken at the mid-point of the tensioned portion of each fiber. The slope represents a strain-frequency sensitivity coefficient of 5.41×10^{-5} GHz/$\mu\varepsilon$ by linear regression.

21
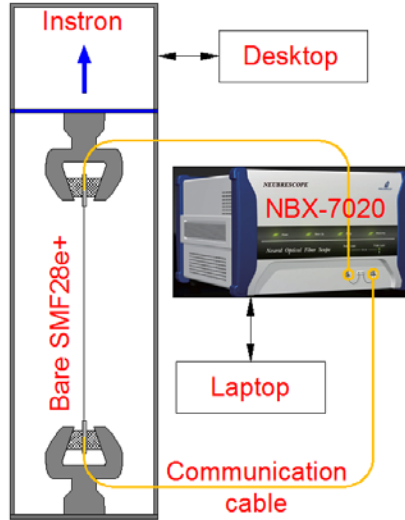
Fig. 3.8. Calibration test setup.

$$y = 0.0541x + 0.0016$$
$$R^2 = 0.9998$$
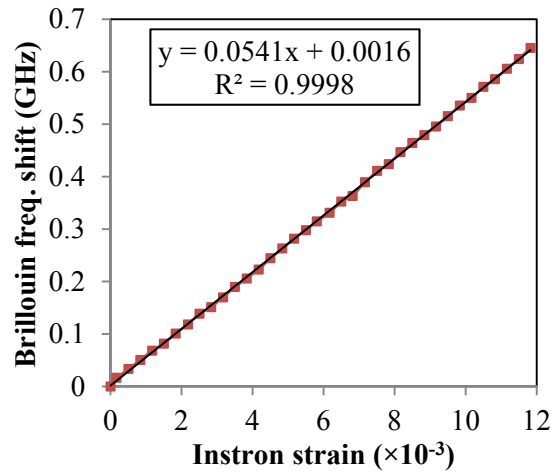
Fig. 3.9. Frequency shift from PPP-BOTDA as a function of applied strain change in a BF.

3.1.3 Features

(1) Accuracy

As indicated in Fig. 3.9, the Brillouin frequency shift and the applied strain are well correlated with R^2=0.9998. This indicates that the frequency shift can be used as an effective indicator to the strain applied on the bare SMF-28e$^+$ fiber. The strain distributions along the fiber length were shown in Fig. 3.10 from three tests of one optical fiber with PPP-BOTDA measurements. A peak-to-peak 110 $\mu\varepsilon$ variation can be observed in Fig. 3.10 at a measurement strain level of approximately 1000 $\mu\varepsilon$. If the middle portion from 3.78 to 4.24 m is concerned, the peak-to-peak variation becomes less than 10% of the strain to be measured. In this case, the accuracy of any point in comparison with the average value is about 5% of the measured strain or 50 $\mu\varepsilon$ in comparison with the 10 $\mu\varepsilon$ accuracy specified by Neubrex Co. Ltd. The reduced accuracy may be attributed to the environmental vibration from and around the load frame. Because of the vibration, the fiber could be subjected to various conditions at different points of the fiber even during one measurement using PPP-BOTDA. In addition, signal processing techniques, such as de-noising algorithms, can be adopted to reduce the variation in strain distribution. A trade-off in this case is to avoid the filter-out of useful information related to spatial distribution of strains in applications.
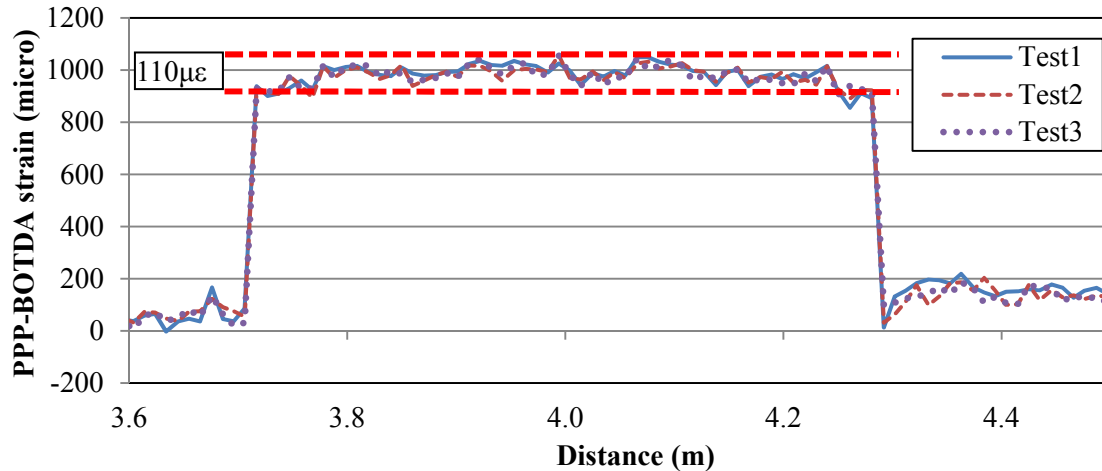
Fig. 3.10. Three measurements from the bare SMF-28e$^+$ fiber.

(2) Repeatability

As shown in Fig. 3.10, the repeatability for three strain measurements has been demonstrated to be around 5-20 με, which also does not satisfy the expected repeatability (1-10 με) from the datasheet of NBX-7020. Again, the results could be influenced by the environmental vibration.

(3) Resolutions

For PPP-BOTDA measurements, up to 1 cm readout resolution and 2 cm spatial resolution can be realized for UV coated SMF. Along the fiber, one data point is collected every centimeter, and the strain values of any two points with a distance no less than 2 cm are expected to be distinguishable.

(4) Ruggedness

The bare SMF-28e$^+$ fibers can withstand a load of up to 16 N or a strain of up to 1.6% as shown in Figs. 3.4 and 3.7. This level of measurement range is sufficient for most applications where moderate inelasticity is involved in structures. Therefore, the fibers are considered rugged in tension. The average force limit in elastic range was 12.68 N. The average strain limit in elastic range was 13,080 με (1.3%).

3.2 SMF-28e$^+$ fiber with tight buffer

3.2.1 Tensile test

The mechanical properties of TB fibers were tested under tension as illustrated in Fig. 3.2. Ten fibers were tested to failure and the force-strain relations were obtained. A representative force-strain relation was presented in Fig. 3.11(a) from which it was observed that the tensile strength of the fiber was around 20 N and the corresponding strain was around 20,000 με (2%). The slope of the linear portion by regression was 9.76×10^{-4} N/με as shown in Fig. 3.11(b). The force capacities and strains corresponding to the breakpoint of ten fibers are summarized in Fig. 3.12.
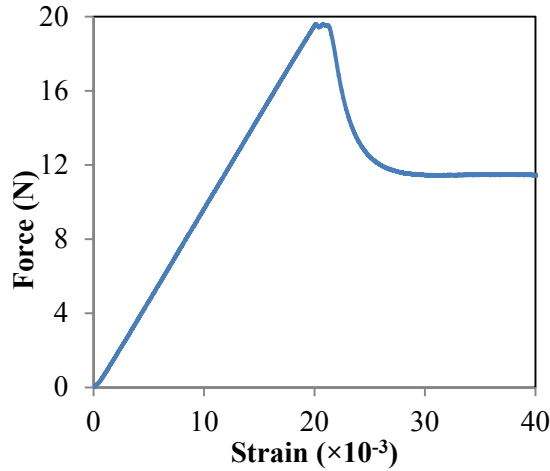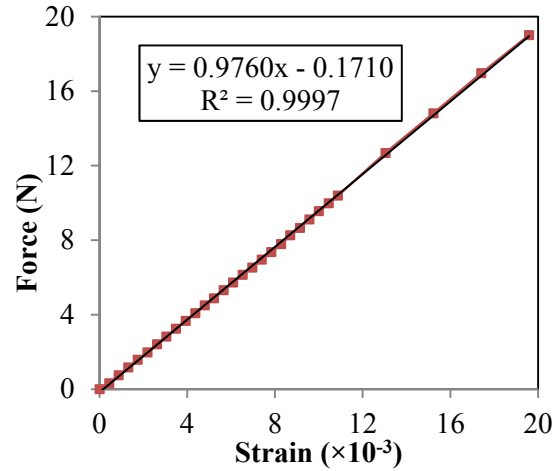
(a) Complete loading process　　　　　(b) Linear portion with regression analysis

Fig. 3.11. Force-strain relation of a TB sensor.
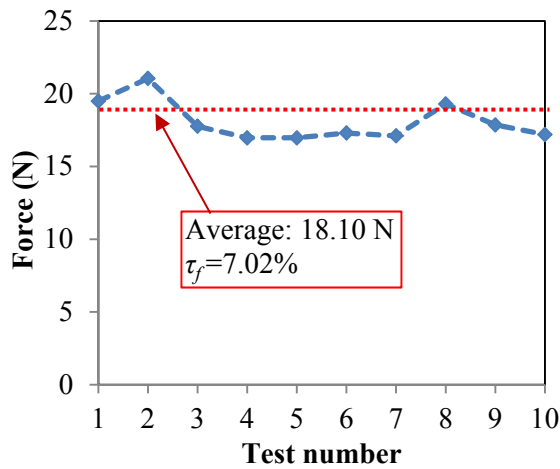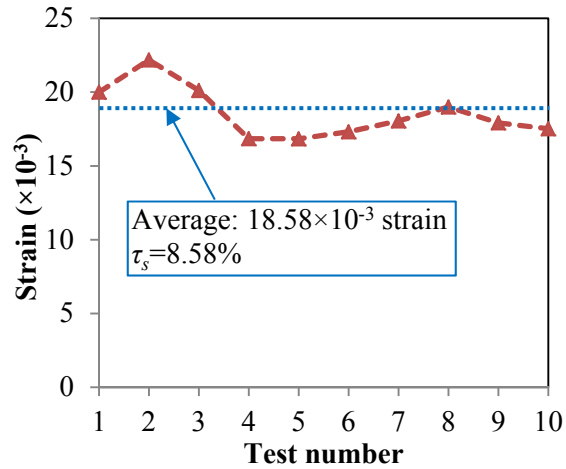
(a) Tensile strength　　　　　(b) Strain at the elastic limit

Fig. 3.12. Tensile test results of ten fibers.

Fig. 3.13 showed that the fiber was broken within the protection sleeve. For the ten tested fibers, the breakpoint of each fiber was within the protection sleeve at one of the two ends.
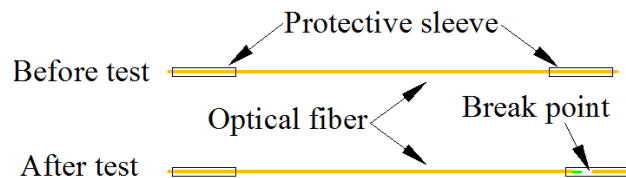
Fig. 3.13. Schematic of the failure mode of a TB.

3.2.2 Strain measurement with PPP-BOTDA

The elastic limit strain ε_e that was obtained in the calibration tests was evenly divided into strain increment during testing. That is, each fiber was loaded in tension at the strain increment $\Delta\varepsilon$ by the Instron step by step. In each measurement, the strain in the optical fiber was simultaneously measured by both the Neubrescope and the Instron. Fig. 3.14(b) shows the Brillouin frequency shift as a function of the applied strain obtained from the Instron. The frequency-strain sensitivity coefficient is 4.66×10^{-5} GHz/$\mu\varepsilon$.

The sensitivity coefficient was used to convert the Brillouin frequency shift from PPP-BOTDA measurement in application into the applied strain on the optical fiber as presented in Fig. 3.14(a) for strain distributions over the length of the optical fiber.
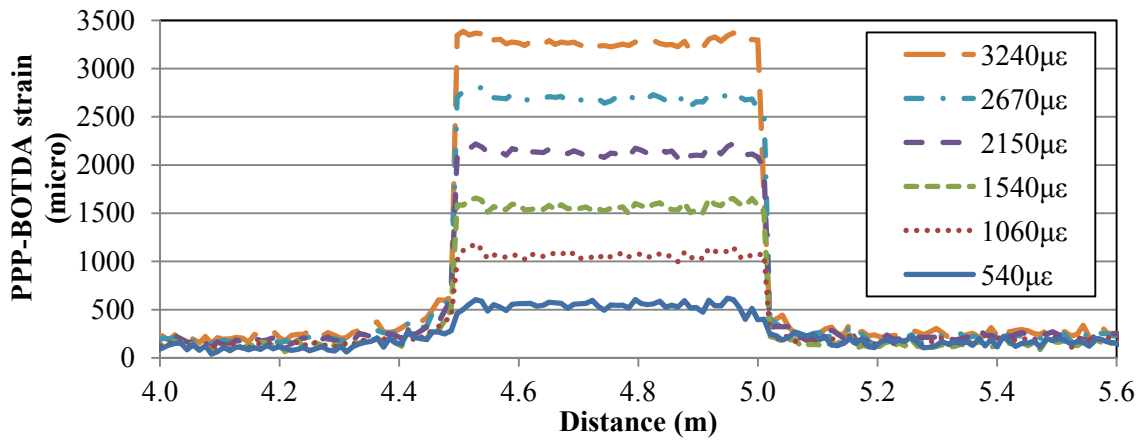
(a) Strain distribution along the length of the optical fiber
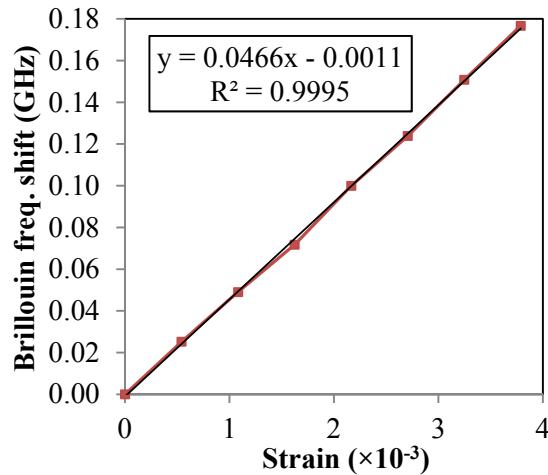
(b) Frequency shift with strain change

Fig. 3.14. Calibration of the SMF-28e$^+$ fiber with tight buffer with PPP-BOTDA.

3.2.3 Features

(1) Accuracy

Fig. 3.14 shows a good linear relation between the Brillouin frequency shift and the applied strain on the optical fiber. The spatial distributions of the strains from three tests of an optical fiber were shown in Fig. 3.15 with PPP-BOTDA measurements. In this case, the peak-to-peak strain variation is 110 με over the entire length of the optical sensor and less than 80 με in the range of 4.52 to 4.94 m. The average strain of the three measurements is approximately 2200 με. Therefore, the measurement accuracy about the average value is approximately 40 με in the middle portion of the optical fiber or 1.9% of the measured strain.

(2) Repeatability

The repeatability of three strain measurements at one point was observed to be around 5-20 με as shown in Fig. 3.15. Although worse than 1-10 με in the datasheet of NBX-7020, this level of repeatability seems acceptable for most applications in civil engineering.
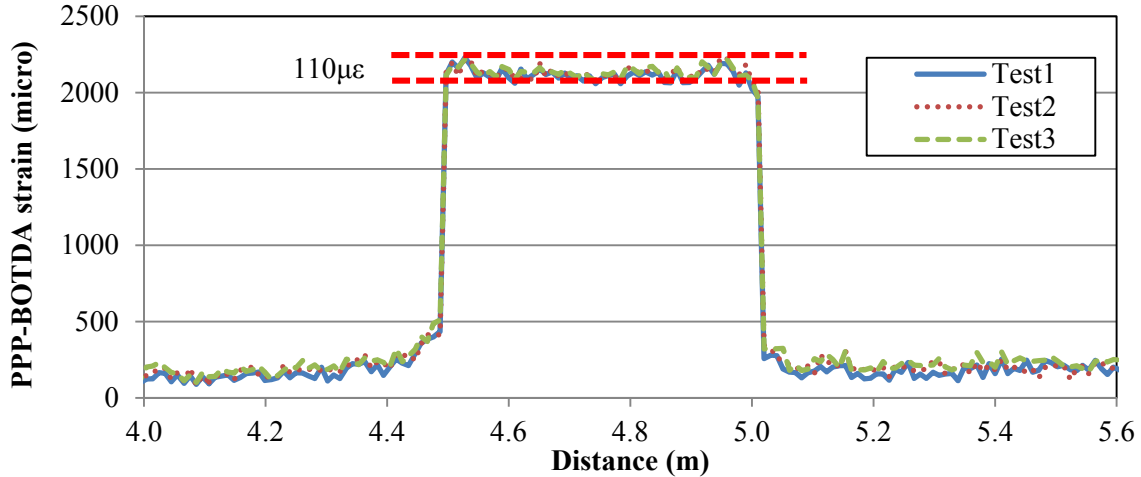
Fig. 3.15. Three measurements from the SMF-28e$^+$ fiber with tight buffer.

(3) Resolutions

For PPP-BOTDA measurements, one data point is collected every centimeter, and the strain values of any two points with a distance of less than 2 cm are distinguishable. These results indicate that the 2 cm spatial resolution is achieved in the strain measurement for the UV coated SMF.

(4) Ruggedness

SMF-28e$^+$ fibers with tight buffer were observed rugged in tension. Fig. 3.12 indicated that the average peak force in elastic range was 18.10 N and the average peak strain in elastic range was 18.58 με (1.8%). They are significantly more rugged than the bare optical fibers.

3.3 FN-SIL-1 concrete crack cable

3.3.1 Tensile test

FN-SIL-1 concrete crack cable was tested in the similar way to other optical fibers. Each optical fiber was loaded in tension to failure. The force-strain relations were obtained as shown in Fig. 3.16. It can be observed from Fig. 3.16 that the tensile stiffness was about 1.08×10^{-3} N/με. The FN-SIL-1 cable is slightly stiffer than the bare SMF-28e+ and the SMF-28e+ with tight buffer.
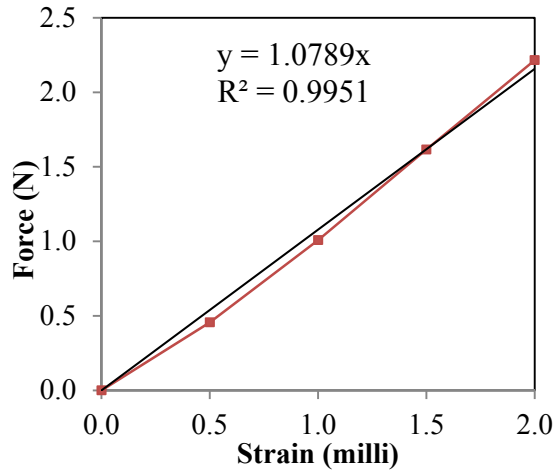
Fig. 3.16. Tensile test results of the FN-SIL-1 concrete crack cable.

3.3.2 Calibrations of strain measurement with PPP-BOTDA

For each test, both the Brillouin frequency shift by PPP-BOTDA and the applied strain by the Instron were recorded simultaneously. They are plotted in Fig. 3.17 with high degree of linearity. The frequency-strain coefficient of the slope of the linear regression line is 1.21×10^{-5} GHz/$\mu\varepsilon$.
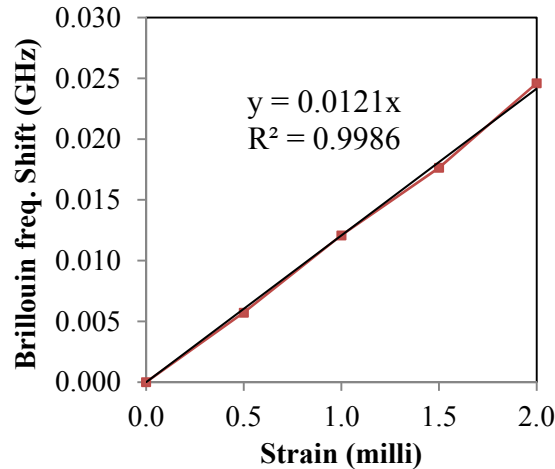
Fig. 3.17. Calibration of the FN-SIL-1 concrete crack cable with PPP-BOTDA.

3.4 Summary

The BF, TB and CC sensors were loaded to failure to characterize their mechanical properties with a low capacity load frame. The Brillouin frequency shift in PPP-BOTDA measurement was calibrated with the applied strain measured from the load frame. Their accuracies and ruggedness for strain measurement are compared.

Among the three types of fibers, the BF was most flexible and fragile but most sensitive to strain change. The CC was most rugged but least sensitive and robust in strain measurement. The ruggedness and sensitivity of the TB were in between the BF and the CC. The Brillouin frequency shift from each of the three types of optical fibers can be well correlated linearly with the applied strain by the load frame.

Chapter 4 Fabrication of specimens

To protect optical fibers from damage during construction, a special installation procedure was developed and successfully implemented as illustrated in Fig. 4.1. Applicable to real world pavement monitoring, the proposed installation method was applied to successfully embed three types of optical fibers (BF, TF, and CC) in full-size concrete panels used in rehabilitation of existing pavement. To demonstrate the measurement capability of the optical fiber sensors, six 183 cm by 183 cm by 7.5 cm (6 ft by 6 ft by 3 in) concrete panels reinforced with engineered alloy polymer macro-synthetic fibers (Febermesh 650) were fabricated in the laboratory; another three panels were cast in the pavement test field in Minnesota.

As illustrated in Fig. 4.1, a porous fabric sheet (3 mm thick) was first laid on the laboratory floor. In field applications, the fabric sheet was used to provide a water passage and a stress release mechanism between the existing pavement and the new concrete panels. Optical fibers were then deployed and attached on top of the fabric sheet with adhesives. To protect the optical fibers, a thin mortar layer (5 – 10 mm thick) was applied on top of the optical fibers. Once set for about 2 hours, the mortar was covered with concrete. The proposed installation method took advantage of the porous fabric sheet since the mortar encapsulated the fragile optical fiber and flew into the voids of the fabric forming a strong bond.
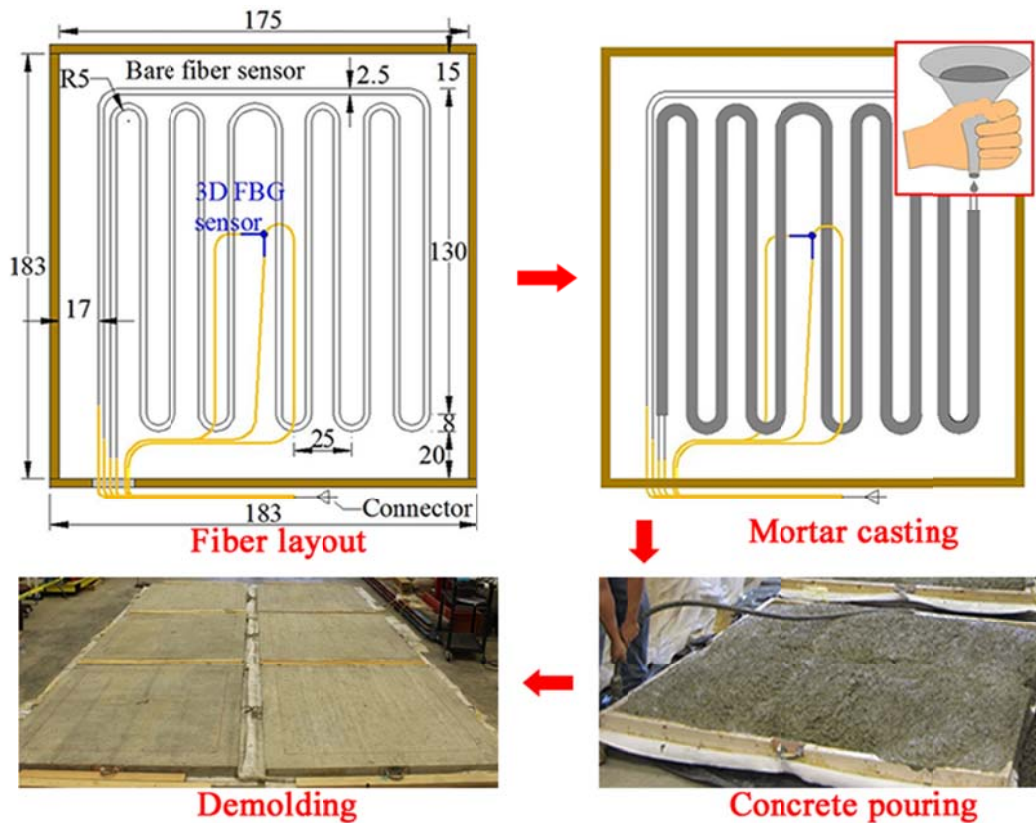
Fig. 4.1. The installation procedure of optical fibers.

4.1 Preparation of optical fibers

Each optical fiber sensor consists of at least five parts: two end connectors, one center sensor, and two transmission cables between the connectors and the sensor. In some cases, multiple fiber sensors are spliced together and then connected directly or connected by transmission cables. In other cases, the transmission cables can be eliminated when optical fibers are packaged with tight buffer and protected from damage. The three cases are illustrated in Fig. 4.2.
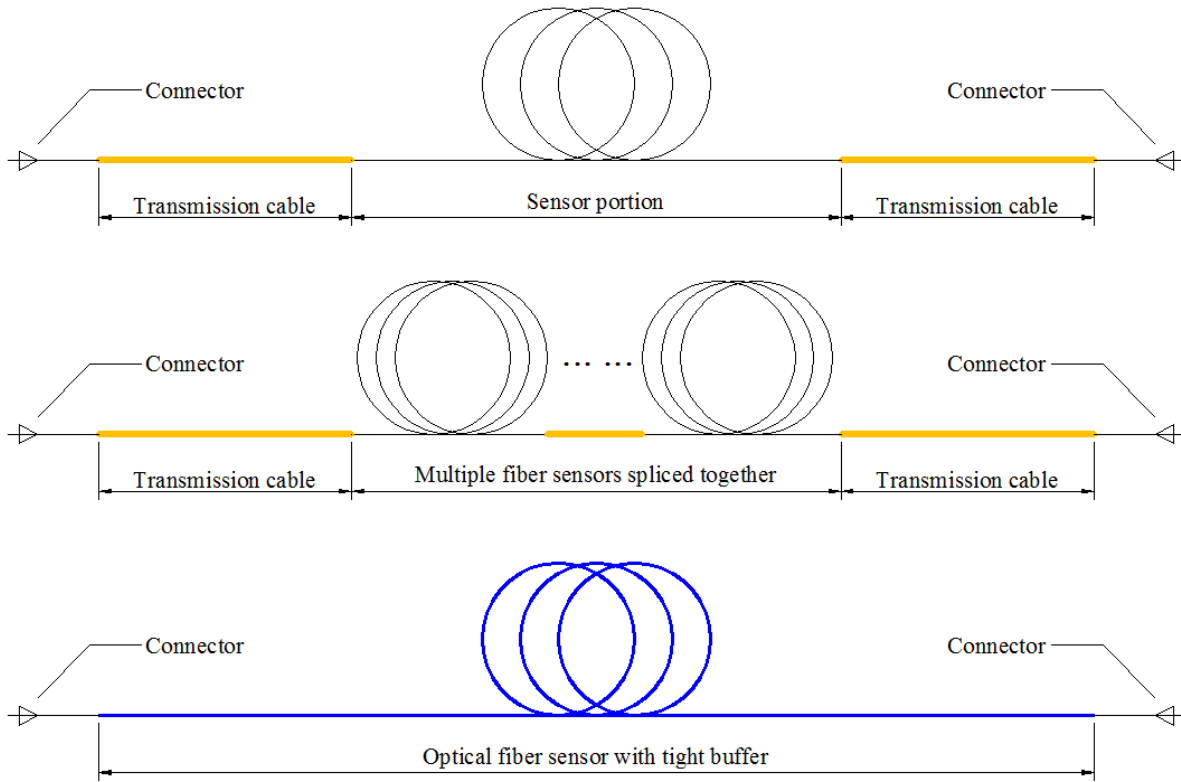
Fig. 4.2. Typical components of optical fiber sensors.

The optical fibers were cut with Precision Cleaver and spliced using the Optical Fiber Fusion Splicer. The splice loss was controlled within 0.02 dB. The fusion splice operation is shown in Fig. 4.3. When the coating was removed, the optical fiber sensor became fragile and easy to damage. To secure the fiber sensor, protection sleeves are utilized to cover the splice zone.

Fig. 4.3. The fusion splicer.

4.2 Formworks

Wood formworks were fabricated with a fabric sheet tightly stretched around their borders as shown in Fig. 4.4. A steel holder was laid at each side of the panel and reinforced by a steel grid so that the panel can be lifted conveniently.
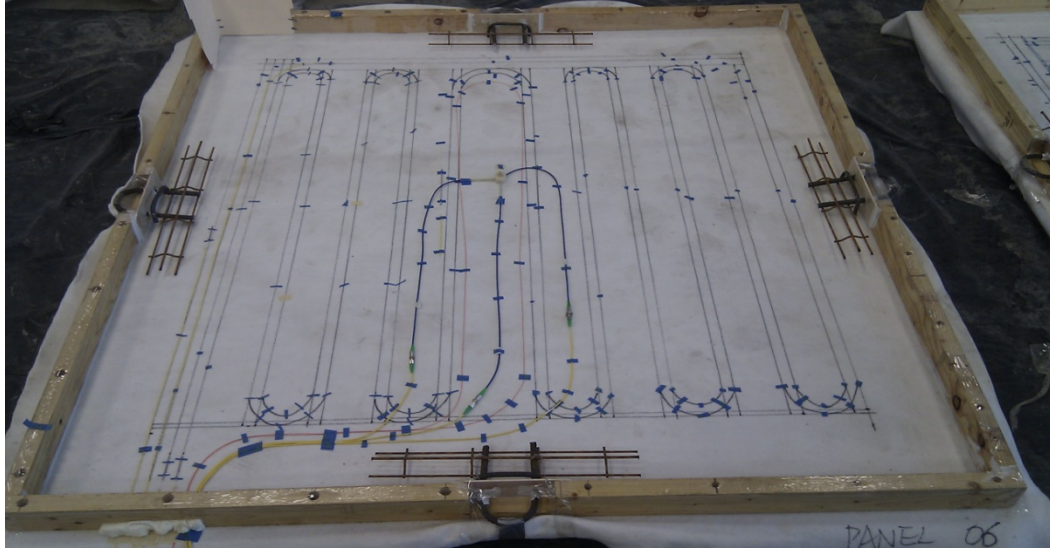
Fig. 4.4. Formwork of the pavement panel.

4.3 Installation of optical fibers

The distributed optical fiber sensors and FBG sensors were attached on top of the fabric sheet with adhesives as shown in Figs. 4.4 and 4.5. Two bare SMF-28e$^+$ fibers (BF01 and BF13) and one SMF-28e$^+$ fiber with a tight buffer (TB1) were installed in Panel 01 (P1). Two bare SMF-28e$^+$ fibers (BF07 and BF08), one SMF-28e$^+$ fiber with a tight buffer (TB1), and one 1D FBG sensor (1D-FBG-2) was installed in Panel 02 (P2). Two bare SMF-28e$^+$ fibers (BF06 and BF09) and one 3D FBG sensor (3D-FBG-1) were in Panel 03 (P3). Two bare SMF-28e$^+$ fibers (BF03 and BF15), one FN-SIL-1 concrete crack cable (CC4), and one 1D FBG sensor (1D-FBG-1) were in Panel 04 (P4). Two bare SMF-28e$^+$ fibers (BF04 and BF16) and one FN-SIL-1 concrete crack cable (CC5) were in Panel 05 (P5). Two bare SMF-28e$^+$ fibers (BF05 and BF18), one SMF-28e$^+$ fiber with a tight buffer (TB3) and one 3D FBG sensor (3D-FBG-2) were in Panel 06 (P6).
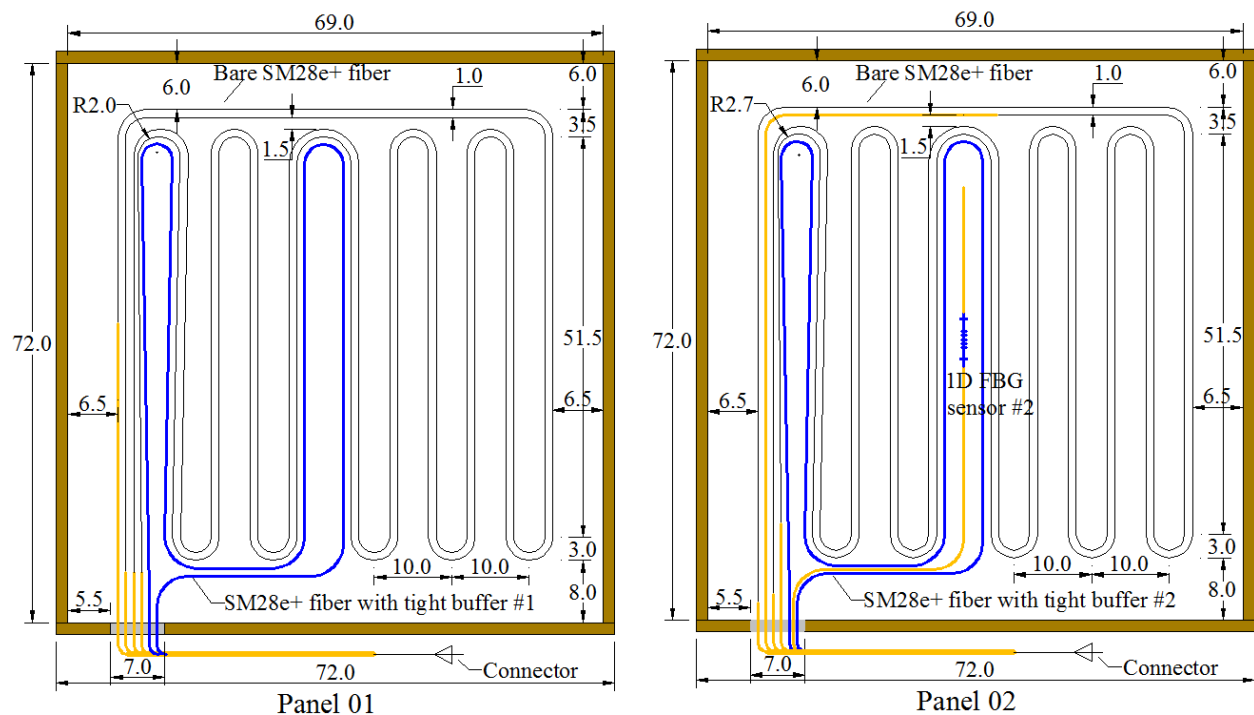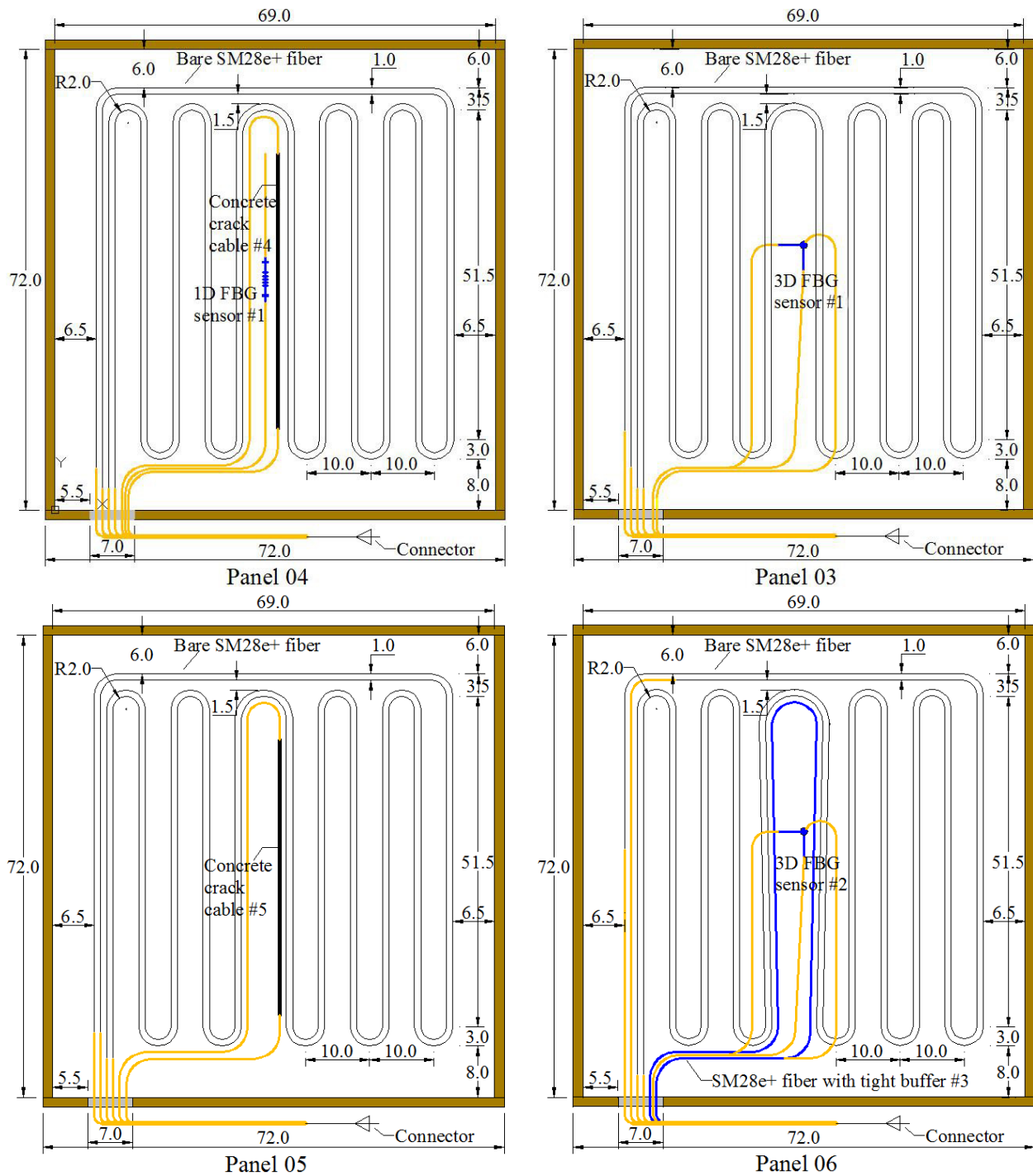
Fig. 4.5. Layout of fiber sensors in six panels (in inch = 2.54 cm).

In Fig. 4.5, the black thin line symbolizes the bare SMF-28e$^+$ fiber, the blue line represents the SMF-28e$^+$ fiber with a tight buffer, the yellow line represents the transmission cable, the black thick line represents the FN-SIL-1 concrete crack cable that includes one SMF with a white tight buffer for strain transfer and one SMF with a green loose buffer for temperature compensation. The fiber with the white tight buffer senses both strain and temperature while the fiber with the green loose buffer senses temperature only for temperature compensation in strain measurement. The installed fiber sensors in each panel are summarized in Table 4.1. Once again, "BF" means the bare SMF-28e$^+$ fiber, "TB" is for SMF-

31

28e[+] fiber with tight buffer; and "CC" is for FN-SIL-1 concrete crack cable.

Table 4.1. Installed fiber sensors in each panel

Pour number	Panel name	Bare SMF-28e^{+} fiber	SMF-28e[+] fiber with tight buffer	FN-SIL-1 concrete crack cable	1D FBG sensor	3D FBG sensor
First pour	Panel 01 (P1)	BF01 BF13	TB1	-	-	-
	Panel 04 (P4)	BF03 BF15	-	CC4W* CC4G*	1D-FBG-1	-
	Panel 05 (P5)	BF04 BF16	-	CC5W* CC5G*	-	-
Second pour	Panel 02 (P2)	BF07 BF08	TB2	-	1D-FBG-2	-
	Panel 03 (P3)	BF06 BF09	-	-	-	3D-FBG-1
	Panel 06 (P6)	BF05 BF18	TB3	-	-	3D-FBG-2

* Each FN-SIL-1 concrete cack cable consists of two optical fibers and one lead cable wrapped inside a protective tight sheath. The fiber with a white tight buffer senses both strain and temperature changes. The fiber with a green loose buffer only senses temperature change. CC4W and CC4G are referred to the fibers with white and green buffers in No. 4 FN-SIL-1 concrete crack cable, respectively. Similarly, CC5W and CC5G are for the corresponding fibers in No. 5 FN-SIL-1 concrete crack cable.

4.4 Pouring concrete

The concrete used in this study was purchased from Rolla Ready Mix in accordance with the mix design provided by Minnesota Department of Transportation (MnDOT) as specified in Table 4.2. Fibermesh 650 fibers were uniformly mixed into concrete as secondary reinforcement. Local aggregates were used according to the sizes and properties specified in Table 4.3.

Table 4.2 The proposed mixture design

MnDOT mix number	MR3A21-2F	
Water	228	
Cement	420	70%
Fly Ash	180	30%
Total Cementitious	600	Agg. Proportions
W/CM Ratio	0.38	100%
Sand	1235	41%
Coarse Aggregate #67	1790	59%
% Air Content	7.0	
Slump Range	1"-4"	
Admix #1 Dos Range	-	
Admix #2 Dos Range	0-5	oz/100# CM
Admix #3 Dos Range	0-12	oz/100# CM
Admix #4 Dos Range	0-6	oz/100# CM
Volume (27.00cf ± 0.10cf)	27.20	
Theoretical Unit Wt. (lb/cf)	142.6	

Table 4.3. The proposed materials

Aggregates					
	Pit No.	Pit Name	Size	Absorption	Gravity
Coarse Aggregate	71041	Elk River	#67	0.013	2.69
Sand	71041	Elk River	Sand	0.009	2.63
Cementitious and Admixtures					
	Manufacturer/Supplier		Admix Name	Class	Gravity
Cement	Holcim-St. Genevieve		STGBLMO	I/II	3.15
Fly Ash	Headwaters-Coal Creek		COVUNND	C/F	2.50
Admix #1	Sika AE260		-	AEA	-
Admix #2	SikaPlastocrete 161		SIPC161	A	-
Admix #3	SikaSikament 686		SIKA686	A	-
Admix #4	SikaViscocrete 2100		SIVIS2100	F	-

When concrete was poured on the fabric sheet to which the optical fibers are adhered, the fragile optical fibers were easy to damage. To prevent potential damage, the optical fibers were covered by a thin layer of mortar (5 - 10 mm thick) that was set for about 30 minutes before concrete was poured on top of the mortar. This installation method took advantage of the porous fabric for good sensor-concrete bonding because the mortar encapsulated the fragile optical fiber and flew between the fibers of the fabric, forming a strong bond as illustrated in Fig. 4.6. The SEM image in Fig. 4.7 verified the good sensor-concrete interface.
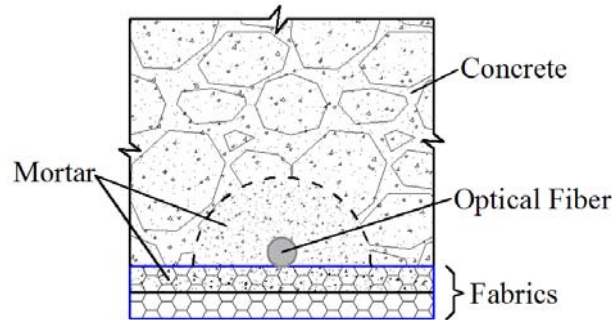
Fig. 4.6. Schematic diagram of an optical fiber covered with mortar and surrounded by mortar.
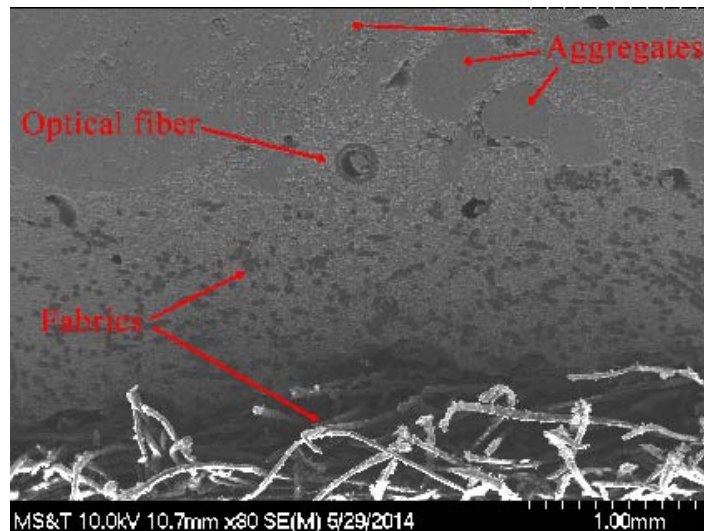
Fig. 4.7. SEM image of an optical fiber embedded in mortar.

33

The six panels were cast in two pours. Panels P1, P4, and P5 constituted the first pour while Panels P2, P3, and P6 were done in the second pour. After concrete pouring, measurements were immediately taken from optical fibers to ensure that they were functional. As indicated in Table 4.4, BF01 in Panel P1, BF15 in Panel P4, and BF04 and BF16 in Panel P5 lost the optical fiber loop during the first concrete pour. Losing the loop of an optical fiber means that the light signal cannot pass through the optical fiber mainly due to either local damage or severe macro-bending of the fiber as a result of fiber displacement. The other fiber sensors survived the first concrete pouring. All fibers installed during the second pour successfully survived the casting process. For the first three panels, concrete was poured 30 minutes after mortar casting so that the mortar was not hard enough to protect the fibers during concrete pouring. Therefore, for the second three panels, concrete was poured after mortar was cast and set for 2 hours, and became strong enough to protect the optical fibers. The fact that all the fiber sensors installed during the second pour survived proved the effectiveness of the proposed installation method.

4.5 Summary

An optical fiber sensor installation method applicable in both laboratory and field conditions is proposed to address the logistics of handling fragile optical fibers. The proposed installation method took advantage of the porosity of the fabric sheet so that, during casting, mortar can flow around the optical fiber and seep in the voids of the fabric, forming a strong bond between the optical fiber and mortar. When set for 2 hours, mortar around optical fiber sensors can effectively protect the sensors from damage during concrete pouring. Tests immediately after concrete pouring verified the 100% success rate and indicated the effectiveness of the proposed installation method.

Table 4.4. Survival rate of installed fiber sensors after concrete pouring

Pouring number	Panel name	Bare SMF-28e$^+$ fiber	FN-SIL-1 concrete crack cable	SMF-28e$^+$ fiber with tight buffer	1D FBG sensor	3D FBG sensor
First pouring	Panel 01 (P1)	BF13	-	TB1	-	-
	Panel 04 (P4)	BF03	CC4W CC4G	-	1D-FBG-1	-
	Panel 05 (P5)	-	CC5G	-	-	-
Second pouring	Panel 02 (P2)	BF07 BF08	-	TB2	1D-FBG-2	-
	Panel 03 (P3)	BF06 BF09	-	-	-	3D-FBG-1
	Panel 06 (P6)	BF05 BF18	-	TB3	-	3D-FBG-2

Chapter 5 Static truck load tests in laboratory

5.1 Load matrix

Each panel was loaded by an empty or fully loaded dump truck as shown in Fig. 5.1. Brillouin frequency shifts were directly measured in each panel by using the Neubrescope and converted to their corresponding strains based on the calibration frequency shift to strain sensitivity coefficient as discussed in Chapter 3. The configuration and size of the dump truck are shown in Fig. 5.2. The contact areas of tires were highlighted in Fig. 5.2 and measured when the inflation pressure of the tires was 90 psi and the truck was empty. Along the truck direction, the contact length of a tire decreases with the inflation pressure in the tire and increases with the weight on the tire. The contact width of the tire doesn't change significantly because the lateral stiffness of the tire is substantially larger than the longitudinal stiffness.

Fig. 5.1. Dump truck used to load concrete panels.
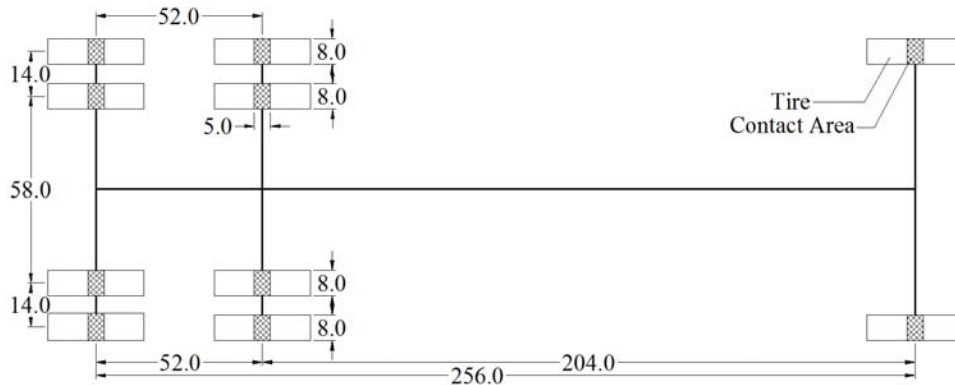
Fig. 5.2. Configuration and size of the dump truck (in inch = 2.54 cm).

The layout of optical fibers in the six concrete panels is re-produced and presented in Fig. 5.3. The six panels instrumented with optical fiber sensors were laid down on the strong floor in the Highbay Laboratory and loaded by the truck applied as shown in Fig. 5.4. Each panel was loaded by an empty truck and a fully loaded truck. While the truck was in position, optical fibers were connected to the data acquisition systems, providing strain and temperature measurements.
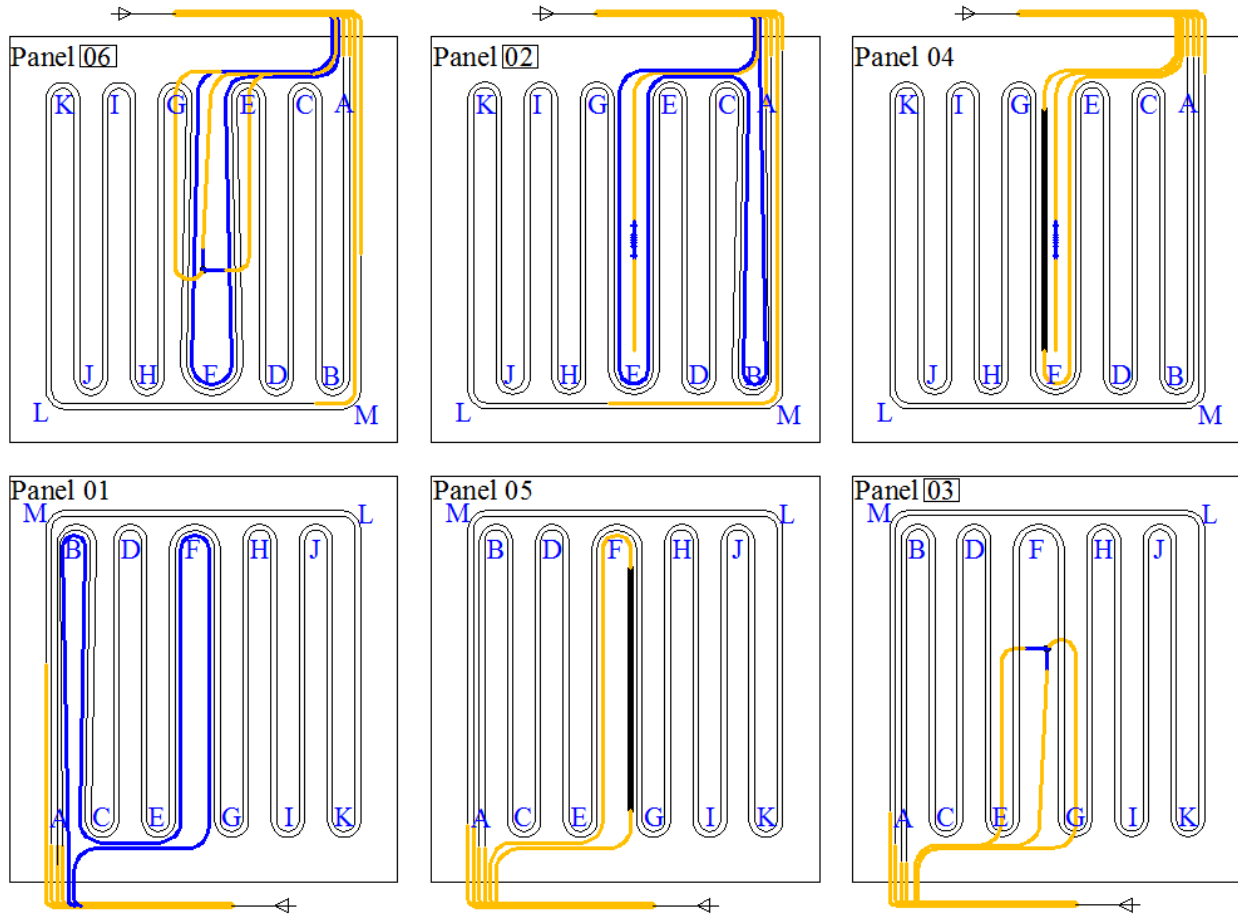
Fig. 5.3. Layout of optical fibers and six concrete overlays.

Fig. 5.4. Concrete panels under truck loads.

The truck load matrix is presented in Table 5.1. The overall test plan consisted of three phases. In the first phase, the six concrete panels were loaded by the empty truck with two passes along the side and middle portions. Each pass included three stops. For the side pass as displayed in Fig. 5.4, truck tires pressed at the edges of the panels. For the middle pass, the truck went along the center lines of the panels. In the second phase, the truck was fully loaded with stones from a local quarry, and then loaded the six panels following the same procedure as the first phase. In the last phase, 1/8-in vertical faulting in field applications was simulated by placing a piece of hard plywood underneath one side of each panel.

36

Table 5.1. Truck load matrix

Truck pass	Under the empty truck	Under the fully loaded truck	
		No faulting/dislocation	1/8 in. faulting/vertical dislocation
Side Pass (Pass I)	Pass I-Stop 1 (P1S1) Pass I-Stop 2 (P1S2) Pass I-Stop 3 (P1S3)	Pass I-Stop 1 (P1S1) Pass I-Stop 2 (P1S2) Pass I-Stop 3 (P1S3)	Substrate movement
Middle Pass (Pass II)	Pass II-Stop1 (P2S1) Pass II-Stop 2 (P2S2) Pass II-Stop 3 (P2S3)	Pass II-Stop1 (P2S1) Pass II-Stop 2 (P2S2) Pass II-Stop 3 (P2S3)	None

Table 4.4 summarizes the optical fiber surviving rate immediately after concrete pouring when the concrete panels were laid flat on the strong floor in the Highbay Laboratory as shown in Fig. 4.1. After 28 days of curing, initial tests were conducted to collect reference strain data from the optical fiber sensors (unloaded). BF13 and 1-D FBG-01 were found to be mal-functional. The optical fiber sensors that survived by that time are listed in Table 5.2. The weight of the dump truck was measured at a local weight station and was listed in Table 5.3.

Table 5.2. Surviving fiber sensors for truck load tests

Pour number	Panel name	Bare SMF-28e$^+$ fiber	FN-SIL-1 concrete crack cable	SMF-28e$^+$ fiber with tight buffer	1D FBG sensor	3D FBG sensor
First pour	Panel 01 (P1)	-	-	TB1	-	-
	Panel 04 (P4)	BF03	CC4W CC4G	-	1D-FBG-1	-
	Panel 05 (P5)	-	-	-	-	-
Second pour	Panel 02 (P2)	BF07 BF08	-	TB2	1D-FBG-2	-
	Panel 03 (P3)	BF06 BF09	-	-	-	3D-FBG-1
	Panel 06 (P6)	BF05 BF18	-	TB3	-	3D-FBG-2

Table 5.3. Weight of the truck (in lb = 4.448 N)

	Front axle	Rear axle	Total
Empty truck	9,700	11,440	21,140
Loaded truck	13,760	31,240	45,000

5.2 Truck tests without vertical faulting

Under the empty truck without vertical faulting, cracks appeared in the panels due to unevenness of the floor in the laboratory. When placed on the uneven floor, each panel was partially supported, subjected to flexural bending at the unshored locations, and thus experienced cracking. Since the unevenness was not known, cracks appeared randomly in different parts. However, most cracks initiated from the side and propogated towards the middle of the concrete panel. Under the fully loaded truck without vertical faulting, more cracks appeared due to the unevenness of the floor. Some cracks initiated from the top and penetrated through the thickness of the panel. Other cracks initiated from the bottom of the panels. Those cracks that intersected with the optical fibers can be detected. As the cracks were widened, the optical fibers spanned over the cracks were strained in tension as reflected in the high peaks of strain distributions. The signficant extension of the cracks may also be captured by multiple optical fibers that

were crossed by. In this case, more peaks appears in multiple strain distributions taken from the optical fiber sensors.

5.2.1 First stop of side pass

The first row of rear wheels were parked on P4 and P3 as shown in Fig. 5.3. Their positions were measured from edges of the wheels and the panels. Because of the eneven floor in the laboratory, some cracks appeared under the truck load.
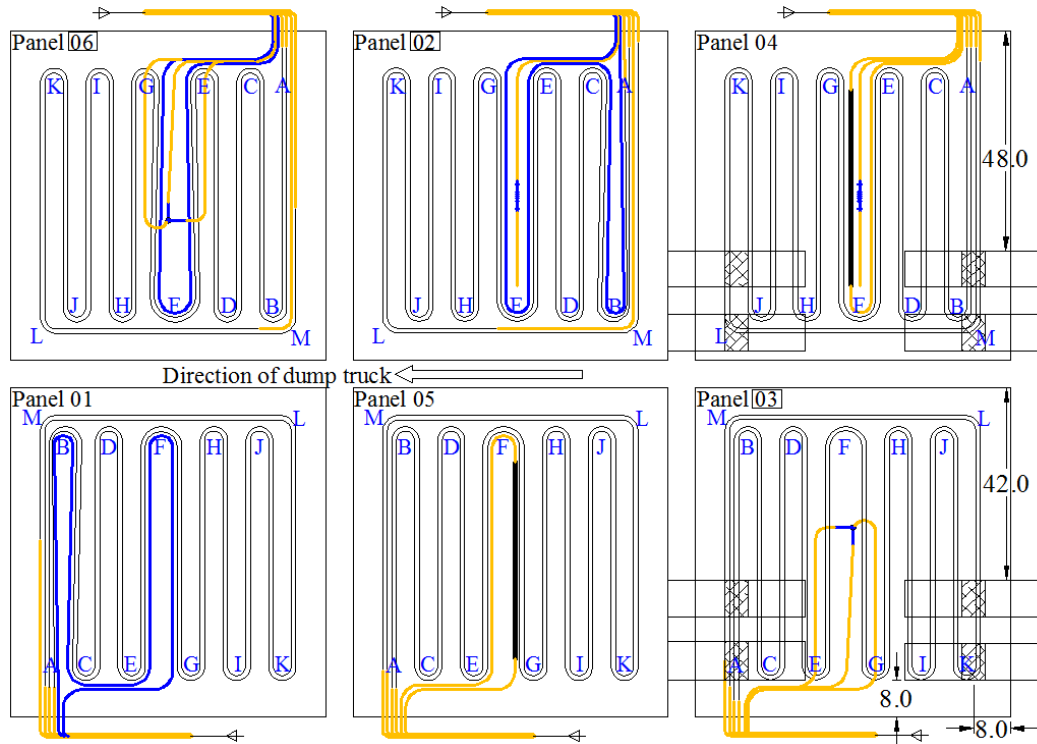
Fig. 5.3. Location of the truck load P1S1 (in inch = 2.54 cm).

(1) Panel 04

Panel P4 was instrumented with CC4W, CC4G, BF03, and BF13. However, BF13 was found malfunctional at the time of the truck load test. As shown in Fig. 5.4, four hairline cracks that were difficult to see by naked eyes were successfully detected by the distributed optical fibers. As indicated in Fig. 5.5(a), three of them (C1-1, C2-1, and C4-1) were detected by BF03 under the empty truck load and the fourth crack (C3-1) was captured under the fully loaded truck load. Since no cracks crossed the concrete crack cable CC4W, no sharp peak can be seen in the strain distributions in Fig. 5.5(b). The strain distributions between points "F" and "G" were measured by both sensors and thus compared in Fig. 5.6. It can be observed from Fig. 5.6 that the measurement results from the two sensors match well with each other. Because the two fibers were separated in P4 with a short distance as shown in Fig. 5.4, the strains measured from the two fibers cannot be exactly the same. The cracks were located at the positions of peaks in strain distributions. Their widths can be estimated from the magnitude of the sharp peaks.

38
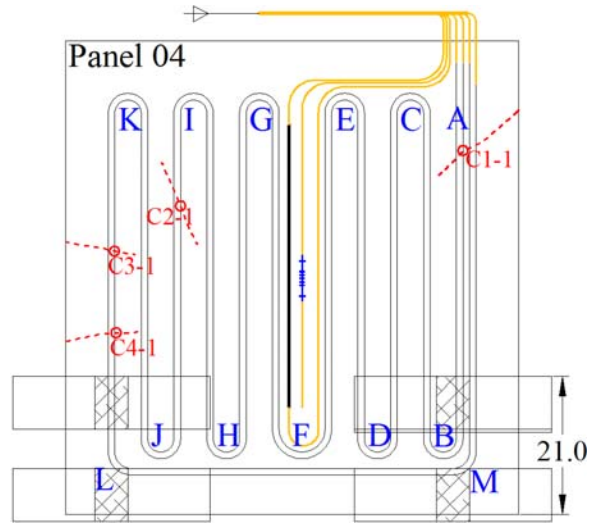
Fig. 5.4. Cracks in P4 under the truck load P1S1.

(a) BF03

(b) CC4W

Fig. 5.5. Strain distributions in P4 under the truck load P1S1.

(a) Under the empty truck load

(b) Under the fully loaded truck
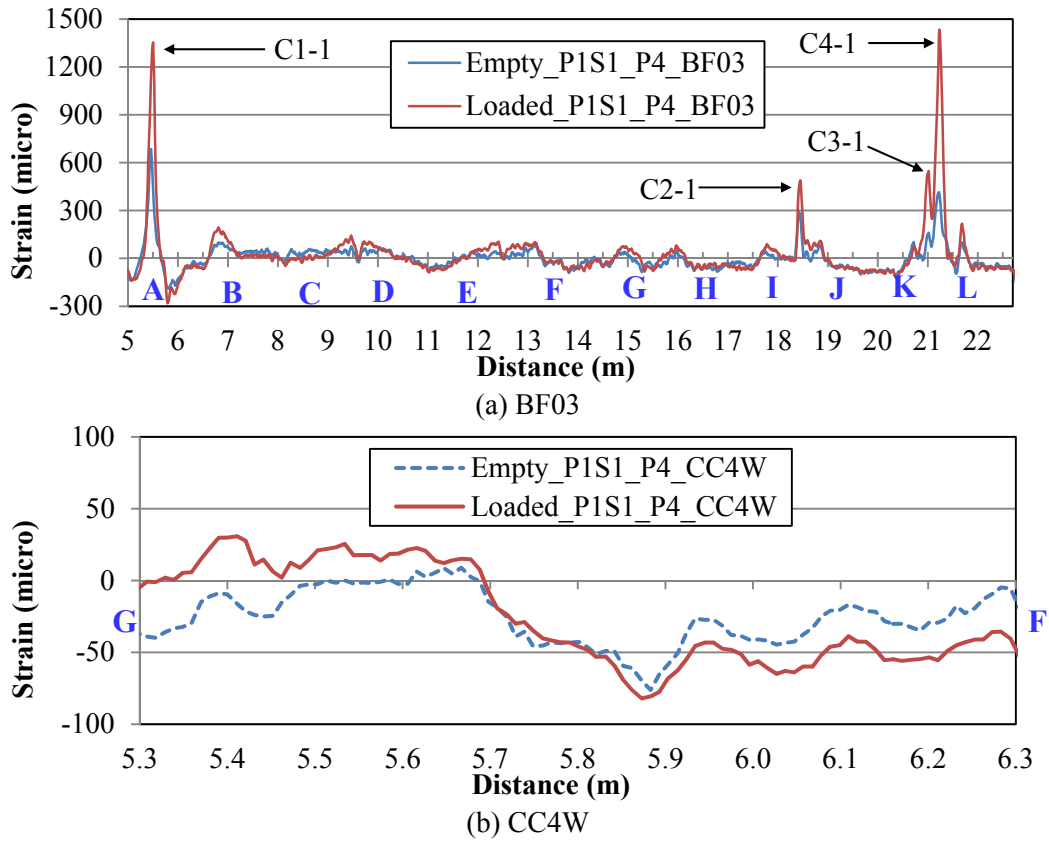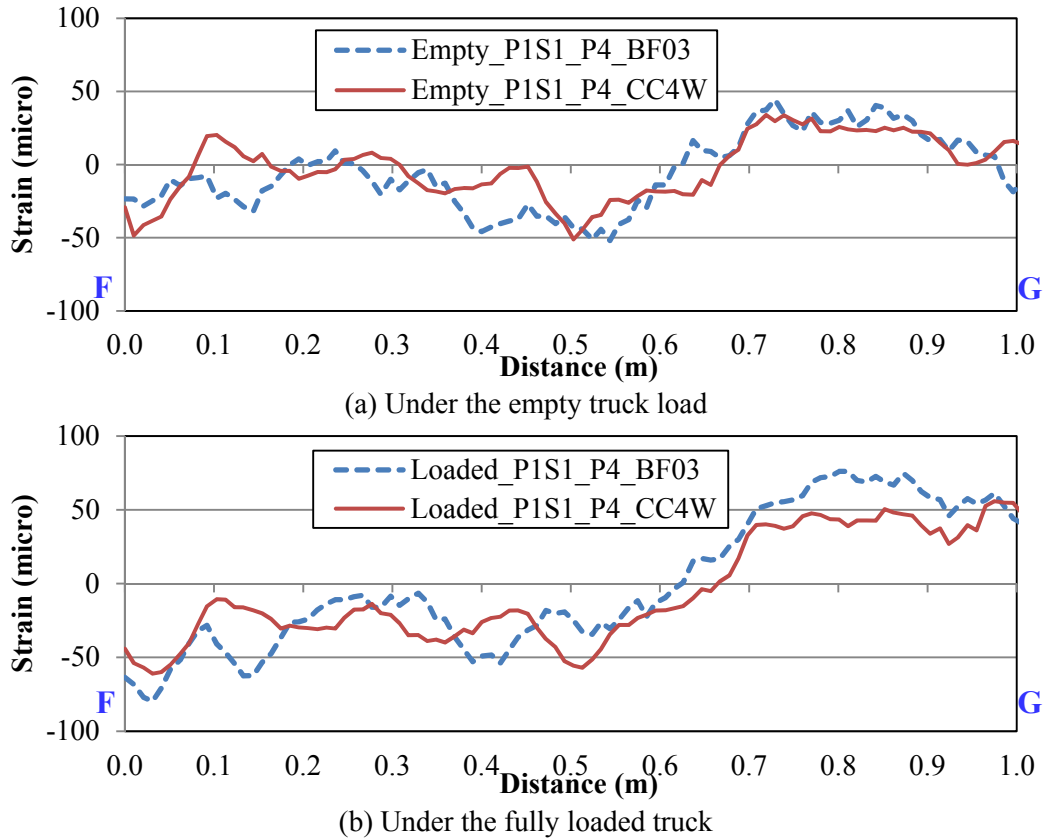
Fig. 5.6. Comparison of the strain distributions in BF03 and CC4W.

(2) Panel 03

P03 were instrumented with BF06 and BF09 that were paralleled to each other and separated by 1 in. Both fiber sensors were functional during the truck load tests. Three hairline cracks were observed in P3 as shown in Fig. 5.7. They were located at the peaks in strain distributions. Their widths corresponded to the magnitude of the sharp peaks.
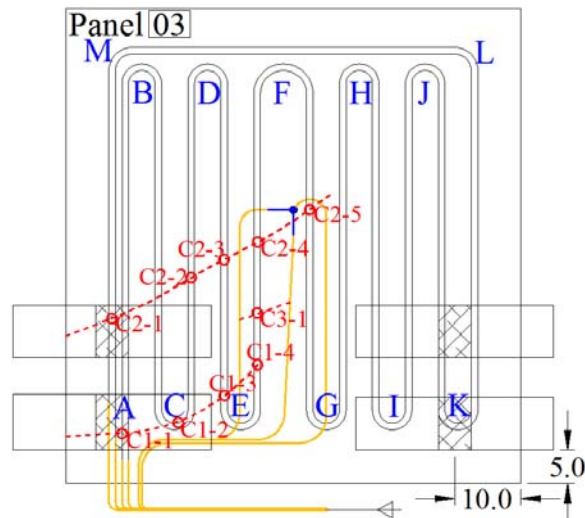
Fig. 5.7. Cracks in P3 in the truck load P1S1.

As shown in Fig. 5.8(a), no crack was detected by either BF06 or BF09 under the empty truck load. However, under the loaded truck, three cracks (C1, C2 and C3) were captured by both BF06 and BF09 as

40

shown in Fig. 5.8. Since BF06 and BF09 were closed with 1 in separation, their measurement results were compared in Fig. 5.9. It can be observed from Fig. 5.9 that the strain distributions from the two fibers were close but not exactly the same, which reflected the variation of strain distributions in the lateral direction of the fiber. For instance, as shown in Fig. 5.9(b), two cracks were detected between point A and point B by either BF06 or BF09. However, the magnitude of the first peak detected by BF06 (about 600 $\mu\varepsilon$) was 1.5 times that of the corresponding peak detected by BF09 (about 400 $\mu\varepsilon$). This was because the crack width of each crack varied along the crack and the width of crack C1-1 at BF06 was larger than that at BF09.

(a) BF06

(b) BF09
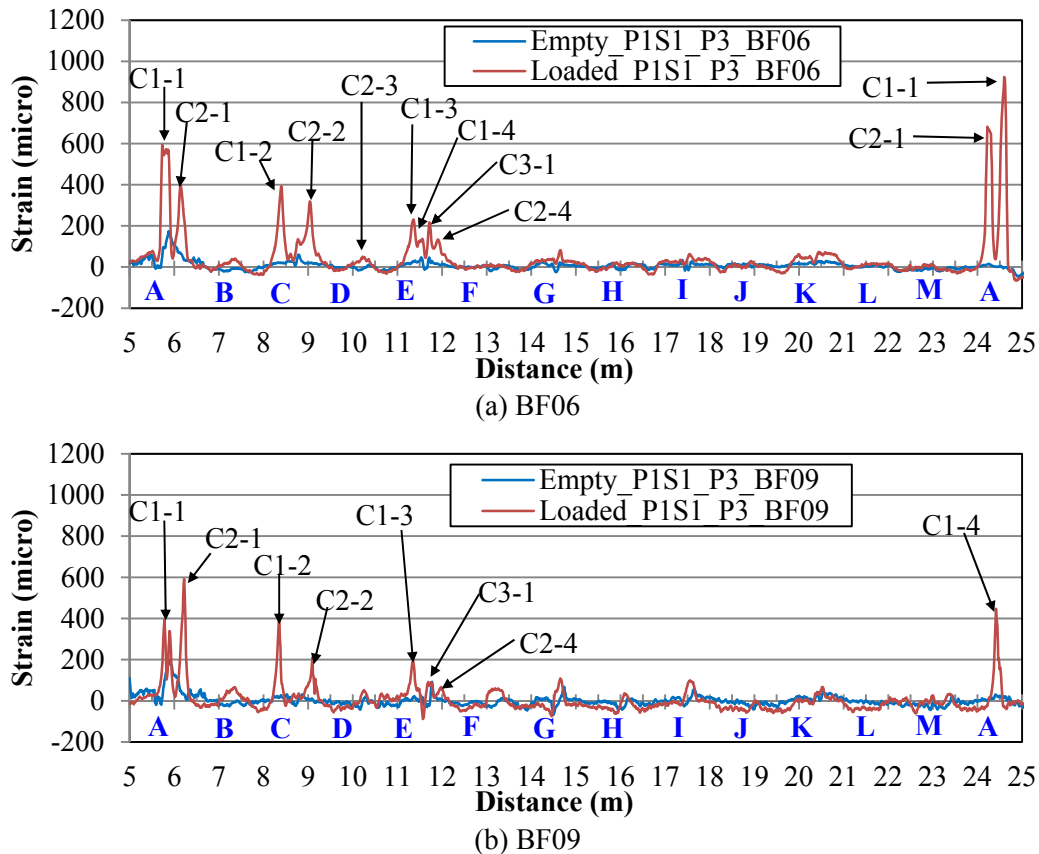
Fig. 5.8. Strain distributions in P3 in the truck load P1S1.

(a) Under the empty truck

41
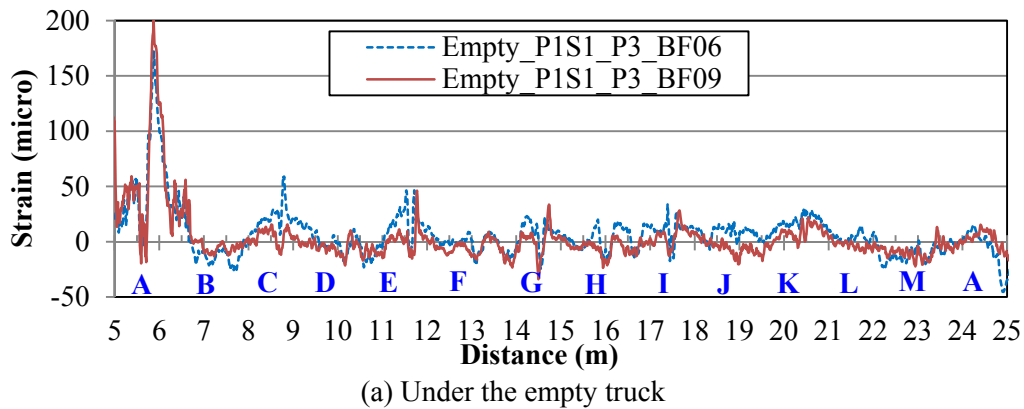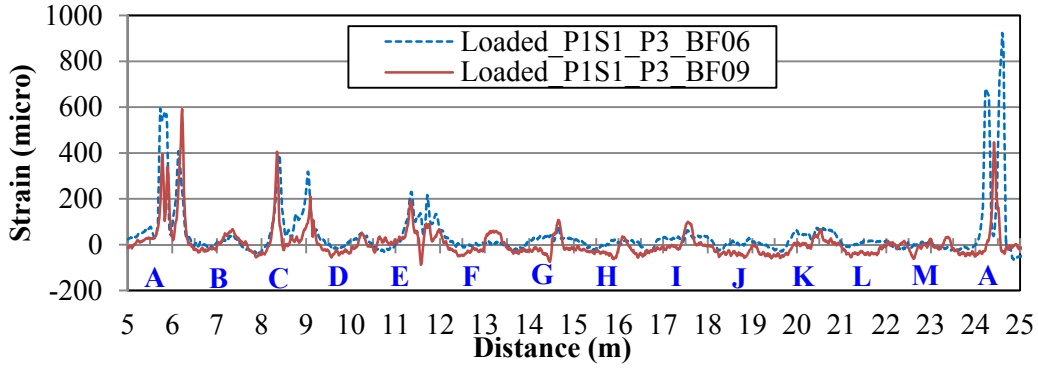
(b) Under the fully loaded truck

Fig. 5.9. Comparisons of the strain distributions in BF06 and BF09.

5.2.2 Second stop of side pass

The first row of rear wheels were parked on P2 and P5 as shown in Fig. 5.10. P2 was instrumented with BF07, BF08 and TB2. All the three fibers worked. The optical fibers in P5 were damaged during concrete pouring. Strain distributions were collected from the optical fibers in P2 by the Neubrescope.
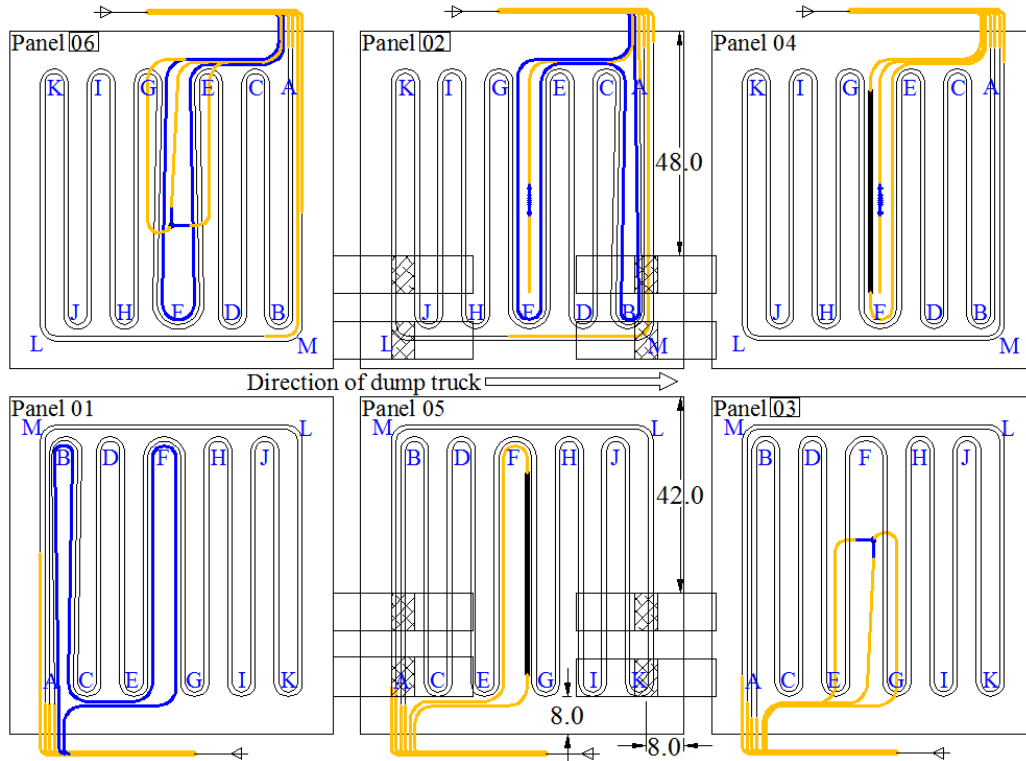
Fig. 5.10. Position of the truck load P1S2.

Due to the uneven support condition, P2 cracked as illustrated in Fig. 5.11. The cracks were detected and identified from the strain distributions. They were successfully localized.

42
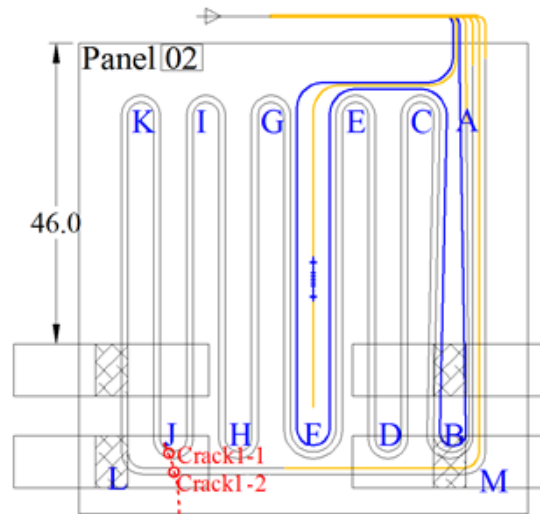
Fig. 5.11. Crack in P2 in P1S2.

Fig. 5.12 shows the strain distributions in P2 from BF07 and BF08. Under the empty truck load, there was no crack. Under the loaded truck, C1 appeared and was detected by BF07 and BF08.
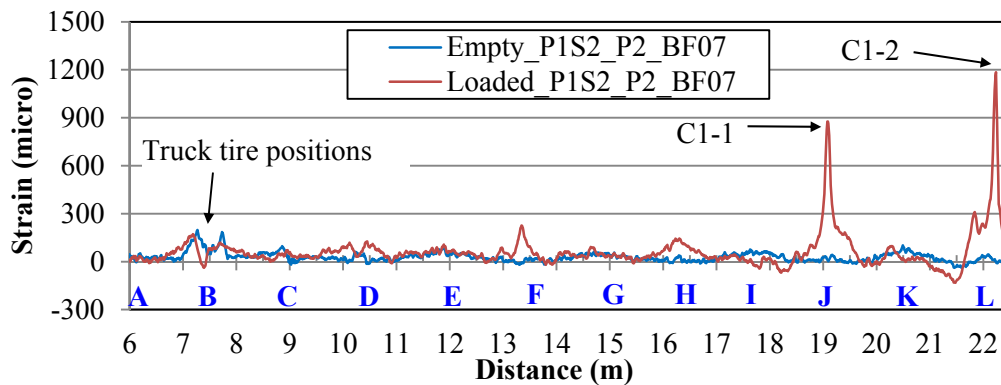
(a) BF07
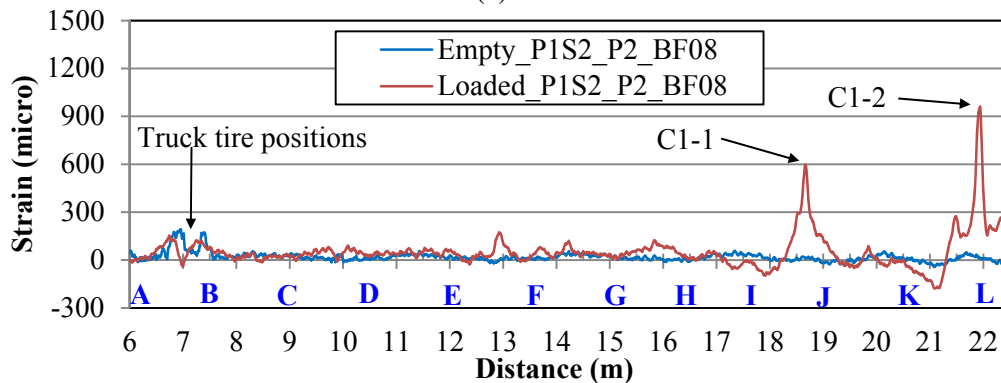
(b) BF08

Fig. 5.12. Strain distributions in P2 in P1S2.

Since BF07 and BF08 were close with 0.5 in separation, their measurement results were compared in Fig. 5.13. It can be observed from Fig. 5.13 that the strain distributions from the two fibers were similar but not exactly the same. For instance, as shown in Fig. 5.13(b) for point J, one crack was detected by either BF07 or BF08. However, the magnitudes of the two peaks were 900 με and 600 με, respectively. By comparing the peak locations under the loaded truck load in Fig. 5.12(b) with those in Fig. 5.13(b), a

distance shift in the horizontal axis direction was observed. Indeed, the strain distribution measured by BF08 must be shifted in Fig. 5.13 in order to be better compared with that measured by BF07 since the two optical fibers had different lengths and may start from different locations, which can be taken into account in data processing.

(a) Under the empty truck

(b) Under the loaded truck

Fig. 5.13. Comparison of the strain distributions in BF07 and BF08.

5.2.3 Third stop of side pass

The first row of rear wheels were parked on P1 and P6 as shown in Fig. 5.14. P1 was instrumented with BF01, BF13 and TB1. But, BF01 and BF13 damaged during the specimen fabrication. P6 was instrumented with BF05, BF18 and TB3. All three fibers were functional. Strain distributions were collected from the optical fibers in P1 and P6 by the Neubrescope.

Fig. 5.14. Position of the truck load P1S3.

(1) Panel 01

Fig. 5.15 shows the location of two cracks in P01. Fig. 5.16 shows the strain distributions in P1. No crack detected under the empty truck loading. Two cracks appeared and were detected by the fiber under the fully loaded truck. The cracks were located at the positions of peaks in strain distributions. In Fig. 5.16, the three peaks represented the three intersection points of the optical fiber TB1 and the cracks shown in Fig. 5.15.
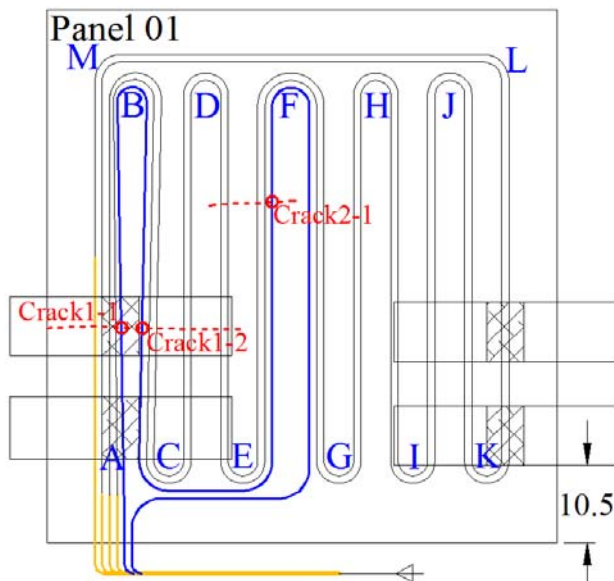
Fig. 5.15. Cracks in P1 under the truck load P1S3.

45
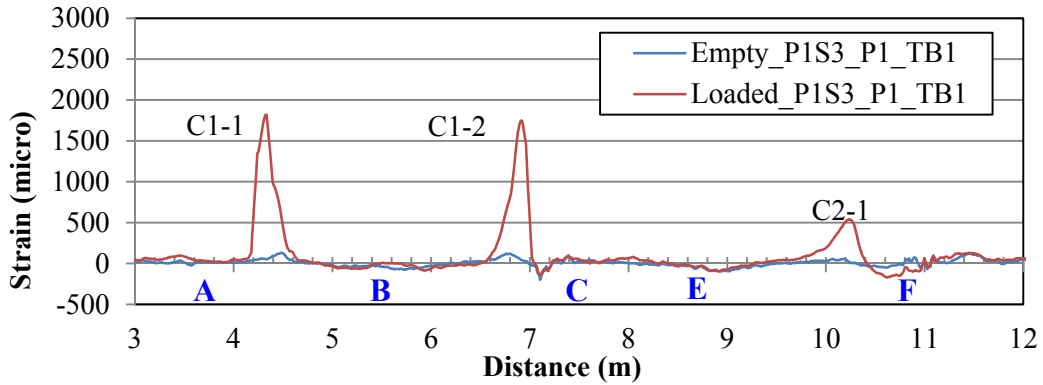
Fig. 5.16. Strain distributions in P1 under the truck load P1S3.

(2) Panel 06

P6 was relatively evenly supported on the floor compared with other panels. No crack was observed in Fig. 5.17 under the same truck load as the other panels. As shown in Fig. 5.18, the peaks between point 'J' and 'K' well reflected the strain distributions due to the tire pressure while the ones between point 'L' and 'M' were not so corresponding due to the uneven floor. In addition, the measurement results from BF18 and TB3 were compared in Fig. 5.19. It can be observed from Fig. 5.19 that the bare fiber can provide strain distributions with higher spatial resolution than the fiber with tight buffer.
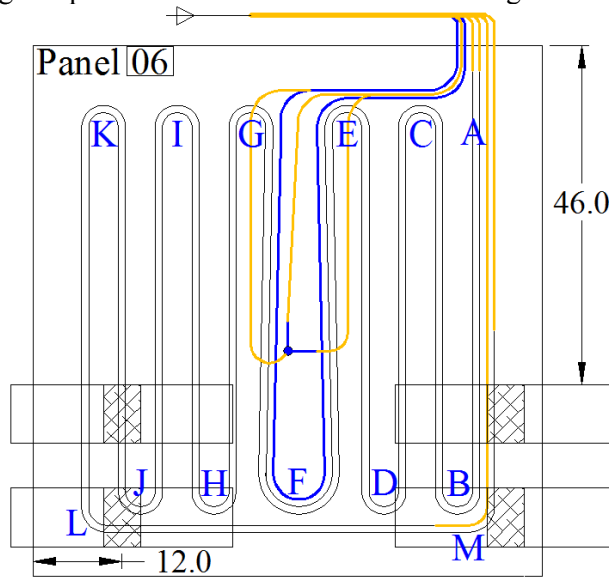
Fig. 5.17. Position in P6 of the truck load P1S3.

(a) BF05

46

(b) BF07
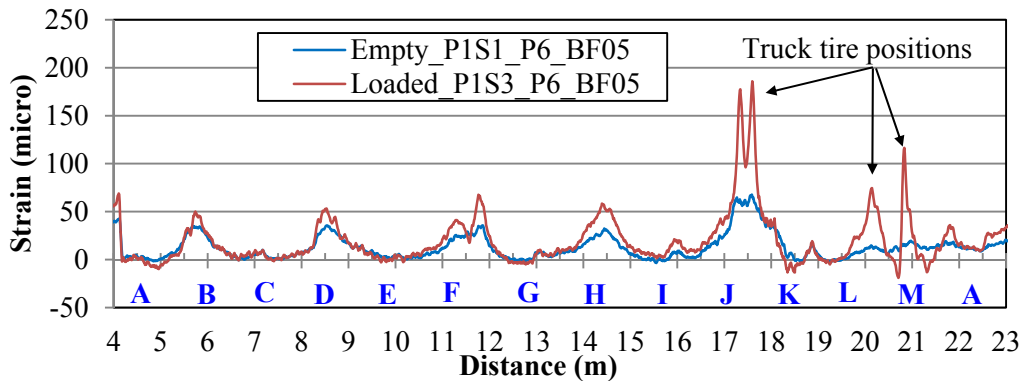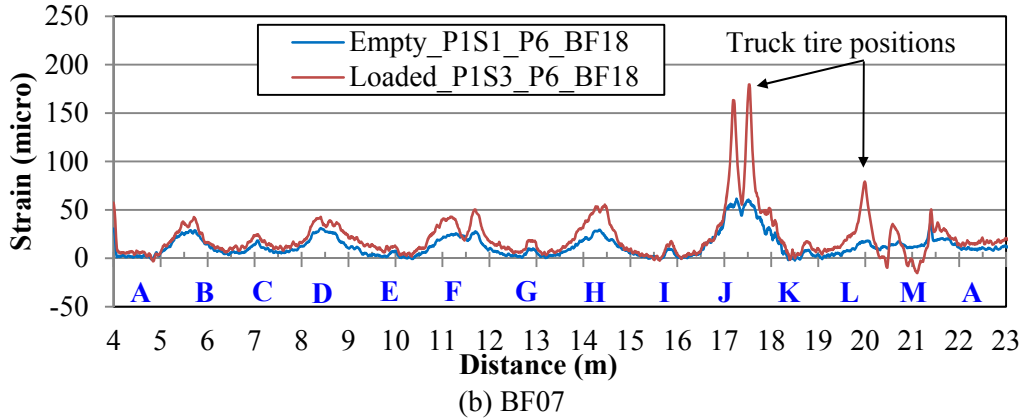
Fig. 5.18. Strain distributions in P6 in P1S3.

As shown in Fig. 5.19, the measurements from BF18 and TB3 are in good agreement. However, their spatial resolutions are different. For the same peak at point 'J' in Fig. 5.19, the width measured by BF18 (about 0.1 m) was much smaller than that by TB3 (0.25 m). Since the two optical fibers were spaced with 0.5 in distance, the strain distributions at each fiber's location were expected to be close to each other. The reason is that the required lengths to transfer strain from the concrete panel to glass core were different for the two types of fibers. The thickness of the buffer on TB3 was about 320 μm while the coating was about 60 μm. The total thickness outside the glass cladding was 380 μm for TB3 in comparison with only 60 μm for BF18. Therefore, TB3 needed a longer length than BF18 to transfer the same amount of strain.
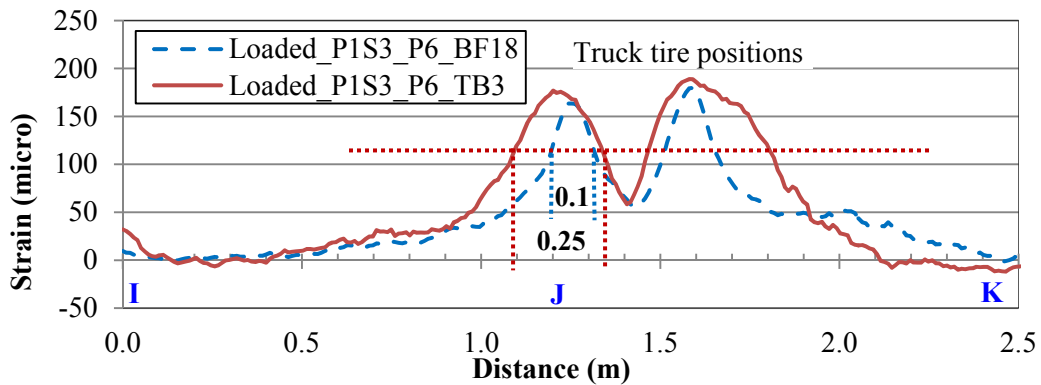
Fig. 5.19. Comparison of the strain distributions in BF07 and BF08.

BF18 and BF05 were also close to each other with 0.5 in. distance. As compared in Fig. 5.20, the strain distributions from BF18 and BF05 were very close, verifying the accuracy of the measurements.
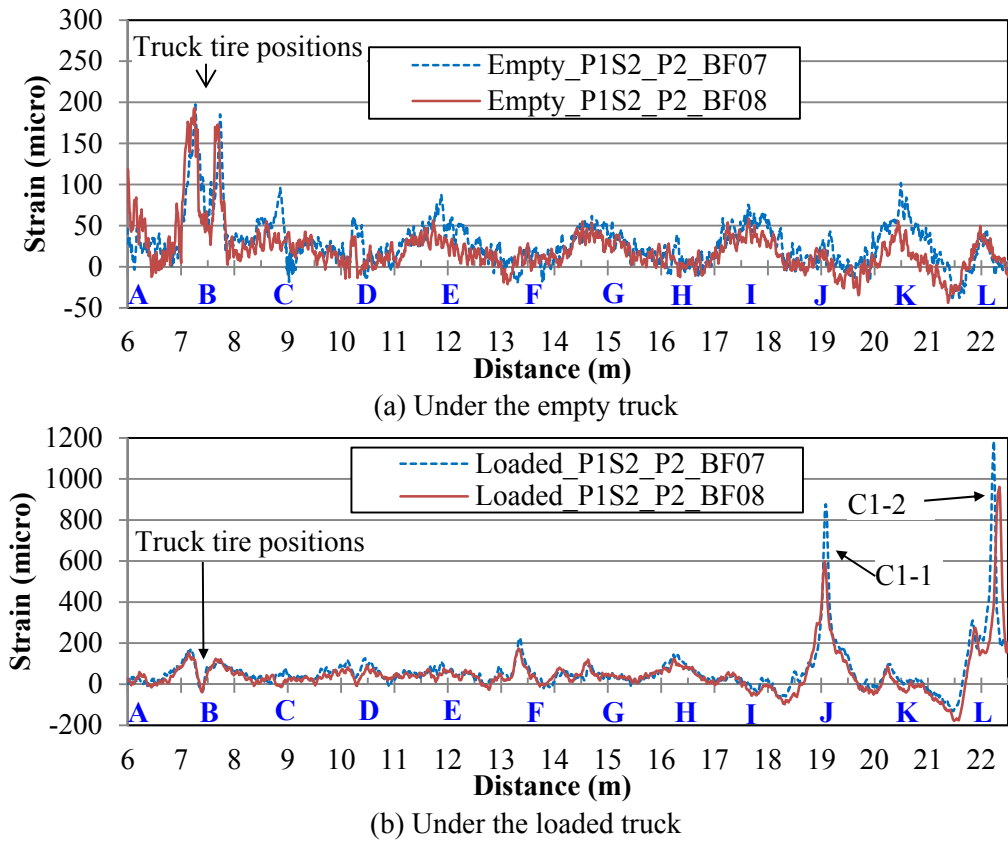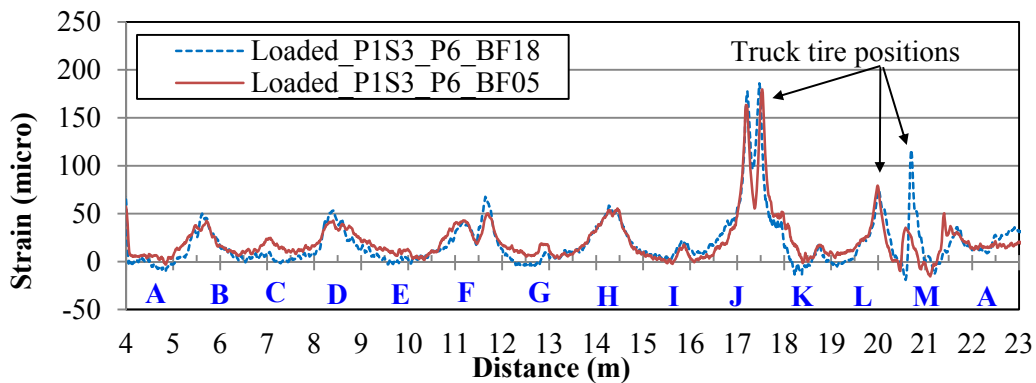

Fig. 5.20. Comparison of the strain distributions in BF07 and BF08.

47

5.2.4 First stop of middle pass

The first row of rear wheels were parked on P3 and P4 as shown in Fig. 5.21. P3 was instrumented with BF06 and BF09. Both fibers worked as expected. P4 was instrumented with CC4W, CC4G and BF03. All the fibers were functional as well. Strain distributions were collected from the optical fibers in P3 and P4 by the Neubrescope. Compared with the P1S1, more cracks appeared in this case.
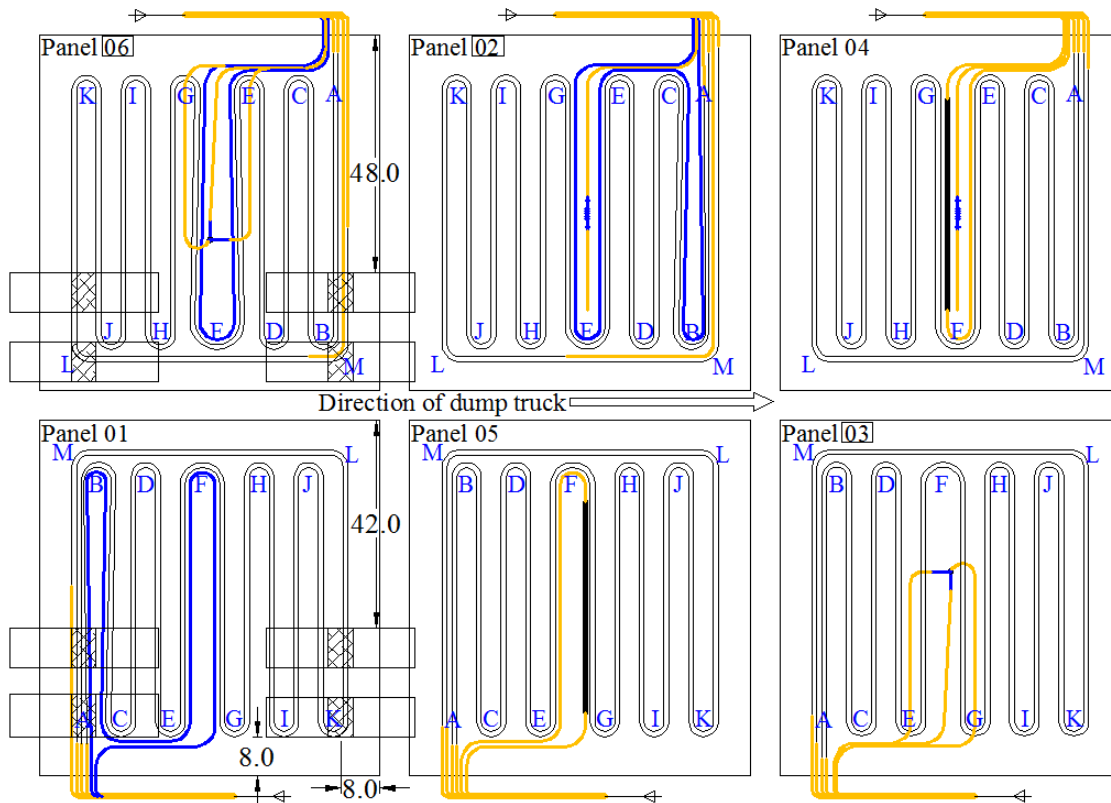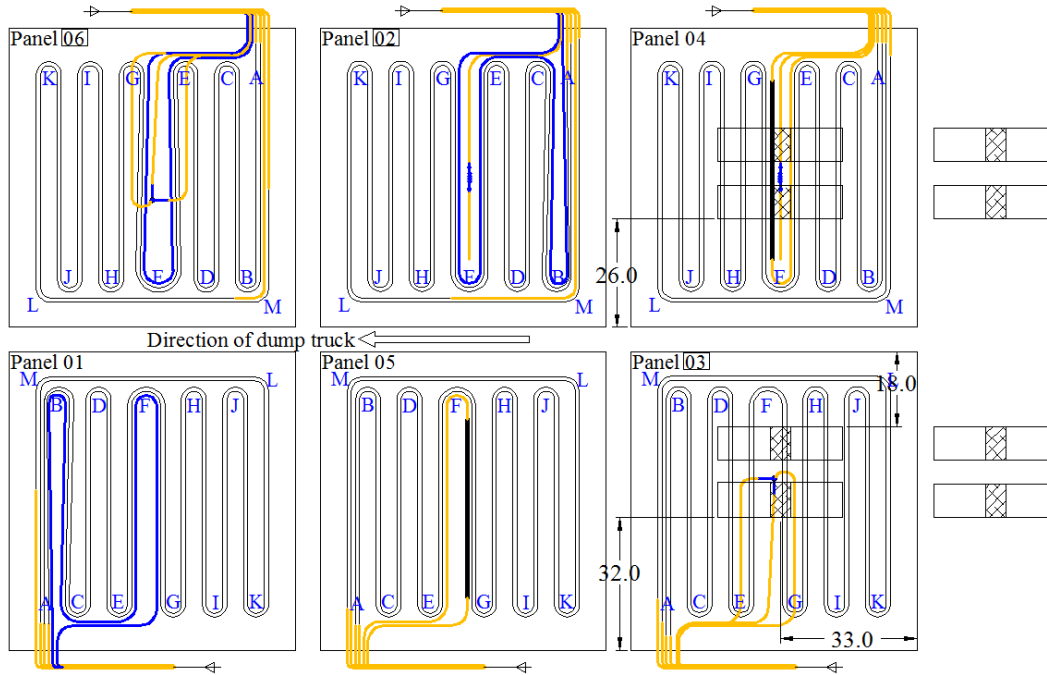

Fig. 5.21. Position of the truck load P2S1.

(1) Panel 04

Due to the uneven support condition, P4 cracked under the loaded truck as illustrated in Fig. 5.22. The cracks were detected and identified from the strain distributions. They were successfully localized in Fig.5.23. Since BF03 and CC4W were close, their measurements were compared in Fig. 5.24. Overall, the measurements were in good agreement. But the spatial resolutions were not the same. The bare fiber provided much better spatial resolution than the packaged concrete crack cable.
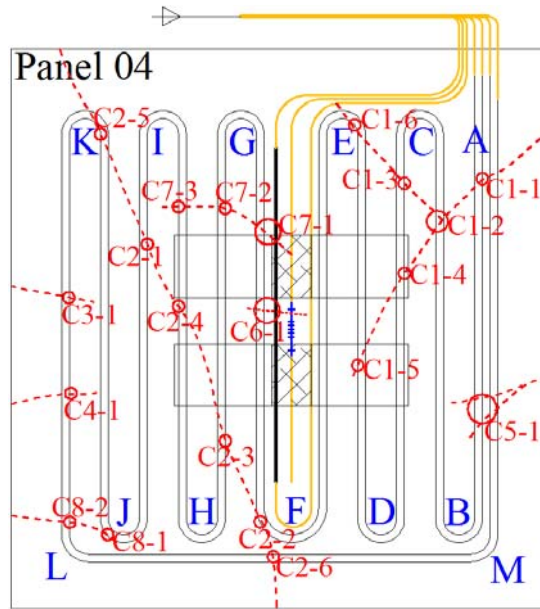
Fig. 5.22. Cracks in P4 under the truck load P2S1.

(a) BF03

(b) CC4W
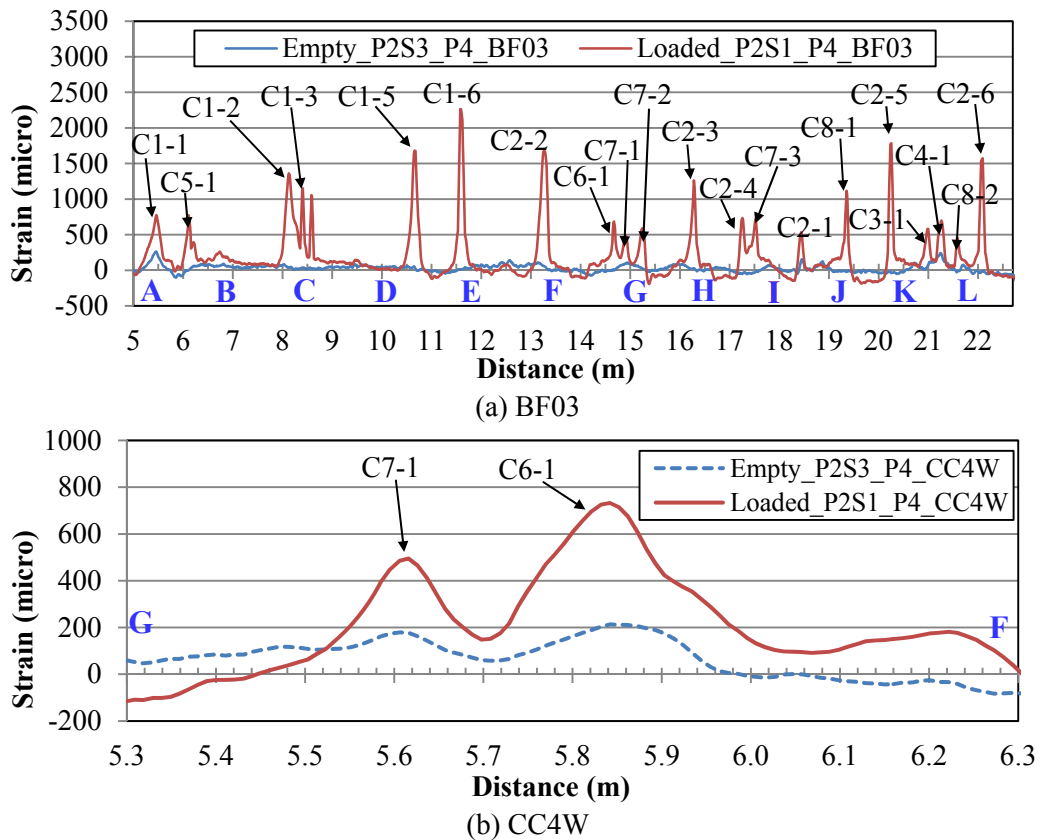
Fig. 5.23. Strain distributions in P4 under the truck load P2S1.
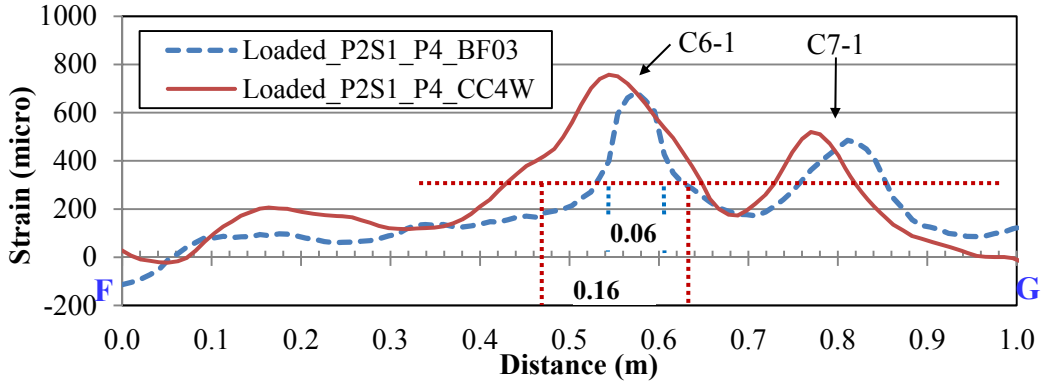
Fig. 5.24. Comparison of the strain distributions in BF03 and CC4W under the loaded truck.

(2) Panel 03

P3 cracked under the loaded truck as shown in Fig. 5.25. The cracks were detected and identified from the strain distributions. They were successfully localized as shown in Fig.5.26.
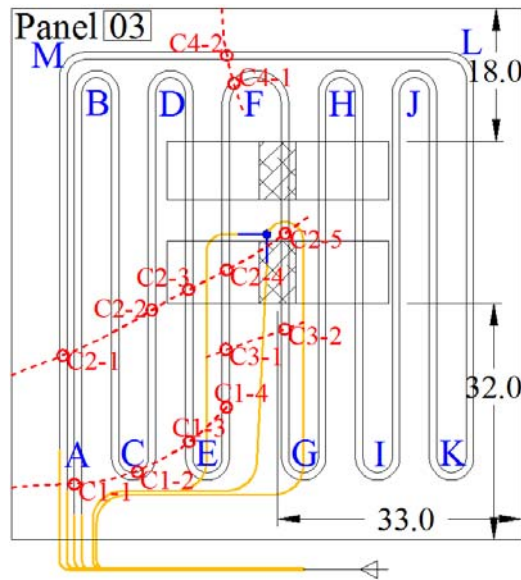
Fig. 5.25. Cracks in P3 under the truck load P2S1.
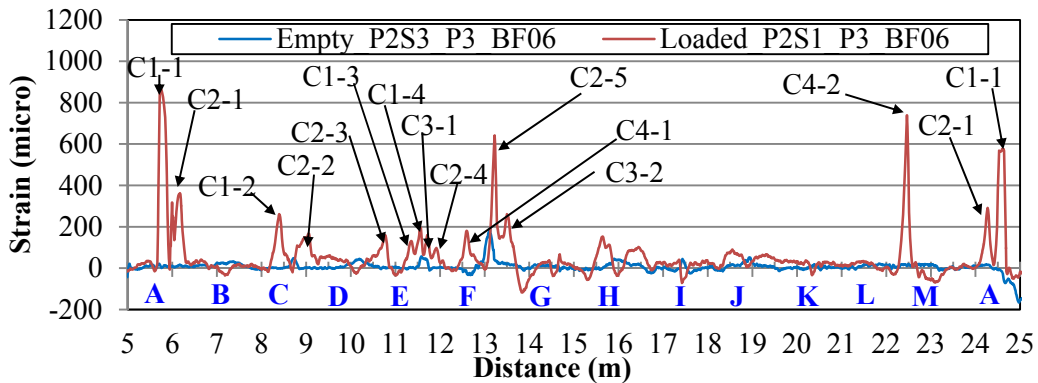
(a) BF06
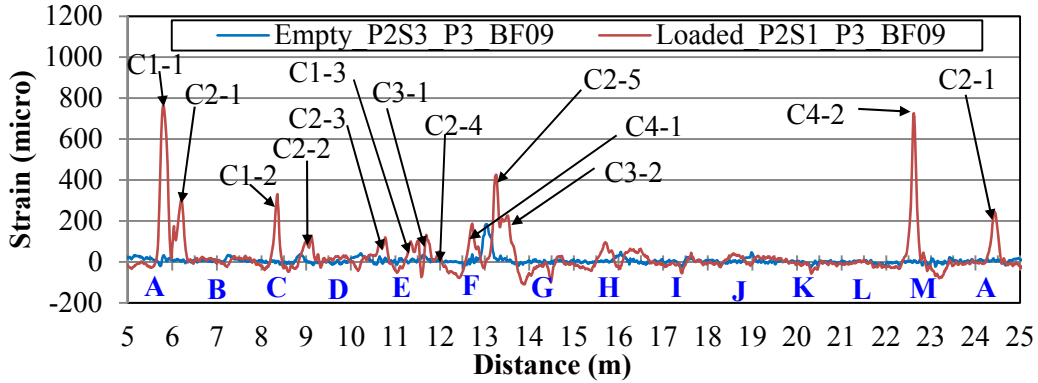
(b) BF09

Fig. 5.26. Strain distribution in P3 under the truck load P2S1.

5.2.5 Second stop of middle pass

The first row of rear wheels were parked on P2 and P5 as shown in Fig. 5.27. P2 was instrumented with BF07, BF08 and TB2. All the three fibers worked. The optical fibers in P5 damaged during the panel fabrication. Strain distributions were collected from the optical fibers in P2 by the Neubrescope.
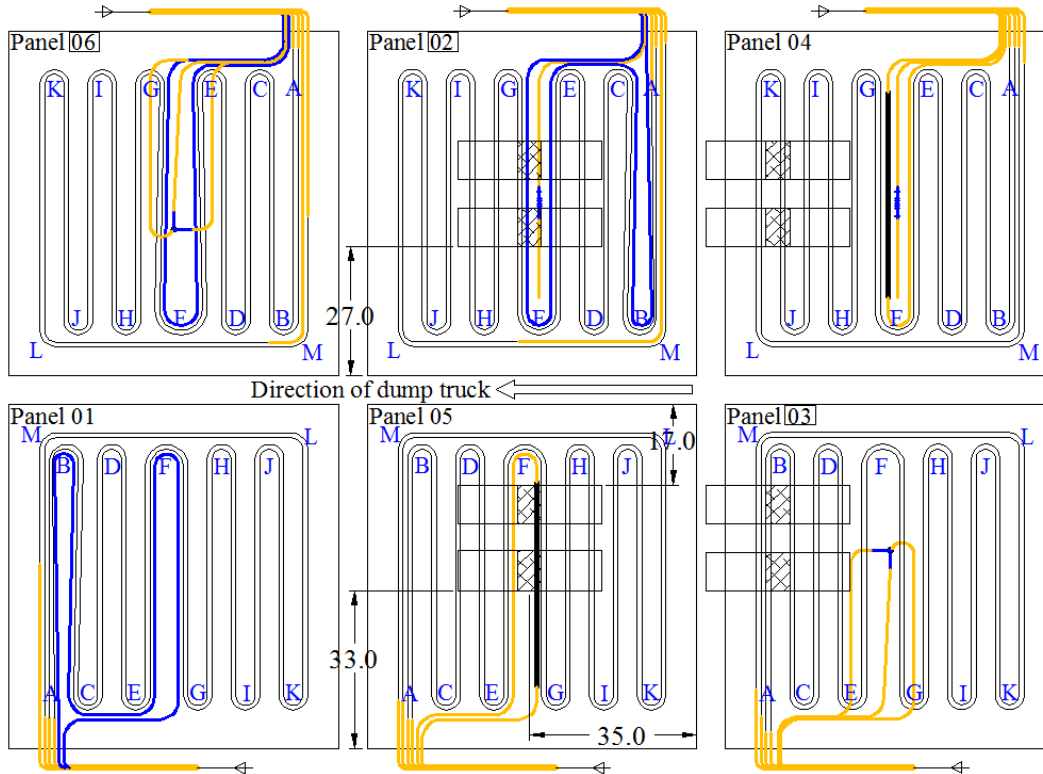
Fig. 5.27. Position of the truck load P2S2.

Fig. 5.28 shows two new cracks (2 and 3) under the truck load P2S3. The cracks crossed the centerline of the panel. The two cracks are significantly reflected in the peaks of strain distributions as presented in Fig. 5.29. The measured strain distributions by BF07 and BF08 are compared well as seen in Fig. 5.30.

51
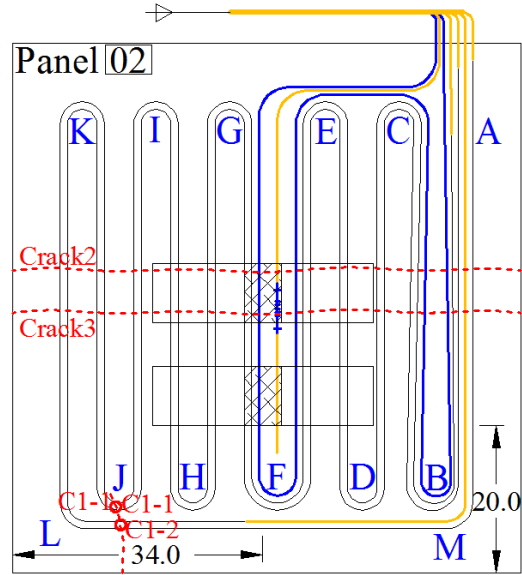
Fig. 5.28. Cracks in P3 under the truck load P2S2.
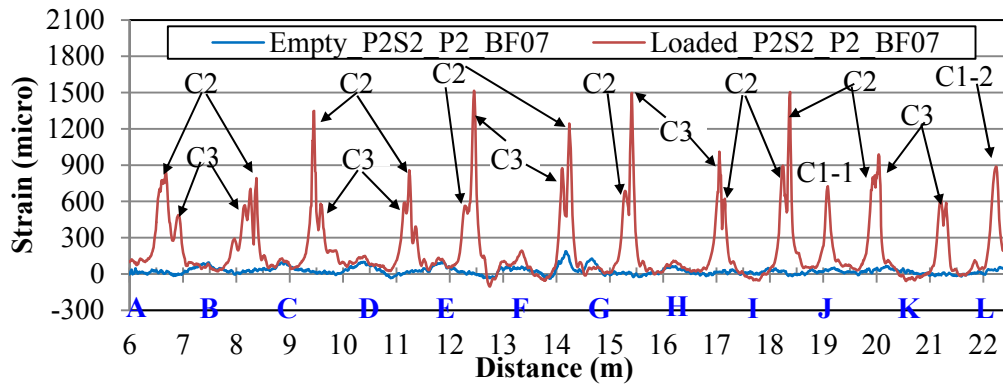
(a) BF07
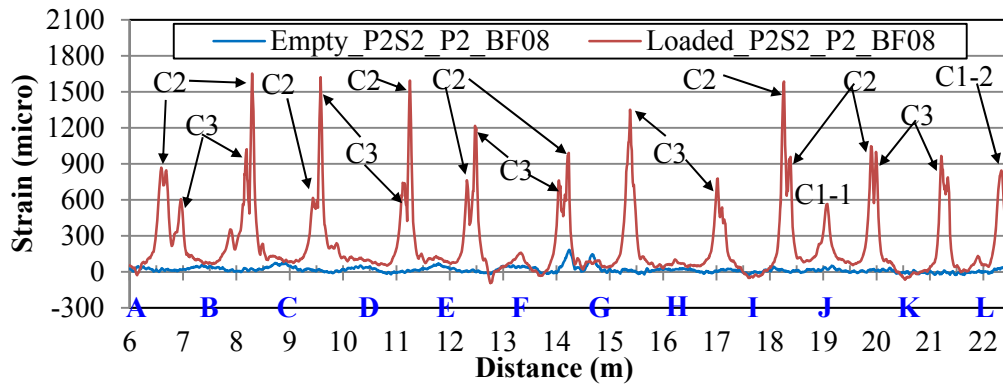
(b) BF08

Fig. 5.29. Strain distribution in P2 under the truck load P2S2.
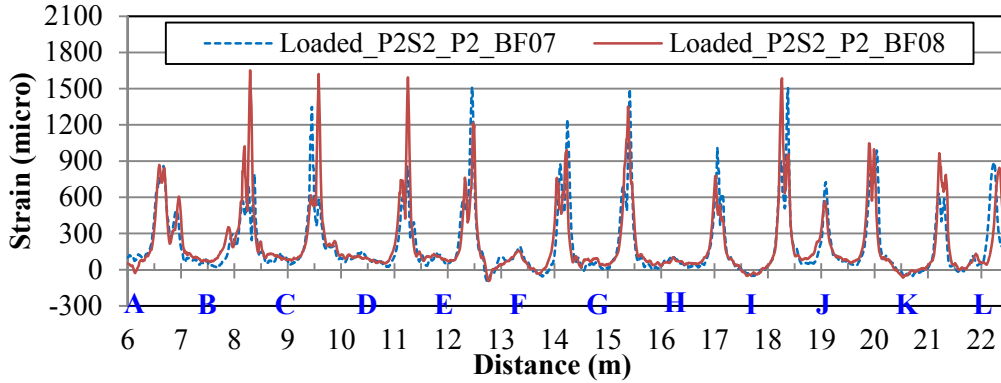
Fig. 5.30. Comparison of the strain distributions in BF07 and BF08 under the loaded truck.

5.2.6 Third stop of middle pass

The first row of rear wheels were parked on P1 and P6 as shown in Fig. 5.31. P1 was instrumented with BF01, BF13 and TB1. BF01 and BF13 damaged during concrete pouring. P6 was instrumented with BF05, BF18 and TB3. All three fibers worked. Strain distributions were collected from the optical fibers in P1 and P6 by the Neubrescope. As illustrated in Fig. 5.32, more cracks appeared under the truck load P2S3 when compared with the case P1S3. The additional cracks correspond to the peaks in strain distributions as shown in Fig. 5.33.
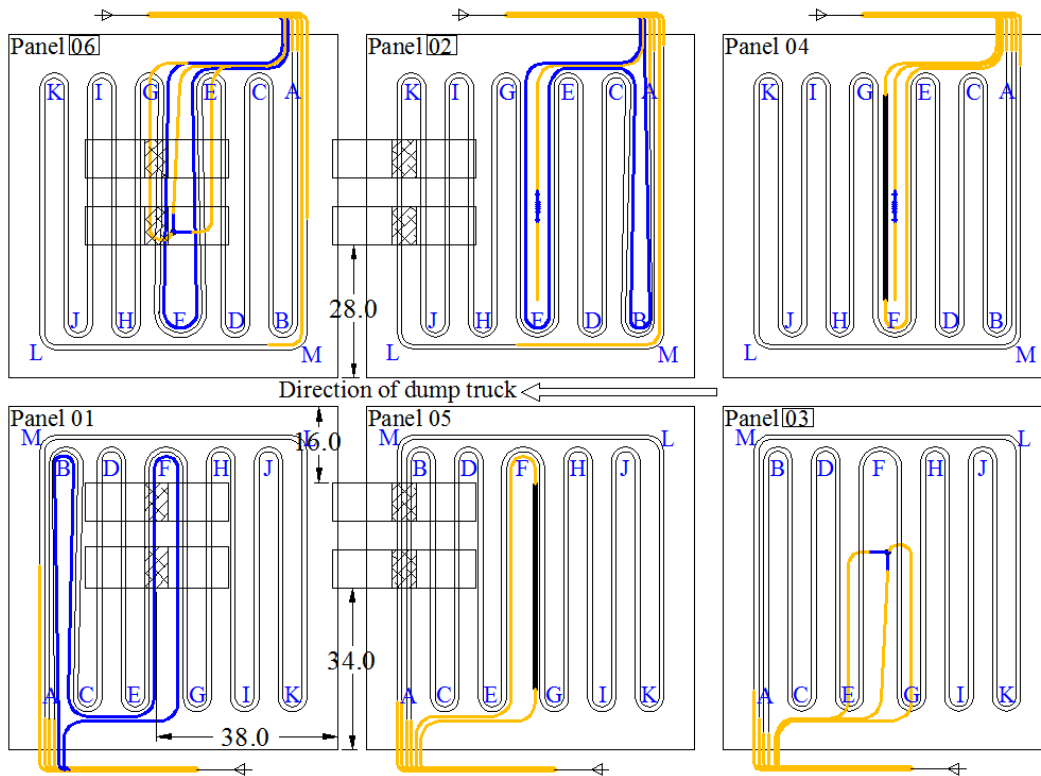
Fig. 5.31. Position of the truck load P2S3.

53
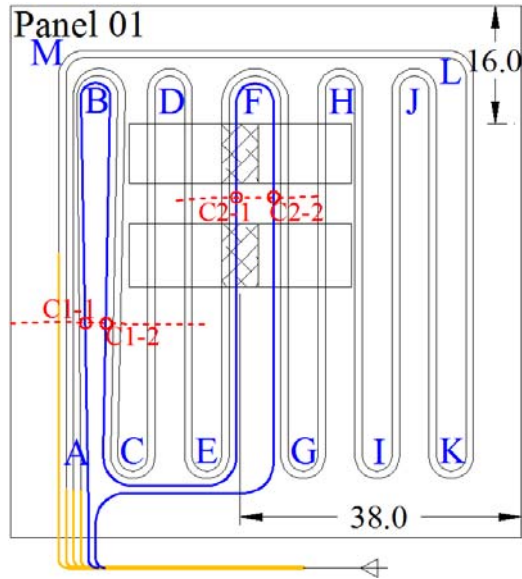
Fig. 5.32. Cracks in P1 under the truck load P2S3.
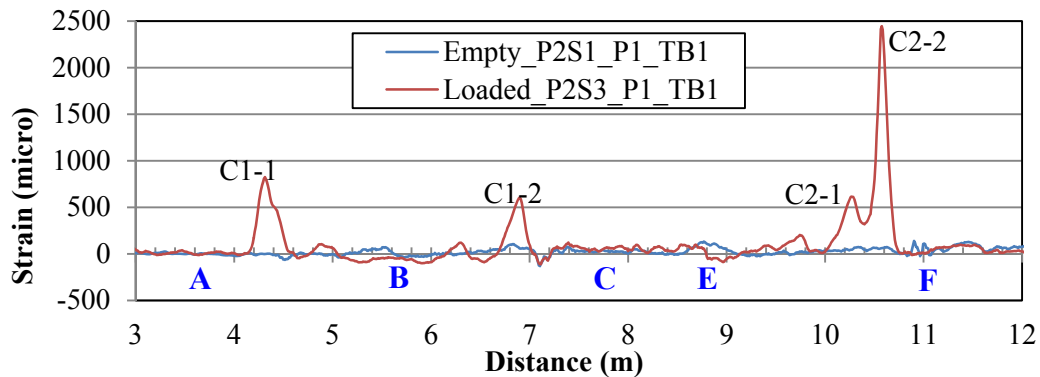
Fig. 5.33. Strain distribution in P1 under the truck load P2S3.

5.3 Substrate movement test

A piece of plywood (4' by 4' by 1/8") was placed underneath the side of P4 to simulate the vertical faulting in application. Fig. 5.34 shows the location and the dimensions of the plywood. The first row of rear wheels were parked on P3 and P4 as shown in Fig. 5.34.
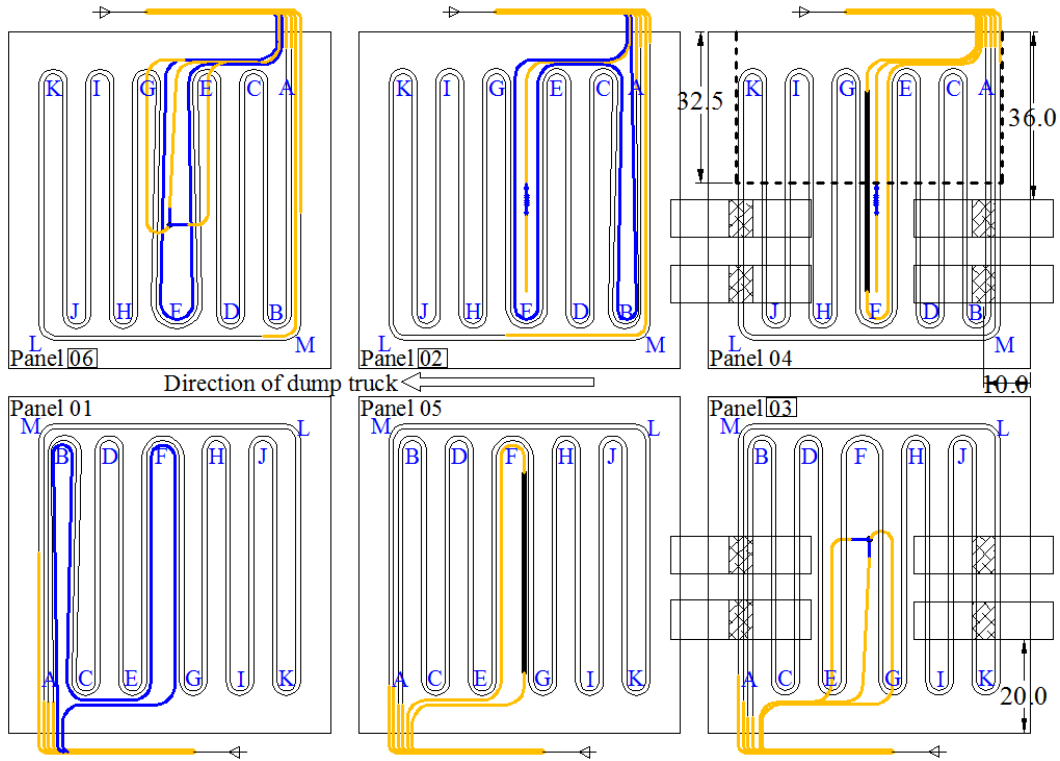
Fig. 5.34. Position of the plywood for substrate movement test.

Under the loaded truck, cracks along the faulting were widened and some cracks propagated as shown in Fig. 5.35 in which only new intersections and significantly changed intersections were marked. Fig. 5.36 shows that more intersection points of the cracks and optical fibers were captured by the distributed optical fibers. Compared with the two peaks in Fig. 5.23(b), Fig. 5.36 only shows one peak. It was because the two peaks could no longer be distinguished when the fiber between the two cracks was de-bonded with the concrete and thus just one peak was detected.
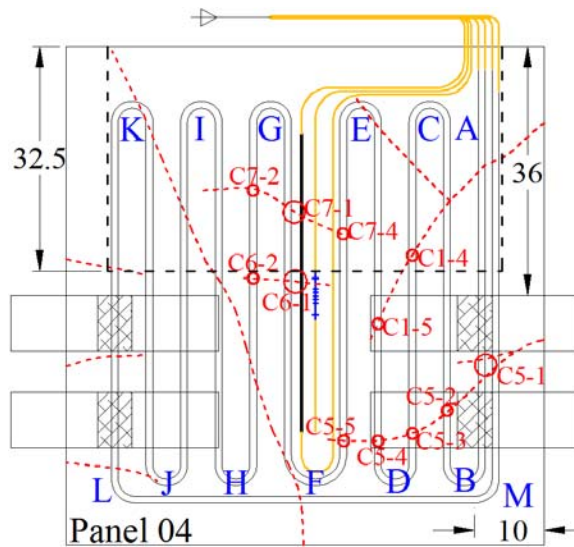
Fig. 5.35. Cracks in P4 under truck load with substrate movement.

55

(a) BF03

(b) CC4W
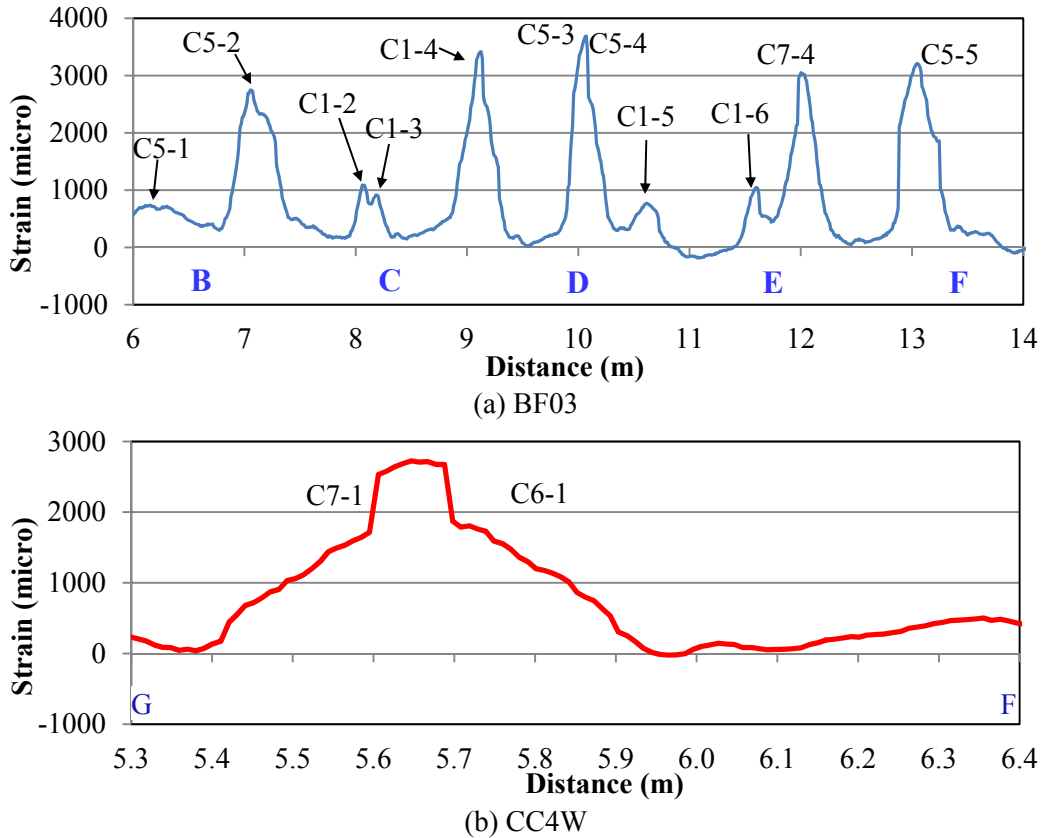
Fig. 5.36. Strain distributions in P4 under the truck load with substrate movement.

5.4 Summary and remarks

Six full-size concrete panels instrumented with three types of optical fibers and two types of FBG sensors were first loaded by an empty and fully loaded dump truck without substrate movement. They were then loaded by a loaded truck with a substrate movement simulated by a vertical faulting under each panel.

Under either the empty or fully loaded truck, strain measurements were taken from optical fibers in room temperature. Strain distributions were obtained from the three types of optical fibers and the results from different optical fibers in each panel were in good agreement. Micro cracks appeared under the truck loading tests due to the uneven floor in the laboratory. They were successfully detected by the three types of optical fibers. When crossed a crack, an optical fiber at the intersection point was subjected to a significant strain peak due to sudden extension. Hence, cracks were well reflected by corresponding sharp peaks in the strain distributions. Their locations were in good agreement. The magnitude of a strain peak corresponded to the width of a crack.

The performances of the three types of fibers were compared. The BFs were observed to have the highest spatial resolution for strain measurement and most sensitive to strain change or micro cracks. The CCs were most rugged, but not as sensitive to micro cracks and robust in micro crack measurement as the bare fiber. The ruggedness and sensitivity of the TBs were in between the BFs and the CCs. The strain distribution resulted from the three optical sensors are in good agreement, and can be applied to successfully locate cracks in the concrete panels. The three types of fibers were functional throughout the truck loading tests.

56

Chapter 6 Load frame tests in laboratory

6.1 Test setup

Following the truck load tests, the concrete panels were loaded to failure with a load frame under a "three-point" bending in displacement control as shown in Fig. 6.1. The panels were simply supported on two steel rollers, each tap welded to a steel beam. The load was applied by two 445 kN actuators through a third roller and two rigid cross beams. A 3.2 mm thick neoprene rubber strip was placed between the concrete surface and the roller. The clear span length between supports was 1.5 m. For each test, the applied load and its corresponding deflection of the panel were recorded by the load cell and the extensometer of the actuators with 10 Hz sampling rate. The strains in the distributed optical fibers and FBG sensors were simultaneously measured by a Neubrescope and an Optical Sensing Interrogator, respectively.
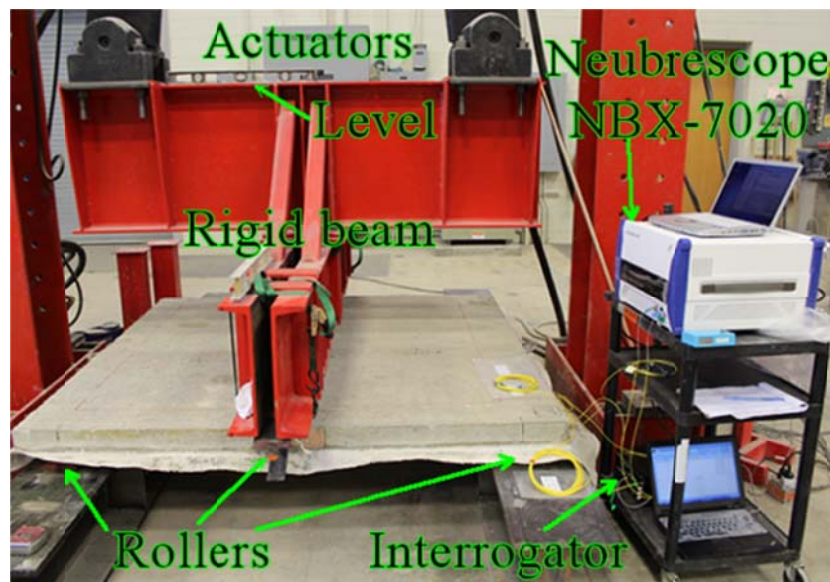
Fig. 6.1. Load frame test setup.

6.2 Mechanical performances of PCC panels

Each PCC panel was reinforced with engineered alloy synthetic macro fibers. In addition, the porous fabric sheet placed at the bottom of the panel during concrete casting became an integral part of the test specimen and functioned like reinforcement. It was observed during the load frame tests that all the panels experienced extensive deformation prior to flexural failure, indicating ductile behavior. The synthetic macro fibers can arrest concrete cracks from leading into brittle failures and thus improve the ductility of concrete panels. In this study, the fabrics were found to appreciably improve the strength and ductility of concrete panels.

Fig. 6.2 shows the load-deflection relations of the six panels tested in the laboratory. As introduced in Chapter 4, there was a fabric sheet placed at the bottom of each concrete panel. To evaluate its effect, the fabric sheet in P5 was removed before the panel was tested. Hence, P5 was considered as a reference that was compared with other panels enhanced by fabrics. P4 was already in poor condition under the truck load with substrate movement. It behaved quite differently from the other five panels as shown in Fig. 6.2. It had the lowest ultimate load and a short linear-elastic behavior as observed from the force-deflection curve.
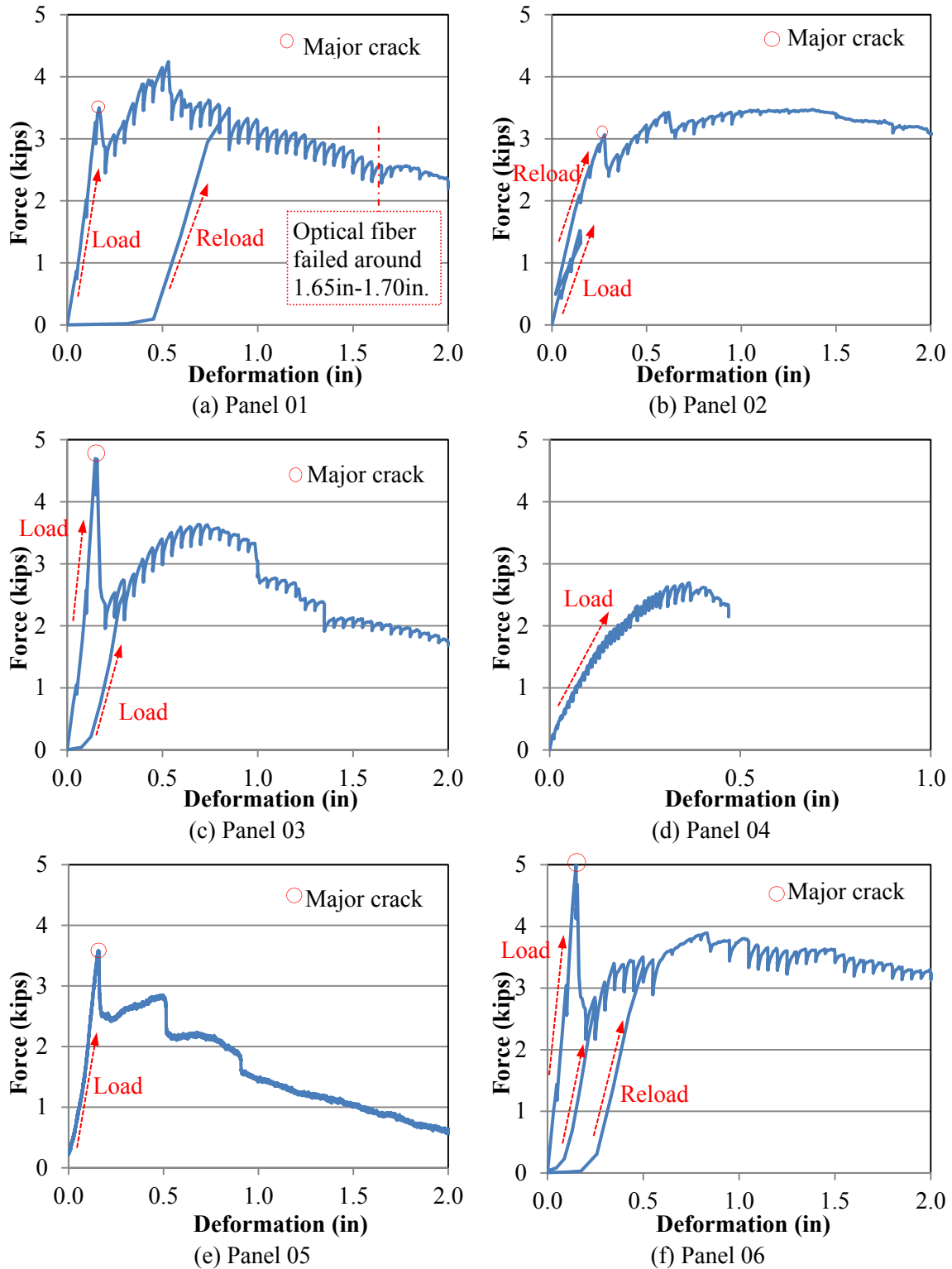
Fig. 6.2. Force-deflection relations of tested panels.

Compared with P1-P3 and P6, P5 gained very limited capacity from the hardening process after the major crack appeared. It was because P5 only benefited from the synthetic macro fiber that was mixed into concrete while other panels also benefited from the fabrics. In addition, P5 had nearly zero residual

load capacity after the short hardening process while the other panels fluctuated between 2 and 3 kips since the fabrics restrained the propagation and widening of the cracks. Therefore, the fabrics were effective to enhance the behavior of concrete panels. The enhancement mechanism was similar to how the concrete was reinforced by rebar. The attached fabrics contributed to the resisting tensile force. When concrete cracked at the bottom face due to tension, with the increase of the crack width, the attached fabrics were subjected to tension as well and thus prevent the crack from further propagating similar to the function of synthetic macro-fibers. Concrete is strong in compression and the fabrics working together with the concrete can resist the tensile force at the bottom the panel. This is why a high load capacity was achieved with the use of fabrics. Eventually, the panels failed due to concrete crushing while the fabrics remained intact.

Both the synthetic macro fibers and the fabrics could enhance the capacity and ductility of concrete panels. The main difference between their functions was their bonding in concrete. The fabric sheet and the concrete bonding were more reliable because of two reasons. First, the bonding area was sufficient since the concrete panel was cast on the whole piece of fabrics. In addition, the bonding between the fabrics and the concrete was very strong. When concrete was poured on the fabrics, a part of mortar seeped in the porous fabrics, gradually forming an integral product. Once the concrete was hardened, the only way to remove the fabrics from the concrete panels was to break either the concrete or the fabrics. When the fabrics were removed from P5, the fabrics were totally damaged and a portion of fabrics remained within the concrete as shown in Fig. 6.3. The bonding strength was so high that the fabrics can only be removed piece by piece. In addition, Fig. 6.3 shows that the enhancement of the fabrics was more effective than that of the synthetic macro-fiber. P5 only gained about 0.32 kip from the hardening effect. However, the other panels except for P4 gained 0.87~1.88 kips from the hardening.

Fig. 6.3. Removal of the fabrics from concrete panel.

6.3 Strain measurements with distributed optical fibers

(1) Panel 01

After P1 was loaded to failure, the fabric sheet was removed to inspect the crack distribution at the bottom of the panel as shown in Fig. 6.4. The blue dotted line represents the TB1 sensor installed at the bottom of the panel, the red line highlights the cracks, and the black circles marks the intersections of TB1. The locations of the cracks were measured by a tape and compared with the locations of the peaks in strain distributions measured by TB1 as shown in Fig. 6.5. It can be observed form Fig. 6.5 that the strain peaks corresponded well to the locations of the cracks.
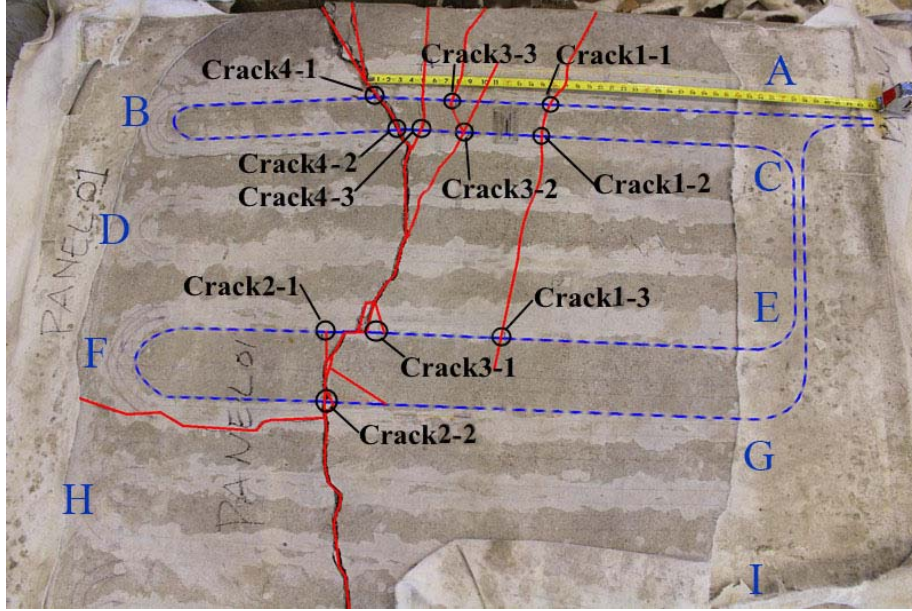
Fig. 6.4. Cracks in P1 after the load frame test.
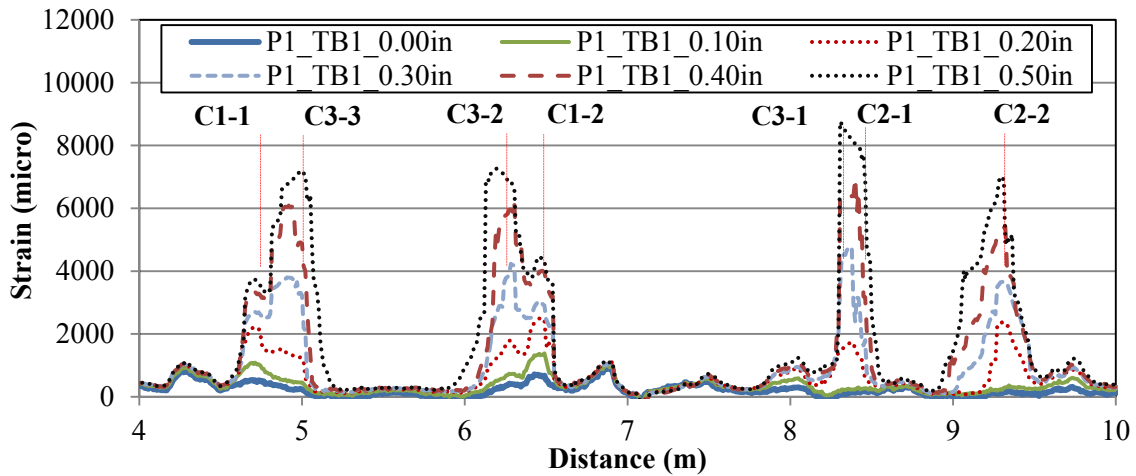
(a) Results with 0.1 in deflection increment
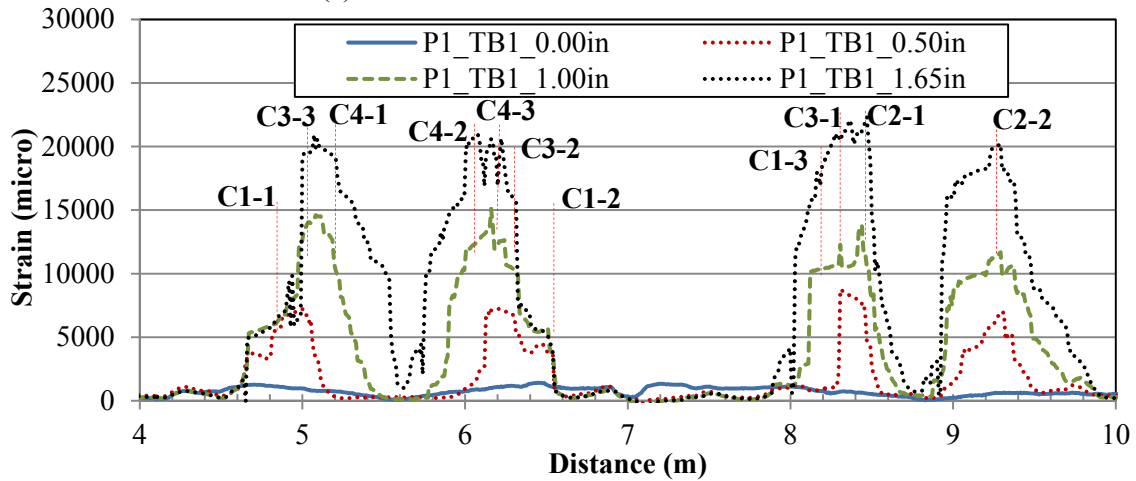
(b) Results with 0.5 in deflection increment

Fig. 6.5. Strain distributions in P1 by TB1.

60

Fig. 6.5 shows that the magnitude of a peak increases with the increase of the loading level, which represents the widening process of the crack. The magnitude of a peak represents the maximum strain in an optical fiber portion at a crack position. Due to the bonding between the concrete panel and the optical fiber, when the crack is widened, the optical fiber will be further stretched and subjected to higher strain. This process is reflected in the increase of the peaks in strain distributions.

In addition to the widening of the existing cracks, the propagation of the existing cracks and the appearance of new cracks were also detected by the distributed optical fiber. As shown in Fig. 6.5, new peaks appeared with the increase of the deformation. The red dot line corresponds to 0.20 in deflection at mid-span, the blue dash line corresponds to 0.30 in deflection in Fig. 6.5(a). Compared with the red dot line for 0.20 in. deformation, a new intersection point C3-3 is observed in the blue dash line for 0.30 in. deflection, which means either a new crack or the propagation of an existing crack.

It can also be observed from Fig. 6.5 that the widths of the strain peaks increase with the deflection when the magnitude of the peak exceeds around 4000 με. There were two mechanisms for this phenomenon. First, some hairline cracks appeared near the major cracks. In fiber reinforced concrete structures, densely distributed hairline cracks are commonly observed since the fibers can restrain the widening of cracks. Another mechanism was about the strain transfer by the buffer and the coating of the optical fiber. Under high strain level, the strain transfer mechanism can be influenced by the de-bonding or local break of material or their combination. The tight buffer and coating can be modelled by an elasto-plastic material that exhibited plastic behavior and the bonding between the buffer and the coating of the fiber can be impaired at high strains. Once the bonding was reduced, when the fibers were stretched, the buffer would no longer be tight and thus cannot well restrain the elongation of the core and cladding of the fiber. Therefore, there would be an extra length of the core and the cladding being stretched to a high strain level. Indeed, evidences for both mechanisms were observed after the bottom fabric sheet was removed from the panel. For instance, Fig. 6.4 shows that C1-1, C3-3, and C4-1 were closely spaced.

(2) P2

P2 was loaded to failure. The locations of cracks were determined and compared with the locations of the peaks in strain distributions measured by BF07 and TB2 as shown in Figs. 6.6 and 6.7. They were corresponded each other very well. Figs. 6.6 and 6.7 indicate that the magnitude of a peak increases with the increase of the loading level, which represents the widening process of the crack. In addition to the widening of existing cracks, the appearance of new cracks was detected by the distributed optical fiber as shown in Fig. 6.6. When the panel was unloaded, the cracks were closed and the corresponding strains decreased. However, the minimum crack widths were observed after unloading as shown in Fig. 6.6. Similar mechanisms can be used to explain crack widening under increased loading as shown in Fig. 6.7.
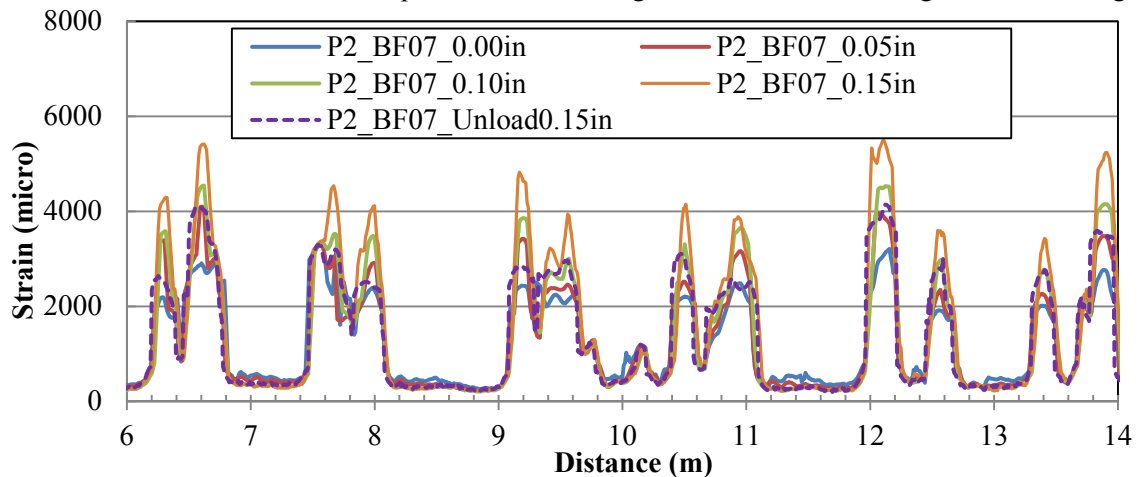
Fig. 6.6. Strain distributions in P2 by BF07.
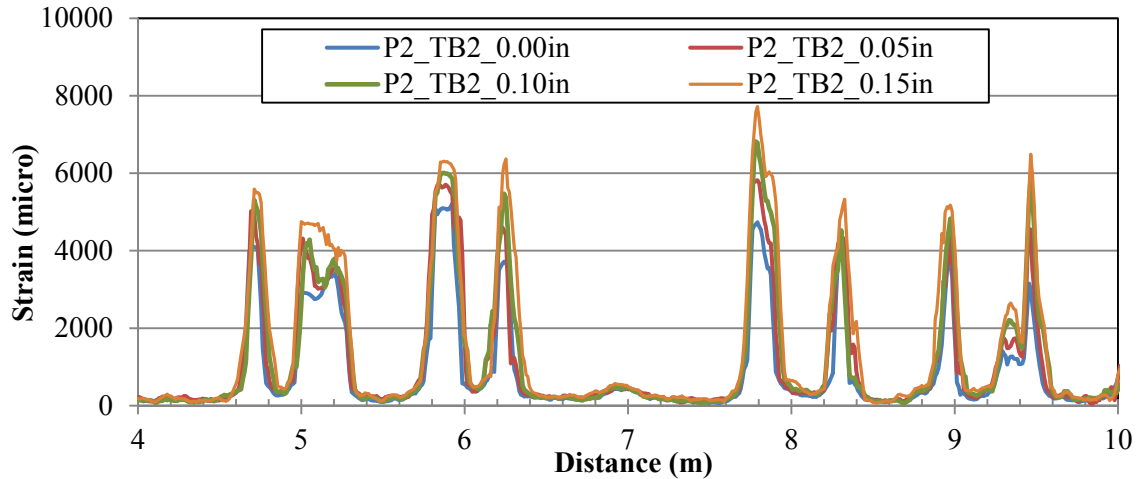
Fig. 6.7. Strain distributions in P2 by TB2.

(3) P3

The fabric sheet was removed to show the crack distribution at the bottom of the panel as shown in Fig. 6.8. Once again, the locations of cracks corresponded very well to the locations of peaks in strain distributions measured by BF06 and BF09 as shown in Figs. 6.9 and 6.10.

Fig. 6.8. Cracks in P3 after load frame test.

Figs. 6.9 and 6.10 clearly show that the strain peak increases with the applied loading, which represents the local effect of crack widening. In addition to the widening of existing cracks, new cracks also appeared as detected by the distributed optical fiber. As shown in Figs. 6.9 and 6.10 that the new peaks appeared with the increase of the deflection.
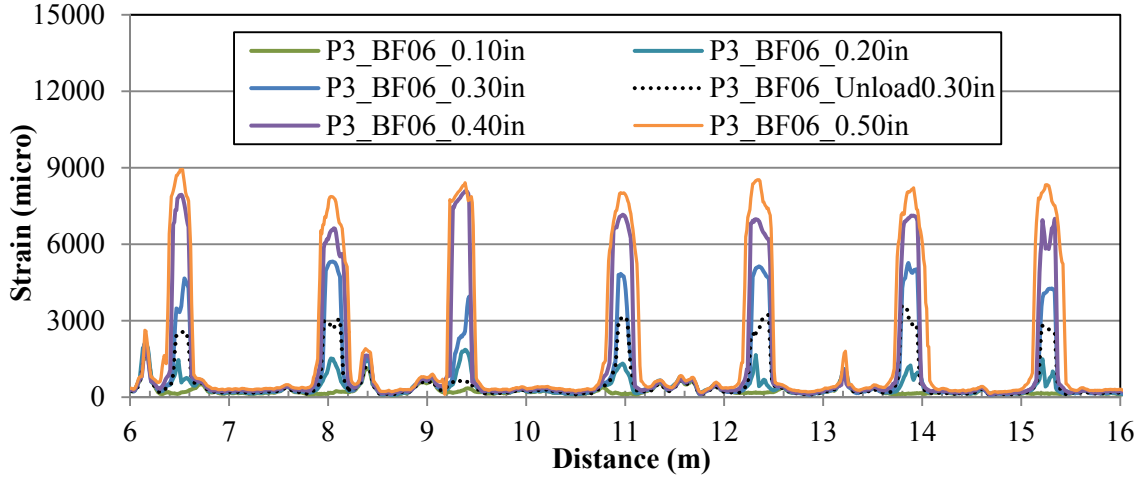
Fig. 6.9. Strain distributions in P3 by BF06.
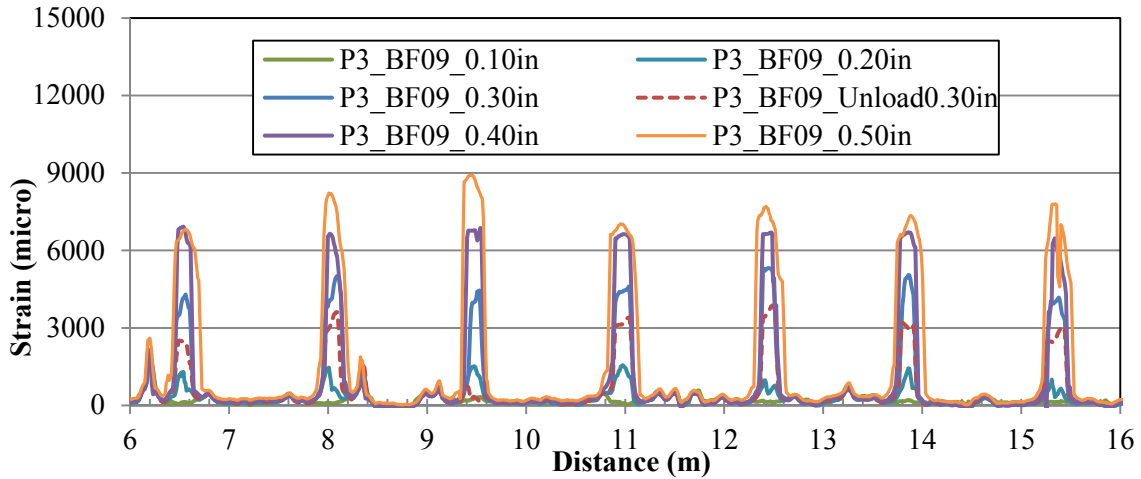
Fig. 6.10. Strain distributions in P3 by BF09.

Besides the distributed optical fibers BF06 and BF09, P3 was also instrumented with a three-dimensional FBG sensor consisting of three legs orthogonal to each other. The X leg was parallel to the distributed optical fibers BF06 and BF09; Y was also in the plane of the panel but perpendicular to BF06 and BF09; Z was perpendicular to the plane of the panel.

The strain measurement results from the 3D FBG sensor in P3 are presented in Figs. 6.11 and 6.12, respectively. Since the major cracks were parallel to the sensors in Y-direction, the strain measurement results from the Y leg were less interested. Only the measurements in X- and Z- directions were included and compared. As shown in Figs. 6.11 and 6.12, the strains changed with the loading level. At the beginning of the tests, the strains approximately linearly increased with the increase of deflection. When the deflection reached 0.15 in, major cracks and many hairline cracks appeared in the two panels, and then the strains nonlinearly increased with the deformation. When the panel was unloaded, the strain did not return to zero, which implies permanent deformation at the sensor location. Figs. 6.11 and 6.12 also show that the strains dropped after the peak values. This is because the major cracks formed close to the FBG sensors but were not across the sensors. When the cracks were widening, the moment values of the sections around the sensors decreased and thus the strain decreased.

Fig. 6.11. Comparisons of strain measurements by BF06 and 3D-FBG-X.

Fig. 6.12. Strain measurements by 3D-FBG-Z in Panel 03.

Fig. 6.11 compares strain measurements by BF06 and its parallel X leg of the 3D FBG in P3. It can be observed that the measurements from the two sensors were very close. Two points in BF06 which were installed close to the position of the FBG sensor were selected for comparison. The distances from the two points to the starting end of BF06 were 11.694 m and 13.285 m, respectively. These two points are selected because the FBG sensor was roughly at the middle of them.

A robust index defined in Eq.(6.1) is to quantify the overall difference between the strain measurements from the two sensors.

$$\tau_s = \sqrt{\frac{1}{N}\sum_1^N[\frac{S_{BF}(i) - S_{FBG}(i)}{\sqrt{S_{BF}(i)}\sqrt{S_{FBG}(i)}}]^2} \tag{6.1}$$

where τ_s denotes the overall difference between strain measurements from the two sensors; i (=1, 2, 3,..., 16) denotes the loading number in this test; $S_{BF}(i)$ and $S_{FBG}(i)$ denote the strain values measured by BF06 and 3D_FBG_01_X corresponding to i, respectively.

Based on the test results, τ_s is 2.12% at 11.694 m distance, and 2.27% τ_s at 13.285 m. The difference between the two sensors mainly resulted from their slight non-collocation. In addition, by averaging the measurements from the two points on BF06, τ_s will be reduced to 1.82%.

BF06 and BF09 stopped working when the mid-span deflection of P3 exceeded 0.7 in, while 3D_FBG_01 continued working until 2.25 in when the transmission cable was broken at the major crack.

On one hand, this clearly indicates that the distributed optical fiber is more advantageous for crack detection than a point FBG sensor. On the other hand, the 3D FBG sensor would appear more rugged than the bare fibers. It is actually subjected to lower strain at failure. As shown in Figs. 6.9 and 6.10, up to 9000 με were sensed by BF06 and BF09 while the highest strain value sensed by the FBG was only 550 με. The data points from BF06 shown in Fig. 6.11 only represent the strains at the location where the FBG sensor was installed in the panel. The main reason why BF06 and BF09 were broken earlier than the FBG sensor was that the transmission cable of the FBG sensor included a layer of spiral steel reinforcement and thus had higher strength than the cables of BF06 and BF09.

(4) P4

At the completion of P4 tests, the fabric sheet was removed to examine the crack distribution at the bottom of the panel as shown in Fig. 6.13. The cracks were localized by measuring their distances to the edges of the panel. The measured distances were compared with the locations of the peaks in strain distributions measured by BF06 and BF09 as shown in Figs. 6.14 and 6.15. The strain peaks were found to correspond well to the locations of cracks in P4.

Figs. 6.14 and 6.15 show that the magnitude of a peak increases with the loading level as a result of crack widening. As introduced in the preceding sections, at the intersections of the optical fiber and the crack that are bonded with each other, the optical fiber is stretched by the concrete due to the crack and subjected to a locally higher strain. Hence, the peaks of the strain distribution represent the detected cracks on the panel. The magnitude of a strain peak can be related to the crack width.

Fig. 6.13. Cracks in P4 after load frame test.
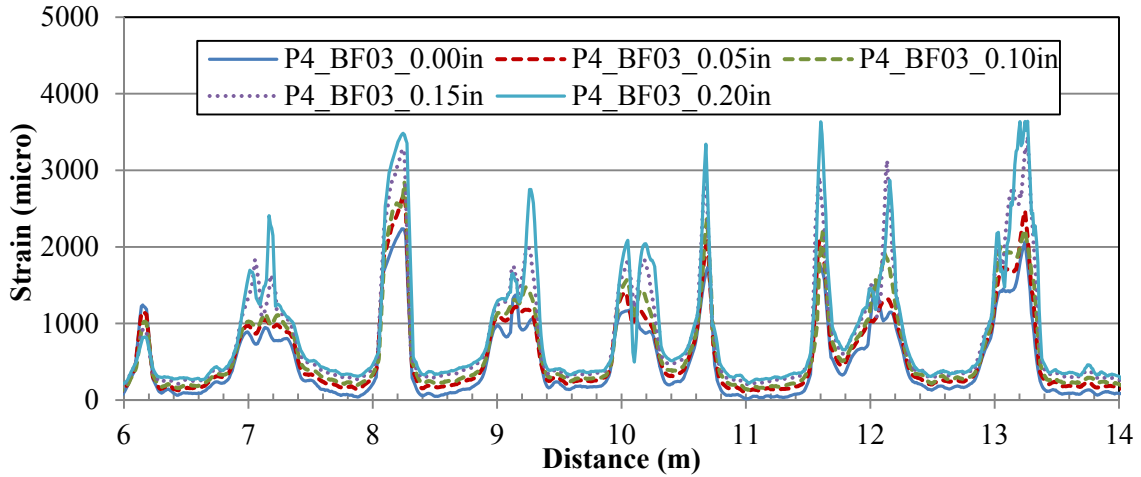
Fig. 6.14. Strain distributions in P4 by BF04.
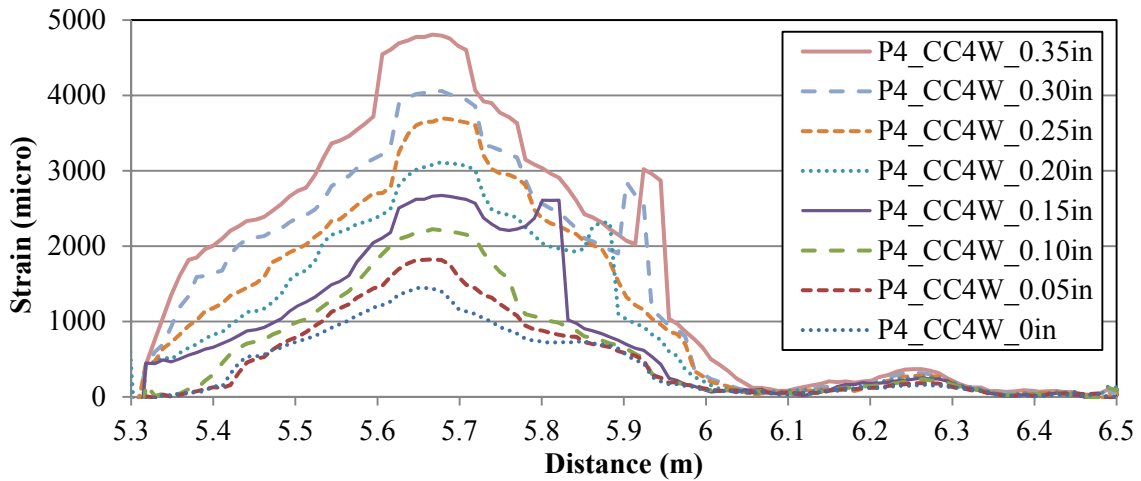
Fig. 6.15. Strain distributions in P4 by CC4W.

(5) Panel 06

After removal of the fabric sheet from P6, the crack distribution at the bottom of the panel was inspected. As shown in Fig. 6.16, the locations of cracks were measured with a tape. The measurements were compared with the locations of the peaks in strain distributions measured by BF06 and BF09 as shown in Figs. 6.17-6.19. It can be observed that the strain peaks correspond well to the locations of cracks.

Fig. 6.16. Cracks in P6 after load frame test.
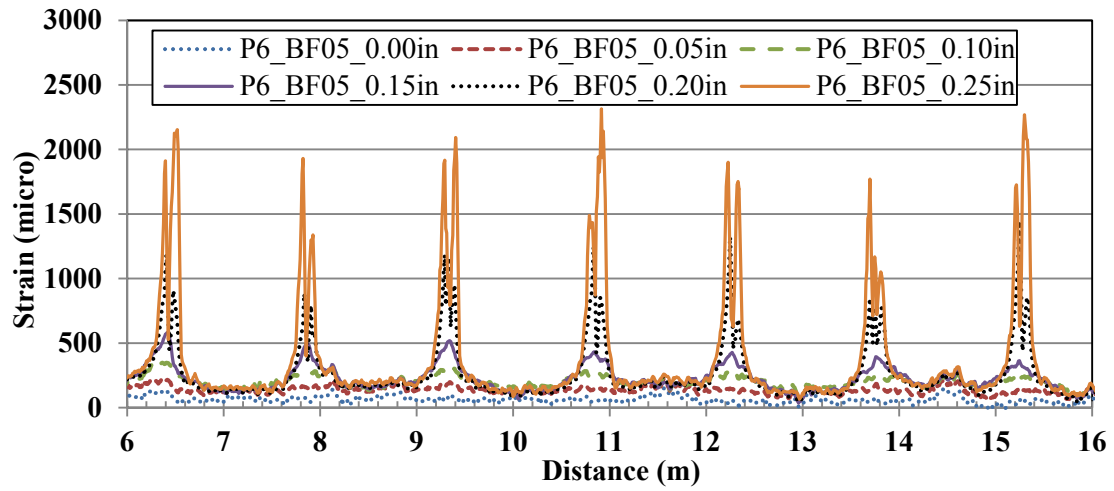
Fig. 6.17. Strain distributions in P6 by BF05.
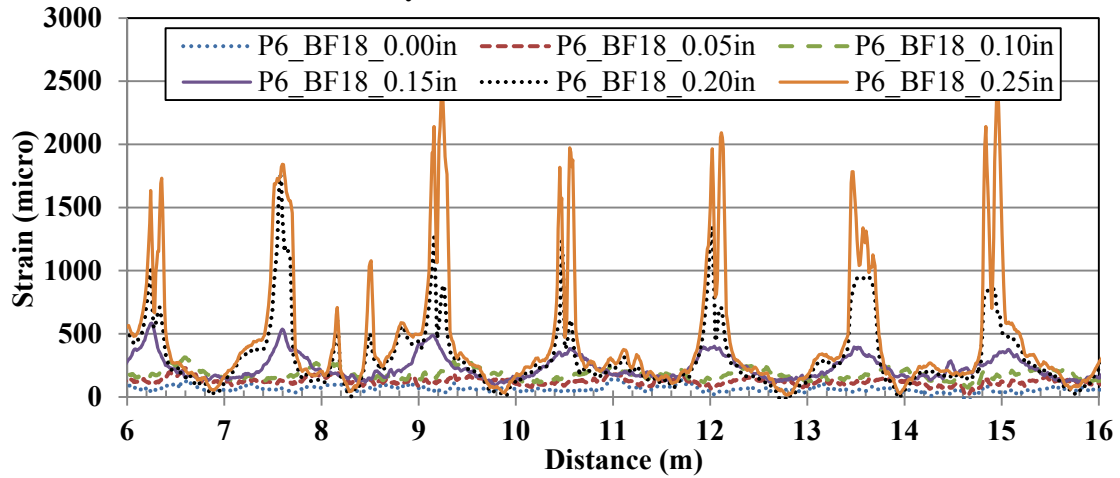
Fig. 6.18. Strain distributions in P6 by BF18.
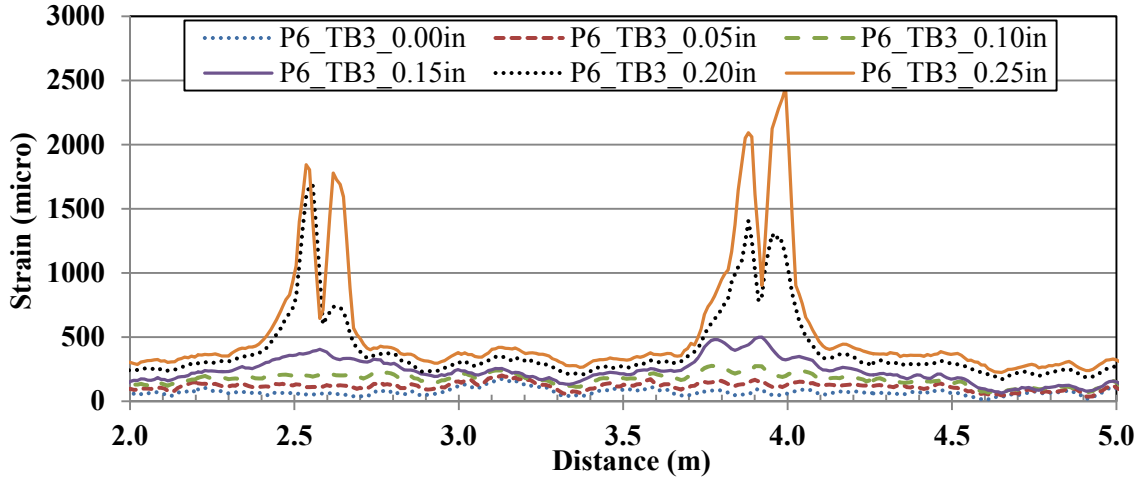
Fig. 6.19. Strain distributions in P6 by TB3.

Figs. 6.17-6.19 show that the magnitude of a peak increases with the increase of the loading level, which represents the widening process of the crack. In addition to the widening of existing cracks, the appearance of new cracks was detected by the distributed optical fiber. As shown in Figs. 6.17-6.19, new peaks appear with the increase of the deflection.

Besides BF05 and BF18, P6 was also instrumented with a 3D FBG sensor consisting of three legs orthogonal to each other. The X leg was parallel to the distributed optical fibers BF05 and BF18; Y was also in the plane of the panel but perpendicular to BF05 and BF18; Z was perpendicular to the plane of the panel. The strain measurement results from 3D FBG sensor in P6 are presented in Figs. 6.20 and 6.21, respectively. Since the major cracks were parallel to the sensors in Y-direction, only the measurements in X- and Z- directions were discussed. As shown Figs. 6.20 and 6.21, the strains approximately linearly increased with the increase of deflection at the beginning and became nonlinearly related to the deflection at 0.15 in mid-span deflection. This was due to the presence of major cracks and many hairline cracks in the panel. When the panel was unloaded, the strain did not return to zero at the sensor location. Figs. 6.20 and 6.21 also show that the strains dropped after passing their peak values. This is because the major cracks formed close to the FBG sensors but were not across the sensors.
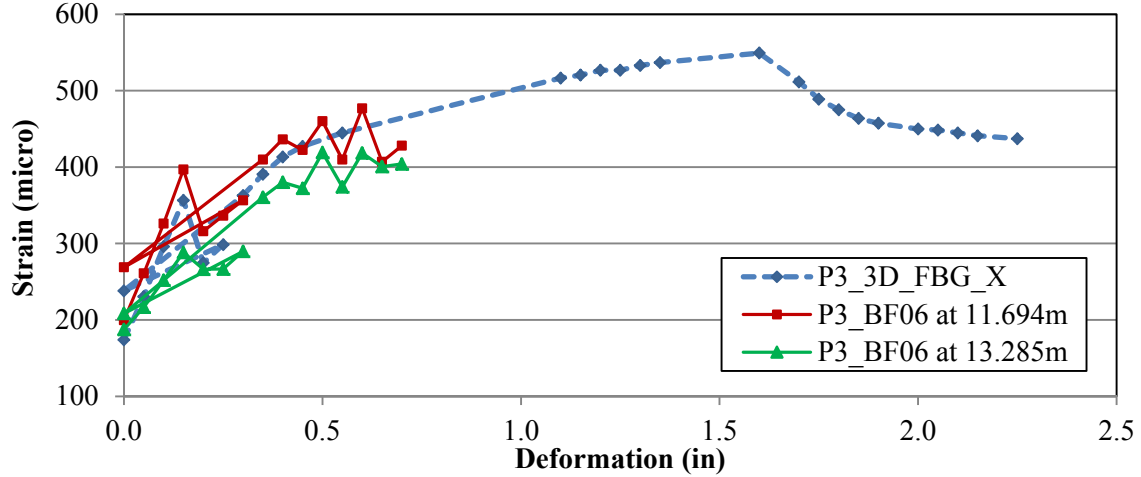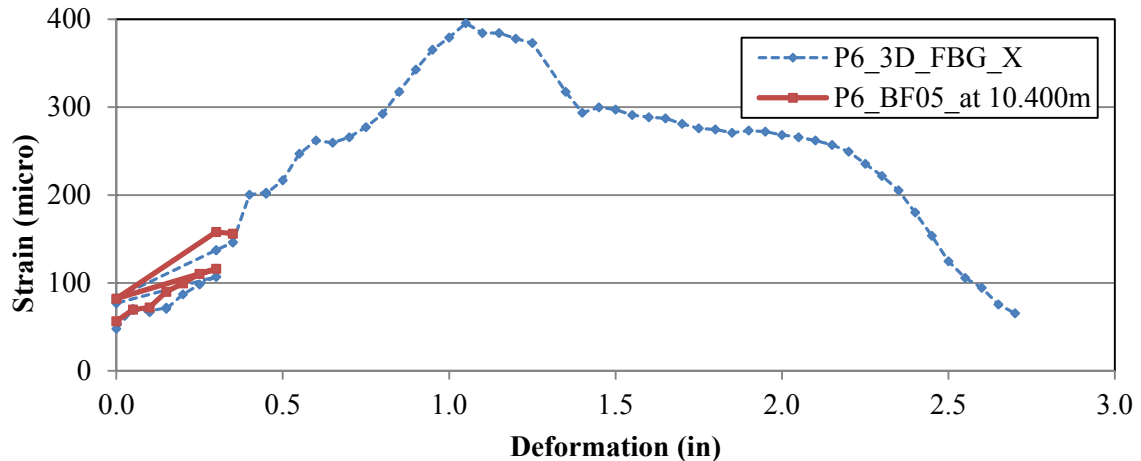

Fig. 6.20. Comparisons of strain measurements by BF06 and BF09 and 3D-FBG-X.

68

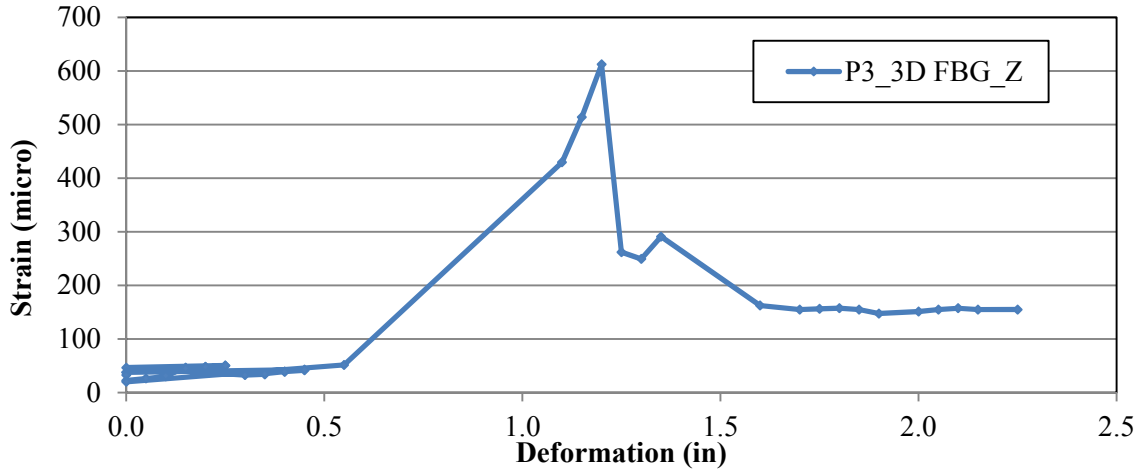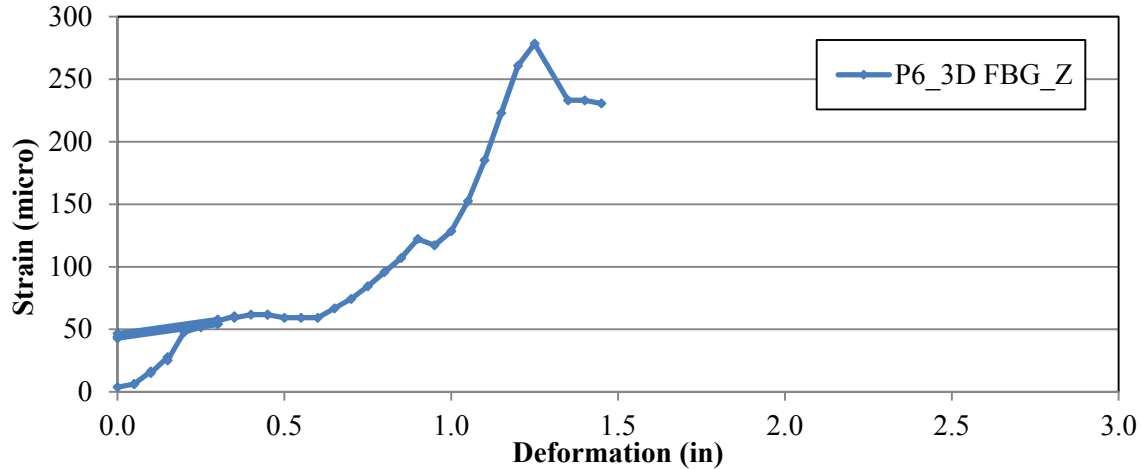**Fig. 6.21. Strain measurements by 3D-FBG-Z in Panel 6.**

Fig. 6.20 compares strain measurements by PBF05 and its parallel 3D-FBG-X. It can be observed that the measurements from the two sensors were in good agreement. Two points in BF05 close to the position of the FBG sensor were selected for further comparison. They are both 10.4 m away from the starting end of BF05. In this case, the robust index as defined in Eq. (6.1) τ_s =3.56%.

BF05 and BF18 stopped working when the mid-span deflection of P6 exceeded 0.35 in while the 3D_FBG_02 continued to work till 2.7 in deflection when the transmission cable was broken at the major crack. Similar to P3, this comparison shows the effectiveness of distributed optical fiber sensors for crack detection. Even though the bare fibers failed early, they were actually subjected to higher strains. As shown in Figs. 6.17-6.19, up to 2500 με were sensed by BF05 and BF18 while the highest strain sensed by the FBG was only 400 με.

6.4 Summary

After the truck load tests, the six panels were tested to failure with a three-point bending setup. By comparing structural performances of the panels, a fabric sheet bonded to the bottom of a panel proved effective as reinforcement. It can significantly improve both strength and ductility of the panel.

Most cracks generated under the three-point load occurred around the mid-span of each panel. They were successfully localized by the strain distributions obtained from optical fibers as verified by tape measurements. The crack widths can be directly related to the peak values in strain distributions as verified by a crack width gauge. The appearance of new peaks in strain distributions represented either propagation of the existing cracks or the initiation of new cracks. The strain peaks are widened as they exceed a threshold of around 4000 με. This phenomenon was related to a change of bonding condition between the optical fibers and their surrounding concrete. At the location of a widening crack, the optical fibers could lose its bond in concrete. In the coating of optical fibers, plastic deformation such as slipping could also occur as the strains applied to the fibers increase.

Strain measurements from Brillouin scattering based optical fiber sensors and FBG sensors were compared well. Due to their distribution nature, the distributed optical fiber sensors are advantageous over the point FBG sensors in crack detection. Measurements from different distributed optical fibers were also compared. Bare fibers have the highest spatial resolution in strain measurement and the highest sensitivity to strain change or micro cracking. Concrete crack cables are most rugged but least sensitive and robust to micro cracking. The ruggedness and sensitivity of optical fibers with tight buffer are in between the bare fibers and the concrete crack cables. The three types of fibers remained functional until major cracks were significantly widened, thus providing a promising tool for real-world applications in pavement engineering.

Chapter 7 In-site tests using FBG sensors

7.1 Sensor layout

In this study, two 1D-GFRP-FBG sensors were deployed inside the existing pavement, and three 1D-GFRP-FBG sensors and two 3D-GFRP-FBG sensors were applied in the newly casted ultra-thin concrete overlay. Figs. 7.1-7.3 show the detailed locations of the deployed sensors. To monitor the propagation of the transverse crack in existing pavement, one 1D-GFRP-FBG sensor (Sensor No. 1D-5) was installed inside the existing pavement as shown in Fig. 7.2 for the sensor location and the photo of the sensor installation as an insert. Polymer had been applied to bond the sensor to the existing concrete pavement. To compare the crack propagation in concrete overlay, another 1D-GFRP-FBG sensor (Sensor No. 1D-4) was placed in the overlay 0.5 in. above the existing pavement at the same location as 1D-5.
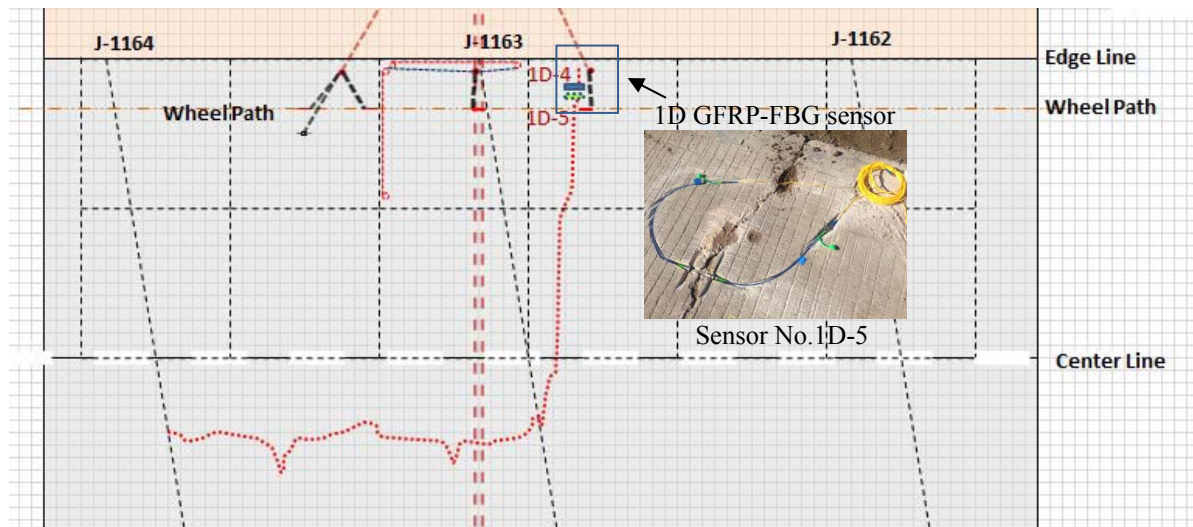
Fig. 7.1. Locations for the 1D-GFRP-FBG crack sensors.

The unbounded ultra-thin concrete overlay used two different fabric thicknesses throughout Cell 40. Therefore, two sets of sensors (East and West Sensor Panel for fabric types 1 and 2, respectively) were placed inside the concrete overlay as shown in Figure 6 for the detail sensor layout. In the East Sensor Panel, an 1D-GFRP-FBG sensor (Sensor No. 1D-3) was placed in existing pavement over a joint and another 1D-GFRP-FBG sensor (Sensor No. 1D-1) in longitudinal direction was placed 0.5 inches from the top of the existing pavement inside the concrete overlay to compare the effects of existing joint to the behavior of the newly constructed concrete overlay. One 3D-GFRP-FBG sensor (Sensor No. 3D-1), two strain gauges, and one thermocouple tree had been placed in the East Sensor Panel. Another 3D-GFRP-FBG sensor (Sensor No. 3D-2), one 1D-GFRP-FBG sensor in transverse direction in the overlay over the existing longitudinal cracks, one strain gauge, and one thermocouple tree were placed in the West Sensor Panel. All 3D-GFRP-FBG sensors were placed 0.5 inches on from the top of the existing pavement inside the overlay. The transmission connections of all the sensors were protected and centrally connected to the instrument at the side. The data collected will be used to analyze the performance and environmental conditions of the ultra-thin concrete overlay.

Fig. 7.2. Sensor layouts on Cell 40.
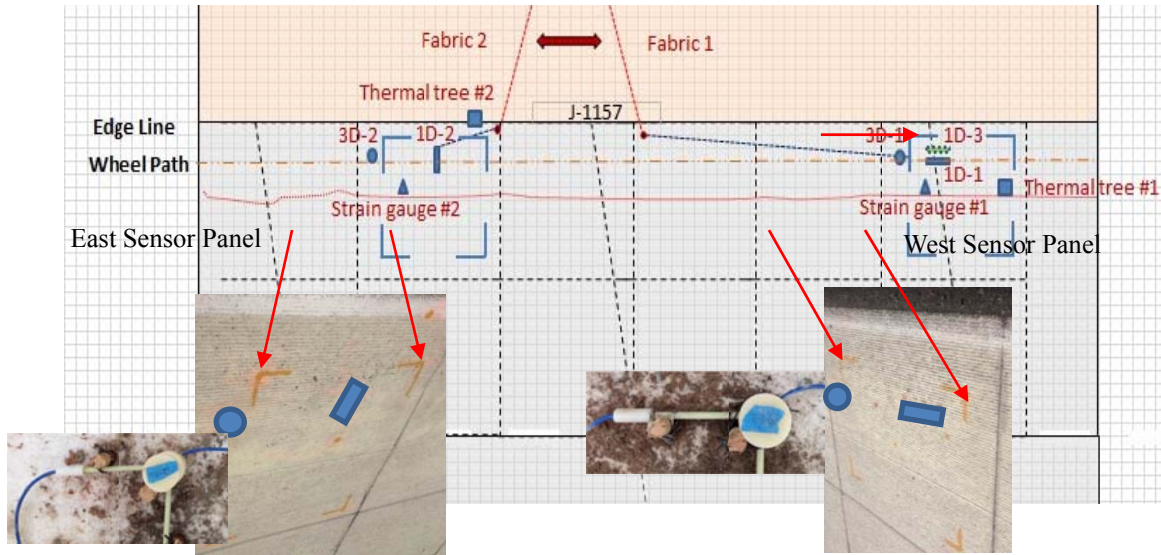
(a) East Panel in Cell 240   (b) West Panel in Cell 140
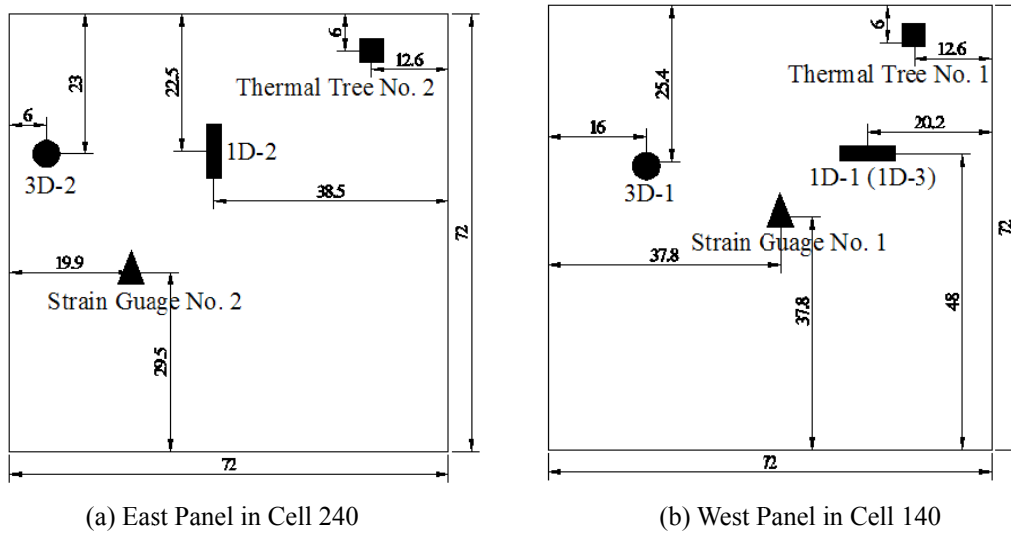
Fig. 7.3. Sensor layouts on Cell 40 (in inch = 2.5cm) [Note: Sensor size not to scale.].

7.2 Static testing and monitoring results

7.2.1 Static field test setup

The ultra-thin concrete overlay was paved with embedded sensors on June 10th 2013 and cured for 28 days (July 8th 2013) before dynamic loading on the pavement as shown in Fig. 7.4(a). A static loading test was performed on August 1st 2013 and April 14th 2014 to evaluate the overlay behavior and sensor functionality. The static and further long-term simulated truck traffic used a MnDOT Truck as shown in Figure 7.4(b) as a loading truck. The truck has five axles and carries a gross vehicle weight of 80 kips. The weights distributed on each tire from front to end, which were loaded on the sensor locations, are 5,800 lbs, 4,025 lbs, 4,525 lbs, 4,300 lbs, and 4,100 lbs, respectively, as shown in Figure 7.4(c). Eight positions were loaded using the MnDOT truck as shown in Figure 7.5(a~h). Loading position 1 had one tire of the front axle loaded on the Sensor No. 1D-1, position 2 loaded on top of the Sensor No. 3D-1 by the same tire as position 1, position 3 used one tire of the second axle loaded on Sensor No. 3D-1, position 4 and 5 loaded one tire of the front axle on Sensor No. 1D-2 and 3D-2, position 6 and 7 had one tire of the second and third axle loaded on Sensor No. 3D-2, and position 8 loaded one tire of the fourth

71

axle on Sensor No. 3D-2.

7.2.2 Static test results and discussion

Table 7.1 shows the measured raw Bragg wavelengths and corresponding strains of all the sensors from the raw data before paving, 21 days (07/01/13), 52 days (08/01/13), 162 days (11/22/13) after paving, and 308 days (04/18/2014). Table 7.2 shows the accumulated raw strains inside the pavements. Compare Sensor No. 1D-1with 1D-3, it can be seen that, the transverse crack in the existing pavements was sealed 0.02% after paving and continuous to seal after 52 days of paving to 0.021%. The crack reopened 0.02% after 308 days of paving. The longitudinal direction of the overlay layer on top of the existing transverse crack was kept in compression during the 308 days after paving with increasing compression strains from -14 μɛ to -516 μɛ from the simulated traffic loading on Cell 40.

The sensor (No. 1D-5) over joint in existing pavement of Cell 40 indicated that the joint closed to a large extent of 0.125% with the paving of the new PCC overlay. After six months of simulated traffic, the existing joint reopened 0.22% compared to the status after paving and after one year of traffic, the joint maintained a reopening of 0.1%. The reopening of the existing joints induced tension stress in the new PCC concrete overlay for a tension strain around 50 μɛ in longitudinal direction in summer but compression in winter of around -0.05% as can be notified from Sensor No. 1D-4. As known, for concrete materials, although the formation of the very first crack is highly dependent on the concrete mix design, it normally will occur with a tension strain of around 100 μɛ because of the tension induced micro cracks (Evans 1968). The reopening of the existing joints may induce future longitudinal or transverse cracks in the new concrete overlay at this specific location, indicating that the locations with existing joints will be weak locations for potential cracks in new concrete overlays.

Fig. 7.4. Photos for overlay after paving, truck and truck dimensions.

Loading Position 2

Loading Position 3

Loading Position 4

Loading Position 5

Loading Position 6

Loading Position 7

Loading Position 8
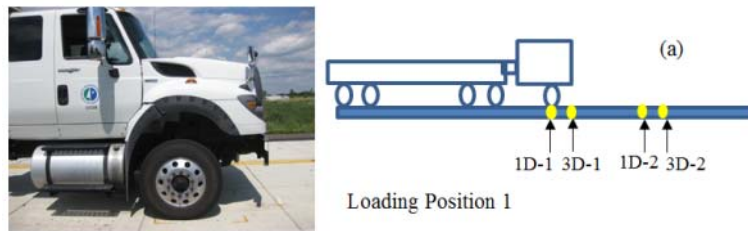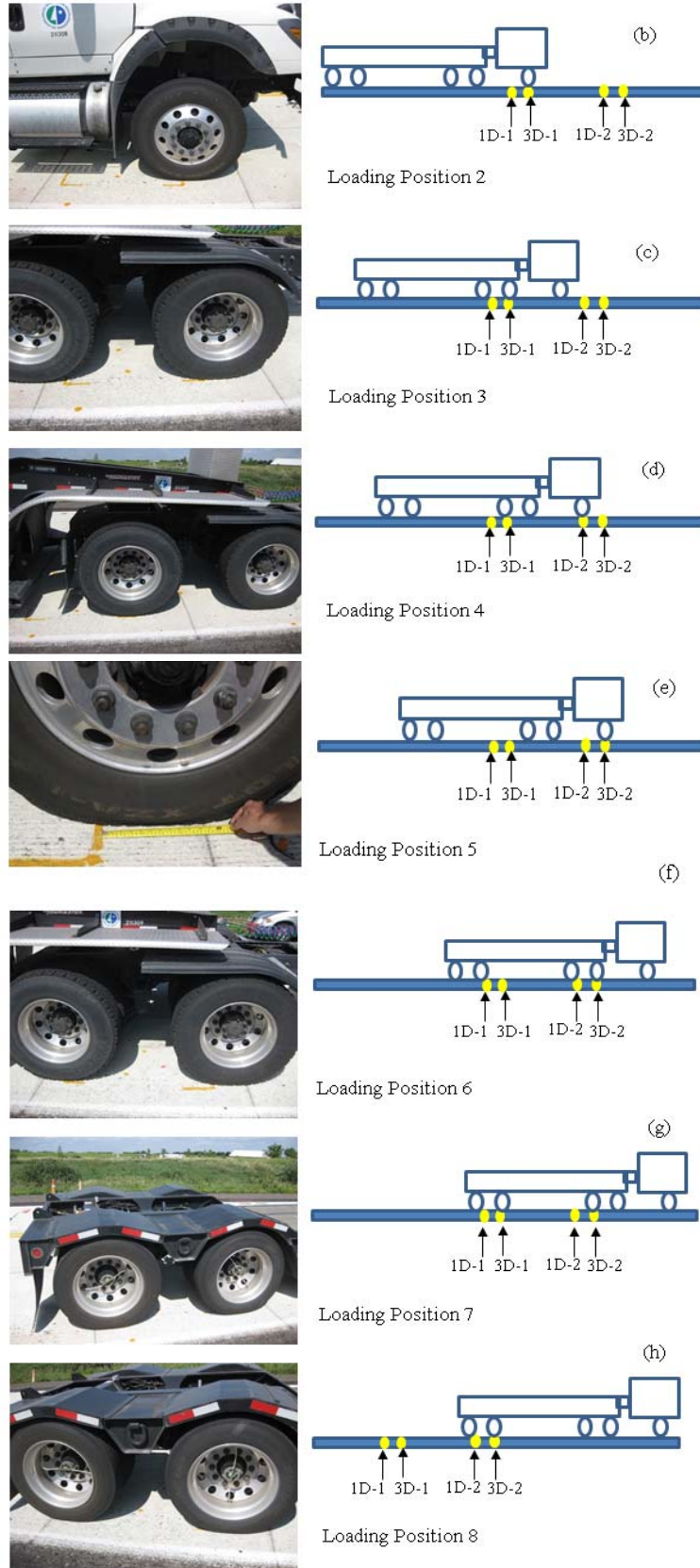
Fig. 7.5. Field static testing setup.

The data from sensors in transverse directions (1D-2, 3D-1-T1, and 3D-2-T1) indicated that the overlay behaved well in transverse direction at the locations without existing joints. Two of the three transverse sensors showed that the overlay was in compression strains with an average of -30 µε in summer and around -500 µε in winter. 3D-2-T1 showed a small tension strain in summer of 35 µε, which worth continuous monitoring to watch for potential transverse cracks. Considering that concrete materials are strong for compression, which can hold compression strain up to two and three thousands of micro strains depending on the mix design of the concrete (Liners 1987), the overlay is performing well in transverse direction. In longitudinal direction, however, the stress development along the pavement longitudinal direction is not uniformly progressed. At the location of Sensor No. 3D-1-T2, compression behavior was noticed with a compression strain of -36 µε, but at sensor location 3D-2-T2, a tension strain of 72 µε was noticed in summer. Extensive compression strains more than -700 µε was noticed in winter in longitudinal directions. Micro longitudinal cracks may develop in small scale inside the concrete overlay. The micro tension cracks could be accounted for various reasons such as concrete shrinkage, temperature variance, freezing and thawing, and non-uniformity of the structural fiber in concrete.

Table 7.1 Measured raw Bragg wavelength and corresponding strain through paving and testing

Sensor No. and directions	Initial wavelength 06/07/13 (nm)	Wavelength after overlay paving (nm) on 07/01/13	Raw Strain (µε)	Wavelength on 08/01/13 (nm)	Raw strain (µε)	Wavelength on 11/22/13 (nm)	Raw strain (µε)	Wavelength on 04/18/14 (nm)	Raw strain (µε)
1D-1 (In existing pavement)	1524.899	1524.743	-197	1524.823	-211	1524.621	-351	1524.018	15
1D-3 (Longitudinal)	1540.011	1540.095	106	1540.069	73	1539.357	-825	1539.686	-410
1D-5 (In existing pavement)	1530.203	1529.211	-1251	1529.445	-956	1530.944	985	1530.055	-186
1D-4 (Longitudinal)	1544.902	1544.891	-14	1544.932	38	1544.48	-532	1544.508	-497
1D-2 (Transverse)	1550.300	1550.488	237	1550.462	204	1549.781	-655	1549.891	-516
3D-1-V (Vertical)	1524.731	1525.093	456	1525.073	431	1524.615	-146	1524.909	25
3D-1-T1 (Transverse)	1534.537	1534.796	266	1534.768	237	1534.134	-414	1534.324	-219
3D-1-T2 (Longitudinal)	1529.137	1529.353	327	1529.349	291	1528.779	-451	1528.916	-278
3D-2-T1 (Transverse)	1544.102	1544.410	388	1544.438	423	1543.878	-282	1544.063	-49
3D-2-T2 (Longitudinal)	1549.205	1549.481	348	1549.538	420	1548.965	-303	1549.178	-34

Table 7.2 Accumulated raw strains

Sensor No. and directions	Strain 08/01/13 (µε)	Strain (11/22/13) (µε)	Strain (04/18/14) (µε)
1D-1 (In existing pavement)	-14	-154	212
1D-3 (Longitudinal)	-33	-931	-516
1D-5 (In existing pavement)	295	2236	1065
1D-4 (Longitudinal)	52	-518	-483

1D-2 (Transverse)	-33	-892	-753
3D-1-V (Vertical)	-25	-602	-431
3D-1-T1 (Transverse)	-29	-680	-485
3D-1-T2 (Longitudinal)	-36	-778	-605
3D-2-T1 (Transverse)	35	-670	-437
3D-2-T2 (Longitudinal)	72	-651	-382

. (a) West Panel in Cell 140   (b) East Panel in Cell 240
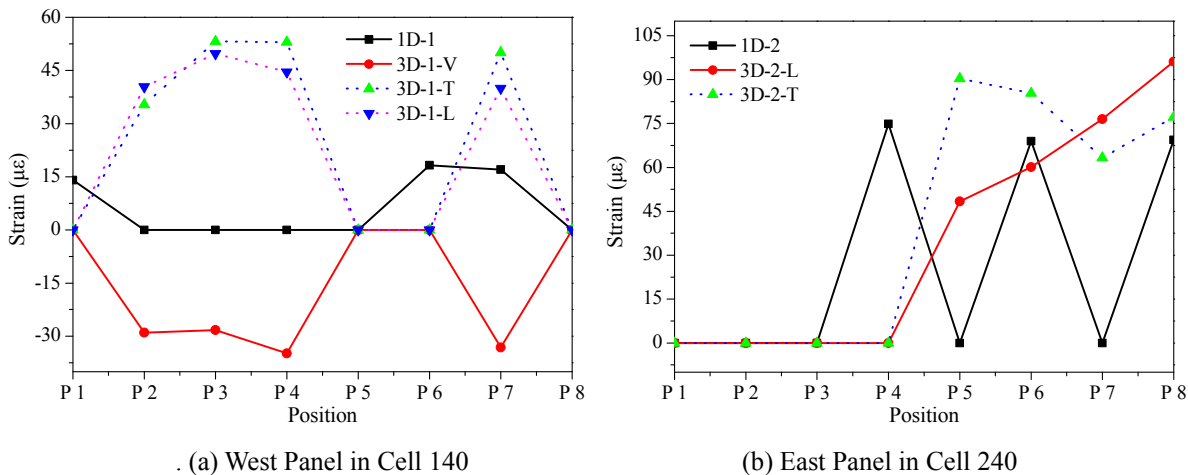
Fig. 7.6. Measured strains throughout static testing (after temperature compensation).

The measured strains after temperature compensation from the static field loading tests are shown in Figure 7.6(a) for West Sensor Panel and Figure 7.6(b) for East Sensor Panel. A static loading of 5.8 kips on the pavement overlay developed a tension strain around 50 με in transverse direction, a tension strain round 40 με in longitudinal direction, and a relatively small compression strain in vertical direction around -35 με. The small compressive strain is likely due to the high strength of the fiber reinforced concrete. Sensors in transverse direction, 3D-1-T1 and 3D-2-T1, are expected to sense higher strain compared to sensors in vertical and longitudinal directions, because the transverse sensors are affected by other tires ~~in~~ parallel to the loading tires, which carry the same amount of loads as the loading tire. All the sensors recovered after the induced strain of the static loading. The static loads did not induce micro cracks inside the ultra-thin concrete overlay (<100 με), validating the strength of the mix design of the overlay for designed loads. However, the truck loading induced larger than expected tensile strains in the transverse direction; long-term truck traffic may cause fatigue cracks in the transverse direction.

7.3 Dynamic field testing and results

7.3.1 Dynamic field test at 5mph

The dynamic testing was performed using two different driving speeds: 5mph and 37mph. Figs. 7.7(a) and (b) show the detected strain from the vertical sensor component of the 3D-GFRP-FBG sensor, Figs. 7.8(a) and (b) illustrate that from the longitudinal sensor component, and Figs. 7.9(a) and (b) indicate that from the transverse component, during the truck driving forward and backward at 5mph. At relative low speed, all the three sensor components clearly captured all five axles and the shape of the truck both for the forward and backward circumstances. Due to the frequency limitation of the used FBG interrogator (10 Hz) and the fluctuation of the wheel loading location during driving, the measured strain missed some of the largest loading during the truck passing by, especially for the vertical sensor component.

It is commonly expected that for traffic monitoring the vertical component of the 3-D sensor will perform better for load detection in concrete pavement since it is directly laid in the direction of loading.

A lot of efforts were made to make it to true to have vertical sensors inside pavement. This may be true for flexible pavement [6], but in concrete pavement, it may not be true. When comparing Figs. 7.7(a, b) to that of the Figs. 7.8(a, b) and 7.9(a, b), we found out the vertical component is not the most sensitive component but the longitudinal component. Due to the bending effects, both negative and positive strains were observed in the longitudinal measurements, which can be used to determine the size of the passing wheel.

The causes for the phenomenon that vertical sensor component has lower sensitivity majorly account that the vertical component of the 3-D sensor has limited loading contact surface. The passing truck gets one chance to catch the passing vehicle only if the truck is accurately driving on top of the sensor location along the wheel load path. In reality, however, it is hard to control the truck to driving always in the wheel load path, which increases the chances for missing the passing truck. If not directly loaded on the top of the vertical sensor component, the accuracy for weight in motion measurement will be affected. On the other hand, the longitudinal and transverse components will be a better job compared to the vertical component because a large loading surface. The sensitivity of the longitudinal and transverse sensor components was not reduced, and on the contract the weight measurement sensitivity was improved by the bending effects on the sensor under loading.

The lab testing of the fiber reinforced PCC concrete pavement has a stiffness of 14 GPa. Based on field static calibration tests, with the pavement trains measured and the loading surface determined at a speed of 5mph, the weight of each tire and thus each axle of the truck can be estimated from each sensor component of the 3-D sensor.
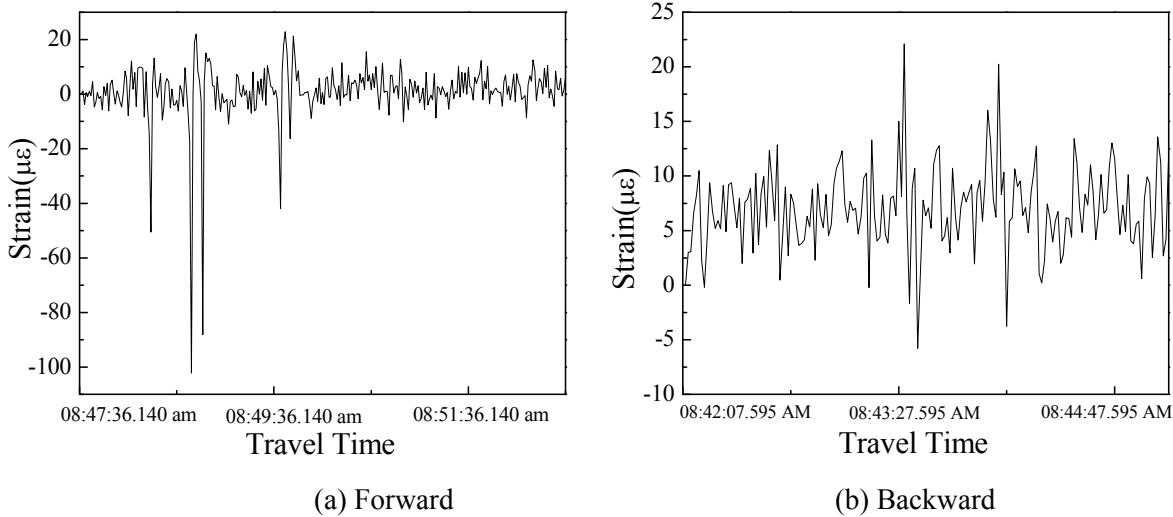
(a) Forward   (b) Backward
Fig. 7.7. Measured strains from vertical component of the 3D-GFRP-FBG sensor at 5mph.

76
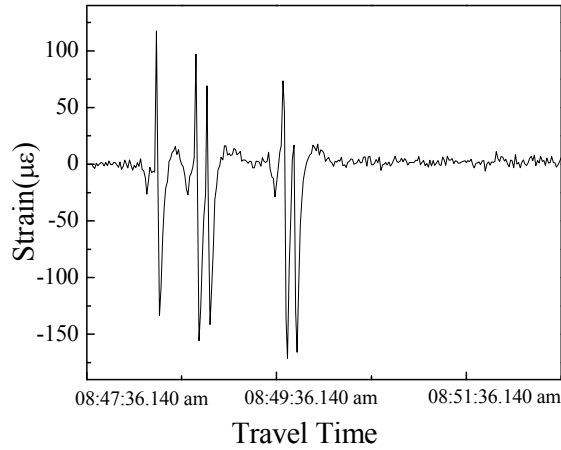
(a) Forward　　　　　　　　　　　　　　(b) Backward

Fig. 7.8. Measured strains from longitudinal component of the 3D-GFRP-FBG sensor at 5mph.
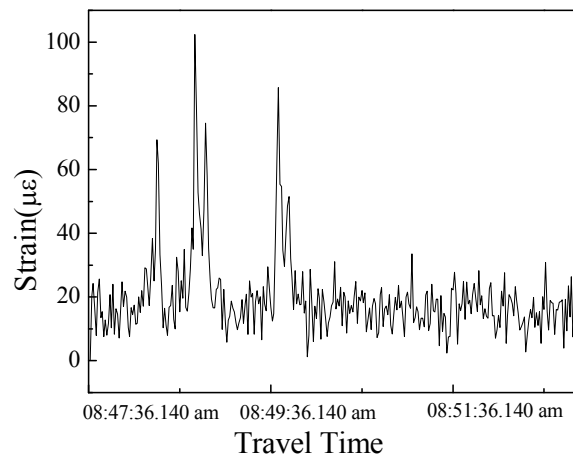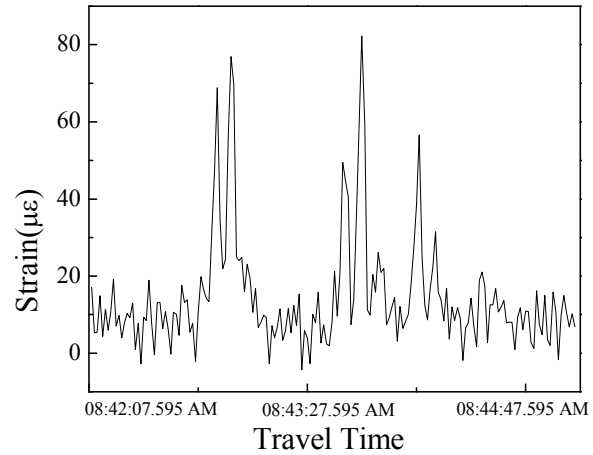
(a) Forward　　　　　　　　　　　　　　(b) Backward

Fig. 7.9. Measured strains from transverse component of the 3D-GFRP-FBG sensor at 5mph.

　　　Table 7.3 shows the calculated weight-in-motion at each axle measured from the three sensor components of the installed 3D-GFRP-FBG sensors. Table 7.3 shows the corresponding calculated relative error of the three sensor components when the truck was driving forward at 5mph. When the truck was driving backward, the vehicle is hard to be controlled driving precisely along the wheel path, which brought in additional errors for the measurements as can be seen from Table 7.4. Table 7.4 clearly shows that the longitudinal sensor component has the best performance in terms of sensitivity, consistency, repeatability, and accuracy. An error of less than 10% of weight measurement was achieved by the longitudinal sensor component with a low truck speed at 5mph. The vertical sensor exhibits excellent accuracy when the wheel was exactly loaded on top of the sensor, however, with point sensing limitation, it showed large variance of loading sensing when the truck was driving a little bit away from the wheel path.

77

Table 7.3 Measured weight-in-motion at 5mph

Sensor component		Axle #1 (kips)	Axle #2 (kips)	Axle #3 (kips)	Axle #4 (kips)	Axle #5 (kips)
Actual Wight		12	17.7	16.8	16.7	16.8
Vertical	Forward	11.80	17.69	15.23	5.81	3.17
	Backward	-	-	-	-	-
Longitudinal	Forward	12.21	17.97	16.32	15.81	15.31
	Backward	8.52	10.34	9.67	11.24	12.35
Transverse	Forward	10.81	17.72	12.90	11.87	7.14
	Backward	8.82	14.24	8.57	10.66	9.53

Table 7.4 Relative error for the 3D-FRP-FBG sensor for weight-in-motion measurement at 5mph

Sensor component (Forward only)	Axle #1	Axle #2	Axle #3	Axle #4	Axle #5
Vertical	1.7%	0.06%	9%	65.2%	81%
Longitudinal	1.7%	1.5%	2.8%	5.3%	8.9%
Transverse	9.9%	0.1%	23.2%	28.9%	57.5%

7.3.2 Dynamic field test at 37mph

Fig. 7.10(a) shows the testing scene of the higher speed weight in motion measurement tests. Fig. 7.10(b) to (d) illustrates the detected strain from the vertical, longitudinal, and transverse sensor components of the 3D-GFRP-FBG sensor during the truck driving at 37mph. With a short clear distance between the second and third axle, and between the fourth and fifth axle, and limited by the low sampling rate of the FBG interrogator, these two set of data almost overlay each other and hard to distinguish. All the three sensor components showed promising detection of the truck appearance, truck size, and truck induced strains in the pavements as can be seen from Figs. 7.10(b-d). Obviously, higher speed reduces the sensitivity of the sensor and increases the chances for missing the maximum loads towards strain and corresponding weight measurements. Four times of speed reduced twice the sensitivity towards strain sensing using the same sensor sets for weight-in-motion measurements.

(a) Testing scene

(b) Vertical sensor component

78
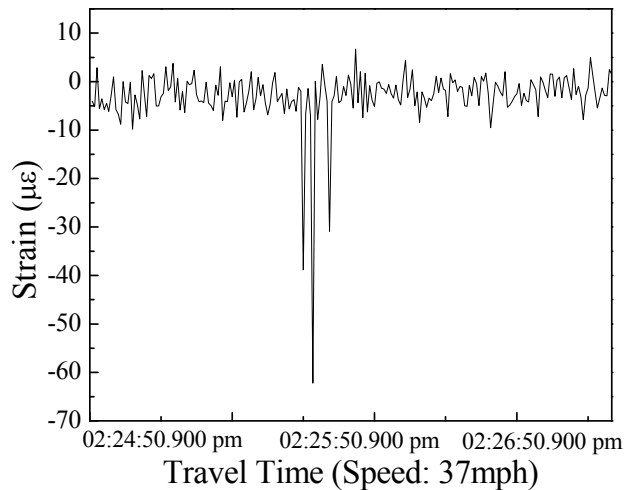
(c) Longitudinal component   (d) Transverse component
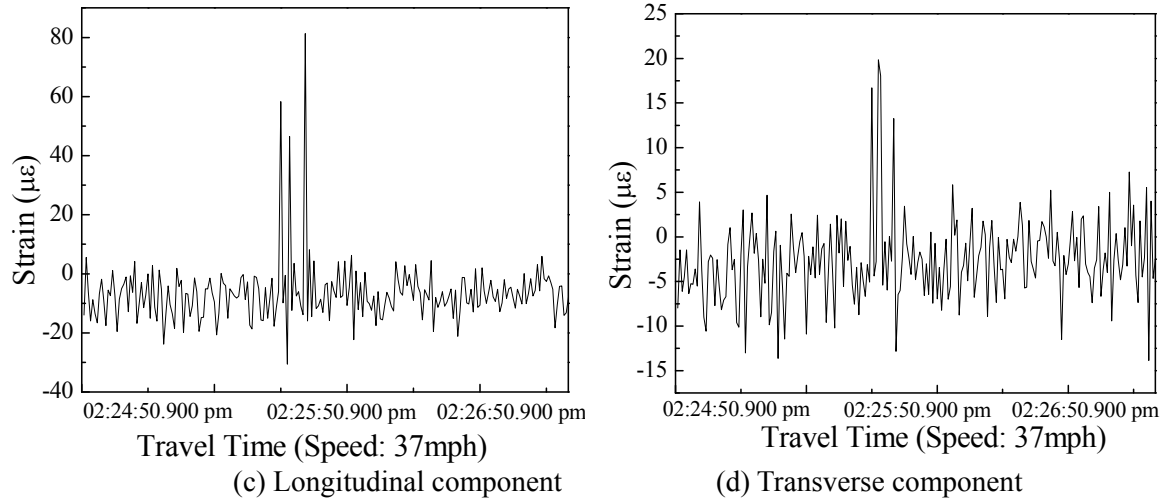
Fig. 7.10. 3D-GFRP-FBG sensor responses for truck driving at 37mph.

Table 7.5 shows the calculated weight-in-motion and corresponding relative errors for all the associated five axles at the speed of 37mph. Consistent with the dynamic testing at 5mph, the longitudinal component of the 3-D GFRP-FBG sensor had the best performance with relative error less than 15% for 37mph speed. To improve the accuracy of the measurement system for higher speed weight-in-motion, FBG integrator with higher sampling rate is required.

Table 7.5 Measured weights in motion at 5mph

Sensor component	Axle 1 (kips)	Error	Axle 2 (kips)	Error	Axle 3 (kips)	Error	Axle 4 (kips)	Error	Axle 5 (kips)	Error
Vertical	13.14	9.5%	17.90	1.1%	17.90	16.2%	11.41	31.7%	11.41	32.1%
Longitudinal	12.10	0.8%	16.07	10.70%	16.07	9.2%	18.76	12.3%	18.76	11.7%
Transverse	11.29	5.9%	15.60	11.9%	14.54	33.2%	8.53	48.9%	8.29	50.7%

7.4 Summary and remarks

In this chapter, a robust infrastructure monitoring system based on GFRP protected FBG was introduced for the performance evaluation of concrete pavements. A number of GFRP-FBG sensors were deployed at MnROAD facility, MnDOT to monitor ultimate thin concrete overlay behavior under simulated low-volume truck loads. The developed sensors showed a 100% survival rate after casting in place, which is superior to most electrical gauges. The deployed GFRP-FBG sensors successfully monitored the closing behavior of the crack and joint in existing pavement during the overlay casting and a slight reopening after two months of overlay in place. With two months of service, the overlay exhibited good performance in transverse direction and a slightly weaker behavior in longitudinal direction for potential tension micro cracks in future. The static load testing results showed sufficient strength of the concrete mix design for this thin overlay and promising results by the authors' experience.

The 3D-GFRP-FBG sensors also were applied to monitor the traffic on the pavements and effectively monitored the weight of the MnROAD truck at the speed of 5mph and 37mph, at MnROAD facility, Minnesota. The dynamic loading testing results indicated that the longitudinal component of the 3-D-GFRP-FBG sensor had the best performance of weight-in-motion measurement at low speed of 5mph for each axle with measured relative error less than 10%. Higher speed testing at 37mph showed that higher speed will reduce the sensitivity of the weight-in-motion of the developed 3D-GFRP-FBG sensor. Due to the limited sampling rate of the FBG integrator of 10Hz, the space between the closest two axle is hard to distinguish. The experimental data will be compared to field strain gauge data and Lab simulation data for further validation of the developed sensing technology for weight-in-motion measurement and vehicle identification. To improve the sensitivity and accuracy of the weight-in-motion measurement

based on the 3D-GFRP-FBG sensors, a higher sampling rate FBG integrator of 1 kHz will be tested and compared with the current testing results in near future.

The GFRP-FBG sensors not only can be used for evaluation of thin concrete overlay but also is capable for application in monitoring of regular concrete pavements. The minimum thickness, which the developed sensors can apply, is determined by the dimension of the sensors, say 2 inches, for an effective monitoring strategy. The thickness of the pavement, if thicker than the dimensions of the sensor, is not expected to influence the sensor accuracy based on our previous studies. Thus, with all the unique advantages of high durability and long-term stability, wide applications of the GFRP-FBG sensors for real-time pavement and traffic monitoring are expected in the near future.

Chapter 8 Concluding remarks

In this study, PPP-BOTDA technique has been successfully implemented in concrete pavement panels to measure strains and detect cracks from the strain distribution with 2 cm spatial resolution by using commercial standard single mode fibers (SMFs). This provides a technical performance database for the use of the cost-effective distributed optical fiber solution for pavement and other infrastructure monitoring.

Based on the characterization and calibration tests, Corning SMF-28e^{+} fibers can sustain up to 12,000 με (1.2%) tensile strain at an average ultimate load of 12.68 N. The axial stiffness was estimated to be 9.63×10^{-5} N/με. With the PPP-BOTDA technique, the Brillouin frequency shift to strain sensitivity coefficient is 5.41×10^{-5} GHz/με. This calibration coefficient can be used to convert the frequent shift measurement to the strain applied on the optical fiber in practical applications.

Even though fragile in shear, optical fibers can be protected with an approximately 0.5-1.0 cm thick mortar layer that is set to harden for about 2 hours prior to concrete pouring. This installation method is applicable to field conditions. The fiber installation method was successfully demonstrated in the laboratory tests. The concrete pavement panels instrumented with three types of distributed optical fibers and FBG sensors were tested and strain distributions were obtained under truck and three-point loads from SMFs based on the PPP-BOTDA measurement. Micro cracks in the concrete panels were identified and localized from the strain distributions in which the sharp peaks represent the locations of cracks.

The appearance of new cracks and the propagation of existing cracks can be captured with high resolution. Two micro cracks with a 10 cm distance were distinguished during the tests. However, further tests are required to understand the ability of discerning two cracks with minimum spacing since it was evident that two strains at points of 2 cm apart can be distinguishable from the PPP-BOTDA measurement. The widening of cracks can be monitored and quantified by relating the crack width with its corresponding peak value in strain distributions.

The strain measurements from a distributed optical fiber sensor and its nearby FBG sensor are in good agreement. The overall difference is approximately 2% mainly due to non-collocation of the two sensors in applications. The measurements from three different types of distributed optical fibers that are close in distance are also in good agreement. The bare SMF-28e^{+} fiber sensor has the highest sensitivity to micro cracking and the highest spatial resolution but the lowest strength to resist brutal actions during construction. The concrete crack cable is most rugged but least sensitive to micro cracking and the lowest in spatial resolution. The performances of the SMF-28e^{+} fiber with tight buffer are in between the bare fiber and the concrete crack cable.

After the truck load tests, the six full-size concrete panels reinforced with micro fibers were tested to failure with a three-point bending setup. By comparing their structural performances, a fabric sheet bonded to the bottom of a panel proved effective as reinforcement. It can significantly improve both strength and ductility of the panel.

By comparing the structural performances of six concrete panels reinforced with fabric sheets and the one without a fabric sheet, the fabric sheets were proven to be effective to serve as reinforcement. Both the strength and the ductility can be appreciably improved by using the fabric sheet.

One- and three-dimensional FBG sensors protected by glass fiber reinforced polymers have been successfully implemented in field conditions at MnDOT roadway test facility since summer 2012. The collected data provides critical information about the concrete pavement condition and, more importantly, field performance experience for the long-term monitoring of pavement and other civil infrastructure in the years to come.

References

[1] **X Bao, L Chen**. Recent Progress in Brillouin Scattering Based Fiber Sensors. Sensors 2011, 11, 4152-4187; doi:10.3390/s110404152.

[2] **X Bao, L Chen**. Recent Progress in Distributed Fiber Optic Sensors. Sensors 2012, 12, pp. 8601-8639; doi:10.3390/s120708601.

[3] **A Deif, , B Martín-Pérez, B Cousin, C Zhang, X Bao, W Li.** Detection of cracks in a reinforced concrete beam using distributed Brillouin fibre sensors. Smart Materials and Structures 19 (2010), pp. 1-7. doi:10.1088/0964-1726/19/5/055014.

[4] **X Zeng, X Bao, CY Chhoa, TW Bremner, AW. Brown, MD DeMerchant, G Ferrier, AL Kalamkarov, and AV Georgiades**. Strain measurement in a concrete beam by use of the Brillouin-scattering-based distributed fiber sensor with single-mode fibers embedded in glass fiber reinforced polymer rods and bonded to steel reinforcing bars. Applied Optics 41 (2002), pp. 5105-5114.

[5] **JM Henault, M Quiertant, S Delepine-Lesoille, J Salin, G Moreau, F Taillade, K Benzarti.** Quantitative strain measurement and crack detection in RC structures using a truly distributed fiber optic sensing system. Construction and Building Materials. Construction and Building Materials 37 (2012), pp. 916-923.

[6] **KT Wan, C Leung.** Applications of a distributed fiber optic crack sensor for concrete structures. Sensors and Actuators A 135 (2007), pp. 458-464.

[7] **R Bernini, A Minardo, L Zeni.** Accurate high-resolution fiber-optic distributed strain measurements for structural health monitoring. Sensors and Actuators A 134 (2007), pp. 389-395.

[8] **A Klar, et al.** Monitoring tunneling induced ground displacements using distributed fiber-optic sensing. Tunneling and Underground Space Technology 40 (2014), pp. 141-150.

[9] **TT Guo, WQ Yuan, LH Wu**. Experimental research on distributed fiber sensor for sliding damage monitoring. Optics and Lasers in Engineering 47 (2009), pp. 156-160.

[10] **Z Zhu, Y Dong, Q Yuan, B Liu, C Jing.** A novel distributed optic fiber transducer for landslides monitoring. Optics and Lasers in Engineering 49 (2011), pp. 1019-1024.

[11] **RM L,opez, VV Spirin, SV Miridonov, MG Shlyagin, G Beltr,an, EA Kuzin.** Fiber optic distributed sensor for hydrocarbon leak localization based on transmission/reflection measurement. Optics and laser technology 34 (2002), pp. 465 - 469.

[12] **SC Huang, WW Lin, MT Tsai, MH Chen.** Fiber optic in-line distributed sensor for detection and localization of the pipeline leaks. Sensors and Actuators A 135 (2007) pp. 570–579.

[13] **A MacLean, C Moran, W Johnstone, B Culshaw, D Marsh, P Parker.** Detection of hydrocarbon fuel spills using a distributed fibre optic sensor. Sensors and Actuators A 109 (2003), pp. 60-67.

[14] **C Zhang, X Bao, IF Ozkan, M Mohareb, F Ravet, M Du.** Prediction of the pipe buckling by using broadening factor with distributed Brillouin fiber sensors. Optical Fiber Technology 14 (2008), pp. 109-113.

[15] **MK Barnoski, MD Rourke, SM Jensen, RT Melville.** Optical time domain reflectometer. Appl. Opt. 1977, 16, pp. 2375-2379.

[16] **C Li, Y Zhang, T Liu, X Li, X Cheng.** Distributed optical fiber bi-directional strain sensor for gas trunk pipelines. Optics and Lasers in Engineering 36 (2001), pp. 41-47.

[17] **G Yilmaz, SE Karlik.** A distributed optical fiber sensor for temperature detection in power cables.

Sensors and Actuators A 125 (2006), pp. 148-155.

[18] **NMP Pinto, O Frazao, JM Baptista, JL Santos.** Quasi-distributed displacement sensor for structural monitoring using a commercial OTDR. Optics and Lasers in Engineering 44 (2006), pp. 771–778.

[19] **AJ Rogers.** Polarisation optical time domain reflectometry. Electron. Lett. 1980, 16, 489–490.

[20] **AH Hartog, DN Payne, AJ Conduit.** Polarization Optical-Time-Domain Reflectometry: Experimental Results and Application to Loss and Birefringence Measurements in Single-Mode Optical Fibres. In Proceeding of the 6th European Conference and Exhibition on Optical Communication (ECOC), York, UK, 16–19 September 1980.

[21] **K Takada, A Himeno, K Yukimatsu.** Phase-noise and shot-noise limited operations of low coherence optical time domain reflectometry. Appl. Phys.Lett.1991, 59, pp. 2483–2485.

[22] **Y Koyamada.** "New technique for distributed strain measurement in optical fibers with very high sensitivity by making use of Rayleigh backscattering", Technical Report of IEICE, OFT98-23, pp. 21–25, 1998 (in Japanese).

[23] **M Wegmuller, F Scholder, N Gisin.** Photon-counting OTDR for local birefringence and fault analysis in the metro environment. J. Lightwave Technol. 2004, 22, pp. 390–400.

[24] **Y Lu, T Zhu, L Chen, and X Bao**. Distributed vibration sensor based on coherent detection of phase-OTDR. J. Lightwave Technol. 28, 2010, pp. 3243-3249.

[25] **JC Juarez, EW Maier, KN Choi, and HF Taylor**. Distributed fiber-optic intrusion sensor system. J. Lightwave Technol. 23(6), 2005, pp. 2081-2087.

[26] **Z Qin, T Zhu, L Chen, and X Bao**. High sensitivity distributed vibration sensor based on polarization maintaining configurations of phase-OTDR. IEEE Photon. Technology Letter. 23(15), 2011, pp. 1091-1093.

[27] **SA Kingsley, DEN Davies**. OFDR diagnostics for fibre and integrated-optic systems. Electron. Lett. 1985, 21, pp. 434-435.

[28] **BJ Soller; DK Gifford; MS Wolfe; ME Froggatt.** High resolution optical frequency domain reflectometry for characterization of components and assemblies. Opt. Express 2005, 13, pp. 666-674.

[29] **T Horiguchi; T Kurashima; M Tateda.** Tensile strain dependence of Brillouin frequency shift in silica optical fibers. IEEE Photonics Technol. Lett. 1989, 1, pp. 107–108.

[30] **GA Brown; AH Hartog.** Optical fiber sensors in upstream oil and gas. J. Petroleum Technol. 2002, 54, pp. 63-65.

[31] **M Belal; YT Cho; M Ibsen; TP Newson.** A temperature-compensated high spatial resolution distributed strain sensor. Meas. Sci. Technol. 2010, 21, 015204.

[32] **D Culverhouse; F Farahi; CN Pannell; DA Jackson.** Potential of stimulated Brillouin scattering as sensing mechanism for distributed temperature sensors. Electron. Lett. 1989, 25, pp. 913-915.

[33] **T Kurashima; T Horiguchi; M Tateda.** Distributed-temperature sensing using stimulated Brillouin scattering in optical silica fibers. Opt. Lett. 1990, 15, pp. 1038-1040.

[34] **K Shimizu; T Horiguchi; Y Koyamada; T Kurashima** Coherenet self-heterodyne detection of spontaneously Brillouin-scattered light waves in a single-mode fiber. Opt. Lett. 1993, 18, 185-187.

[35] **X Bao; DJ Webb; DA Jackson.** 32km distributed temperature sensor based on Brillouin loss in an optical fiber. Opt. Lett. 1993, 18, 1561–1563.

[36] **X Bao; J Dhliwayo; N Heron; DJ Webb; DA Jackson.** Experimental and theoretical studies on a distributed temperature sensor based on Brillouin scattering. J. Lightwave Technol. 1995, 13, 1340–1348.

[14] **X Bao; DJ Webb; DA Jackson.** 22-km distributed temperature sensor using Brillouin gain in an optical fiber. Opt. Lett. 1993, 18, 552–554.

[37] **R Parker; M Farhadiroushan; VA Handerek; AJ Roger.** A fully distributed simultaneous strain and temperature sensor using spontaneous Brillouin backscatter. IEEE Photonics Technol. Lett. 1997, 9, 979–981.

[38] **D Garus; T Golgolla; K Krebber; F Schliep.** Brillouin optical frequency-domain analysis for distributed temperature and strain measurements. J. Lightwave Technol. 1997, 15, 654–662.

[39] **T Golgolla.; Krebber K.** Distributed beat length measurements in single-mode optical fibers using stimulated Brillouin-scattering and frequency-domain analysis. J. Lightwave Technol. 2000, 18, 320–328.

[40] **K Hotate; Hasegawa T.** Measurement of Brillouin gain spectrum distribution along an optical fiber with a high spatial resolution using a correlation-based technique—Proposal, experiment and simulation. IEICE Trans. Electron. 2000, E83-C, pp. 405-411.

[41] **R Bernini; A Minardo; L Zeni.** Distributed Sensing at centimeter-scale spatial resolution by BOFDA: Measurements and signal processing. IEEE Photonics J. 2012, 4, 48–56.

[42] **K Hotate; M Tanaka.** Distributed fiber Brillouin strain sensing with 1cm spatial resolution by correlation-based continuous-wave Technique. IEEE Photonics Technol. Lett. 2002, 14, pp. 179-181.

[43] **K Hotate.** Brillouin scattering accompanied by acoustic grating in an optical fiber and applications in fiber distributed sensing. Proc. SPIE 2011, 7753, pp. 7-10.

[44] **W Li; X Bao; Y Li; L Chen.** Differential pulse-width pair BOTDA for high spatial resolution sensing. Opt. Express 2008, 16, 21616–21625.

[45] **L Hao; W Li; N Linze; L Chen; X Bao.** High resolution DPP-BOTDA over 50 km fiber using return to zero coded pulses. Opt. Lett. 2010, 35, 1503–1505.

[46] **Y Dong; H Zhang; L Chen; X Bao.** A 2-cm-spatial-resolution and 2-km-range Brillouin optical fiber sensor using a transient differential pulse pair. Appl. Opt. 2012, 51, 1229–1235.

[47] **K Kishida; CH Li.** Pulse pre-pump-BOTDA technology for new generation of distributed strain measuring system. Structural Health Monitoring and Intelligent Infrastructure 2006, pp. 471-477.

[48] **MN Alahbabi; YT Cho; TP Newson.** Simultaneous temperature and strain measurement with combined spontaneous Raman and Brillouin scattering. Opt. Lett. 2005, 30, 1276-1278.

[49] **G Bolognini; MA Soto; FD Pasquale.** Fiber-optic distributed sensor based on hybrid Raman and Brillouin scattering employing multiwavelength Fabry-Pérot lasers. IEEE Photon. Technol. Lett. 2009, 21, 1523-1525.

[50] **G Bolognini; MA Soto.** Optical pulse coding in hybrid distributed sensing based on Raman and Brillouin scattering employing Fabry-Pérot lasers. Opt. Express 2010, 18, 8459-8465.

[51] **W Zou; Z He; K Hotate.** Complete discrimination of strain and temperature using Brillouin frequency shift and birefringence in a polarization-maintaining fiber. Opt. Express 2009, 17, 1248-1255.

[52] **W Zou; Z He; K Hotate.** Demonstration of Brillouin distributed discrimination of strain and temperature using a polarization-maintaining optical fiber. IEEE Photon. Technol. Lett. 2010, 22, 526-528.

[53] **Y Dong; L Chen; X Bao.** High-spatial-resolution time-domain simultaneous strain and temperature sensor using Brillouin scattering and birefringence in a polarization-maintaining fiber. IEEE Photon. Technol. Lett. 2010, 22, 1364–1366.

[54] **ME Froggatt; DK Gifford; ST Kreger; MS Wolfe; BJ Soller.** Distributed Strain and Temperature Discrimination in Unaltered Polarization Maintaining Fiber. In Optical Fiber Sensors, OSA Technical Digest (CD); Optical Society of America: Cancún, Mexico, 23 October 2006; paper ThC5.

[55] **D Zhou, W Li, L Chen and X Bao.** Distributed Temperature and Strain Discrimination with Stimulated Brillouin Scattering and Rayleigh Backscatter in an Optical Fiber. Sensors 2013, 13, 1836-1845; doi:10.3390/s130201836

[56] **K Kishida; CH Li; K Nishiguchi; Y Yamauchi; A Guzik; T Tsuda.** Hybrid Brillouin-Rayleigh distributed sensing system. Proc. SPIE 2012, 8421, 84212G.

[57] **K Kishida, K Nishiguchi, CH Li and A Guzik.** An important milestone of distributed fiber optical sensing technology: separate temperature and strain in single SM fiber. Proc. OECC 2009 (14), 1-2.